Oberflächenplasmonen-artige Resonanzen auf metallischen Gittern

Dissertation zur Erlangung des Grades
„Doktor der Naturwissenschaften“

am Fachbereich Physik
der Johannes Gutenberg-Universität
in Mainz

vorgelegt von
Maximilian Kreiter
geboren in Neuburg an der Donau

Mainz, 2000

Tag der mündlichen Prüfung: 28. Juni 2000

Surface plasmon-related resonances on metallic diffraction gratings

submitted to
Fachbereich Physik
Johannes Gutenberg-Universität
Mainz

as a thesis for the degree of
„Doktor der Naturwissenschaften“

by
Maximilian Kreiter

Mainz, 2000

Contents

1 Introduction

Almost 100 years ago, R. W. Wood observed strong, angular dependent variations in the intensity of light that was reflected from an optical metal grating [Woo02]. These effects are due to the interaction of light with a fundamental excitation of a metal-dielectric interface. This excitation is characterised by a charge density oscillation in the metal, which is accompanied by an electromagnetic field that extends in both media. Since the energy is confined to the vicinity of the metal surface, and the conduction electrons of a metal can be treated as a plasma, this excitation is called the surface plasmon resonance. For quite a long period of time, not much progress was made in this field until the availability of new theoretical and experimental techniques triggered growing interest in the optics of metal gratings.

Today, many aspects of the optics of metal gratings are well understood, although a quantitative mathematical description of the processes that are involved in the interaction of light with metal gratings cannot be obtained analytically. The availability of computers allowed the development of algorithms that solve this mathematical problem numerically, and enabled focusing the attention of contemporary research on the optics of metal gratings. A short introduction to the basic understanding of „Wood's anomalies" and grating optics as established today is given in the second chapter. The possibilities offered by numerical modelling are described.

Since lasers have become relatively cheap and easy to handle, optical experiments with a previously unknown precision have become possible. The development of techniques for the structuring of surfaces on a sub-micron scale, which were pushed forward by the silicon technology, allows the preparation of high-quality samples. Details about the experimental techniques that were explored in this work are described in chapter 3.

A large variety of interesting effects in the context of Wood's anomalies has now been studied both theoretically and experimentally. Many of them are due to the ability of the surface plasmon resonance to interact not only with light like in Wood's original experiment, but with other forms of energy as well. The strong influence of the geometry defined by the grating still allows the observation of new and sometimes puzzling effects due to surface plasmons on gratings. The understanding of these effects is desirable not only from a fundamental point of view, but also because mechanisms that allow a defined control over the optical properties of a surface promise applications in the future. This work is intended as a contribution to gain more insight into the world of surface plasmons and the ways they exchange energy with other excitations.

The occurrence of Wood's anomalies is due to an energy transfer from light to the surface plasmon resonance and from there to thermal energy of the metal. In the fourth chapter, an experiment is presented to prove the possibility of the reverse process:

surface plasmons may be thermally excited and lead to specific light-emission properties of a metallic grating.

Another possible channel of energy exchange is the interaction of two surface plasmons which is possible on metal gratings. As a consequence, coupled resonances that are quite different from ordinary surface plasmons may exist already on weakly corrugated metal surfaces. These resonances are well studied both in theory and experiment [Bar96]. Theoretical studies of the effect of an increased depth of the modulation and a strong asymmetry on the coupled resonances have been reported [Wan98], [Sob98], [Lop98]. They predict a strong change of the coupled resonances as well as new types of resonances that are supported on sufficiently deep structures. In chapter 5, these effects are investigated further by model calculations. A new theoretical viewpoint is adapted to combine the results from literature with some new findings into a consistent picture. These theoretical predictions serve as a basis for the interpretation of the experimental results that are in the main focus of this chapter (5).

Both surface plasmons and coupled resonances may exchange energy with electronic excitations of molecules that are placed in the vicinity of the surface. In the sixth chapter, the influence of the localisation of the electrical field of coupled resonances on the excitation and emission properties of a fluorescent dye is investigated.

The coupling strength of light to the surface plasmon resonance is strongly dependent on the polarisation state of the light. In chapter 7, attempts are described to obtain a better understanding of the polarisation dependence for an arbitrary reflection geometry.

Finally, a small contribution is made to the most prominent field of application of the surface plasmon resonance. Surface plasmon spectroscopy is a method to investigate ultra-thin dielectric films on metal surfaces. Due to the difficulties in data analysis, gratings play a negligible role in this field compared to the alternative approach of prism coupling. In chapter 8, it is shown that gratings are equally well suited for this purpose and an easy evaluation routine is proposed.

2 Introduction to grating- and surface plasmon optics

In this chapter, some fundamental concepts that build the basis for the following discussions are outlined. The notation for the description of light waves is introduced in 2.1, followed by a short discussion of the dielectric function of metals in 2.2. The electromagnetic boundary problem of the reflection of light from a grating is described in 2.3. The surface plasmon resonance is then introduced in the intuitive framework of momentum matching in 2.4 and a comparison is made with the alternative approach of rigorous mathematical modelling.

2.1 Light in matter

For the following, it is necessary to introduce a notation that will be used for the description of light waves. For a detailed treatment of electromagnetism, please refer to one out of a huge number of standard textbooks like the book of Jackson [Jac83]. Electromagnetic radiation in an isotropic, homogenous medium is described by Maxwell's equations without source terms.

$$\begin{aligned} \nabla \cdot \mathbf{E} = 0 \qquad & \nabla \times \mathbf{E} + \frac{\partial \mathbf{B}}{\partial t} = 0 \\ \nabla \cdot \mathbf{B} = 0 \qquad & \nabla \times \mathbf{H} - \frac{\partial \mathbf{D}}{\partial t} = 0 \end{aligned} \tag{2.1}$$

Where **E** is the electrical field, **H** the magnetic field, **D** the electrical displacement and **B** the magnetic induction. For this work, the media under investigation were assumed to be linear. In this case, the full solution of the electromagnetic problem can be decomposed into independent solutions with a periodicity in time which is given by the angular frequency ω. If such a frequency is fixed by the exciting light, the connection between **D** and **E** is given by the dielectric function ε.

$$\mathbf{D} = \varepsilon(\omega) \cdot \varepsilon_0 \cdot \mathbf{E} \tag{2.2}$$

ε_0 is the permittivity of vacuum. Similarly, **B** and **H** are connected by

$$\mathbf{B} = \mu(\omega) \cdot \mu_0 \cdot \mathbf{H} \tag{2.3}$$

Where μ is the magnetic permeability and μ_0 the permeability of free space. Inside a homogenous and isotropic medium, the solution of Maxwell's equations as a function of time t at the point **x** can be decomposed into plane light waves which are characterised by their electrical field amplitude $\mathbf{E_0}$, the wavevector **k** and their angular frequency ω.

$$\mathbf{E}(\mathbf{x}, t) = \mathrm{Re}\left(\mathbf{E_0} \cdot e^{i(\mathbf{k}\cdot\mathbf{x} - \omega t)}\right) \tag{2.4}$$

The orientation of $\mathbf{E_0}$ is orthogonal to $\mathbf{k}$. For each pair (ω, $\mathbf{k}$), two mutually orthogonal electrical field amplitudes may exist, corresponding to two possible polarisations.

Instead of the electrical field, the magnetic field amplitude $\mathbf{H_0}$ may be used to describe a plane wave.

$$\mathbf{H}(\mathbf{x},t) = \mathrm{Re}\left(\mathbf{H_0} \cdot e^{i(\mathbf{k}\cdot\mathbf{x}-\omega t)}\right) \qquad (2.5)$$

Both representations contain the full information and one representation may be calculated from the other one with the aid of

$$\begin{aligned} \mathbf{H}_0 &= \frac{1}{\mu\ \mu_0\omega} \cdot \mathbf{k} \times \mathbf{E_0} \\ \mathbf{E}_0 &= \frac{1}{\varepsilon\ \varepsilon_0\omega} \cdot \mathbf{k} \times \mathbf{H_0} \end{aligned} \qquad (2.6)$$

Which can be readily seen from (2.1). For a given angular frequency ω, the modulus of $\mathbf{k}$ is fixed by the dispersion relation

$$\frac{\omega^2}{|\mathbf{k}|^2} = \frac{1}{\mu\mu_0\varepsilon\varepsilon_0} = \frac{c^2}{n^2} \qquad (2.7)$$

With the speed of light in vacuo c and the refractive index n which is defined as the ratio of c and the speed of light in matter. In the following, the magnetic permeability μ is assumed as 1 which allows to express the modulus of $\mathbf{k}$ as a function of the dielectric constant only.

$$|\mathbf{k}| = \omega \cdot \sqrt{\varepsilon\varepsilon_0\mu_0} = k_0 \cdot \sqrt{\varepsilon} = k_0 \cdot n \qquad (2.8)$$

Where k_0, the wavevector of the light wave of the corresponding frequency in vacuo has been introduced. It is often convenient to use the wavelength of the light λ instead of $|\mathbf{k}|$, which is defined as

$$\lambda = \frac{2 \cdot \pi}{|\mathbf{k}|} \qquad (2.9)$$

2.2 The dielectric function of metals

It has been shown in the last section that for homogenous and isotropic media, the dielectric function $\varepsilon(\omega)$ is needed to describe the response of the material to the external electromagnetic field that is produced by the incident light. In this work, the focus lies on two classes of materials that have qualitatively different ε, metals and dielectrics.

In dielectrics, the electrons are bound tightly to the nuclei which leads to a small positive and real ε.

Metals are substances that possess quasi-free electrons which are easily moved by an external electrical field. The classical Drude model already allows a good insight into the response of metals without being forced to deal with the quantum theory of solids. A good description of the Drude model can be found in many textbooks of solid state physics, e. g. [Ash76]. The conduction electrons in the metal are assumed to be freely movable so that they can be accelerated by an externally applied electrical field according to Newton's laws. Within a typical time τ, the collision time, they undergo a scattering process after which their propagation direction is completely random and their average velocity depends on the thermal energy of the metal. In this framework, the dielectric constant of a metal as a function of the frequency ω of the applied electrical field can be derived as

$$\varepsilon(\omega) = 1 - \frac{\omega_p^2}{\omega^2 + i\frac{\omega}{\tau}} \qquad (2.10)$$

with the plasma frequency ω_p which is given as

$$\omega_p^2 = \frac{n_e e^2}{\varepsilon_0 m_e} \qquad (2.11)$$

Here, n_e is the electron density, e the charge of an electron and m_e its (effective) mass. Usually, ω_p and τ are used to describe the optical response of a metal. These parameters are determined by comparison to experimental values.

It is seen that the dielectric function of metals is in general complex with a negative real part ε' and a small positive imaginary part ε''.

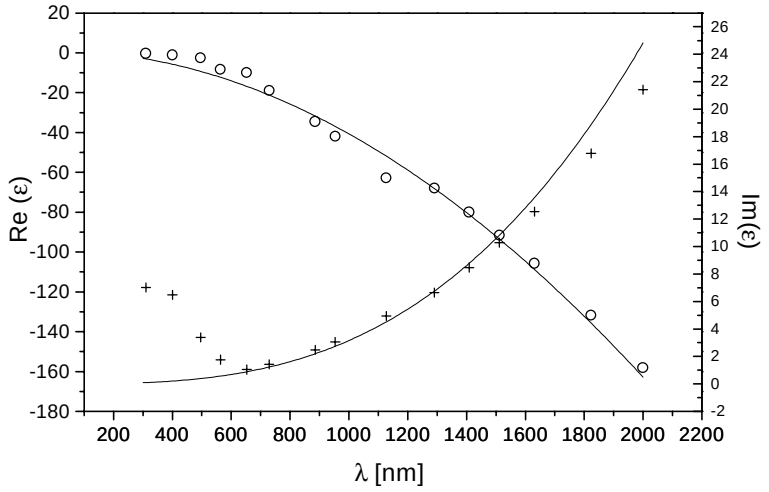

Fig. 2.1: Experimental literature values [Lyn85] for the wavelength-dependent dielectric constant of gold (circles: real part, crosses: imaginary part) in comparison to a Drude-like behaviour ($\tau = 7 \times 10^{-15}$s, $\omega_p = 1.22 \times 10^{16}$s^{-1}) which is plotted as a straight line.

In Fig. 2.1 the experimentally measured dielectric function of gold in the visible and near infrared as obtained from literature [Lyn85] is compared to a Drude-like behaviour with $\tau = 7 \times 10^{-15}$ s, $\omega_p = 1.22 \times 10^{16}$ s^{-1}. These parameters are chosen for the description of the gold gratings that are investigated in this work. At wavelengths of $\lambda > 650$ nm, the Drude model gives a good description of the measured data, at shorter wavelengths there is a significant discrepancy. For radiation in the infrared, the large negative values of the real part of ε indicate that gold acts as a very good reflector, as it is expected from a metal. In the short-wavelength regime of the visible light, gold is a much worse reflector, instead, there is considerable absorption. This is the reason why gold appears yellow.

Around $\lambda = 1200$ nm there appears a slight discontinuity in ε which is due to the fact that the data were gathered from different experiments. This effect is unphysical and due to the sometimes rather strong variations in the optical quality of evaporated films as it has been pointed out by several authors ([Lyn85] and references therein, [Bry91]). Such an evaporated film is usually composed of microscopic crystallites which are responsible for some roughness of the surface. Additionally, there may be voids between the grains. Chemical modification of the surface, as it inevitably takes place as soon as the samples are exposed to air, will have an additional effect on the optical response of the metal. Therefore, it is inappropriate to state one ε for gold surfaces that are fabricated by thermal evaporation for a certain wavelength. Instead, the small variations in the optical response of different samples must be taken into account for a good description of the optical response of metallic surfaces.

2.3 Reflection of light on a grating

In this section, some remarks are made about the electromagnetic problem of a plane wave scattered by a grating. Basic concepts of reflection on planar systems are reviewed in (2.3.1) and the reflection on a grating is introduced in (2.3.2). Finally, a brief introduction in the numerical modelling code that was used for this work is given (2.3.3).

2.3.1 Reflection on a plane multilayer system

The reflection of a plane light wave on a planar multilayer system is sketched schematically in Fig. 2.2. A plane light wave with a fixed wavevector $\mathbf{k_i}$ and frequency ω is incident on a system that consists of layers of homogenous refractive index, separated by plane and parallel interfaces. On each interface the incident beam is subject to reflection and transmission, producing new beams which may again be reflected and transmitted on other interfaces. Each beam is either described by its wavevector or by the planes of equal phase. Both are depicted in Fig. 2.2. It is important to note that for each of these processes the component of the wavevector parallel to the interface, $k_{||}$, of the reflected and transmitted beam is equal to the $k_{||}$ of the incident beam. For this

reason, the electromagnetic field can be decomposed into two components in each layer, an upward and a downward propagating plane wave which are completely described either by their magnetic or by their electrical field.

As it has been pointed out earlier, two orthogonal polarisations are needed for the full description of a plane light wave with a given (ω, **k**). There is one natural choice of two polarisations which are not changed with respect to their polarisation state upon reflection and transmission. They are characterised by having one field component which is orthogonal to the plane of incidence which is spanned by the wavevector $\mathbf{k_i}$ of the incident beam and the surface normal: If the incident beam has an (**E**- or **H**-) field component which is confined to this direction, the same holds for all transmitted and reflected beams. Therefore, the choice of the electrical field in the case of transverse electric polarisation (TE) as basis of the description of the entire problem and of the magnetic field in the case of transverse magnetic polarisation (TM) is particularly easy.

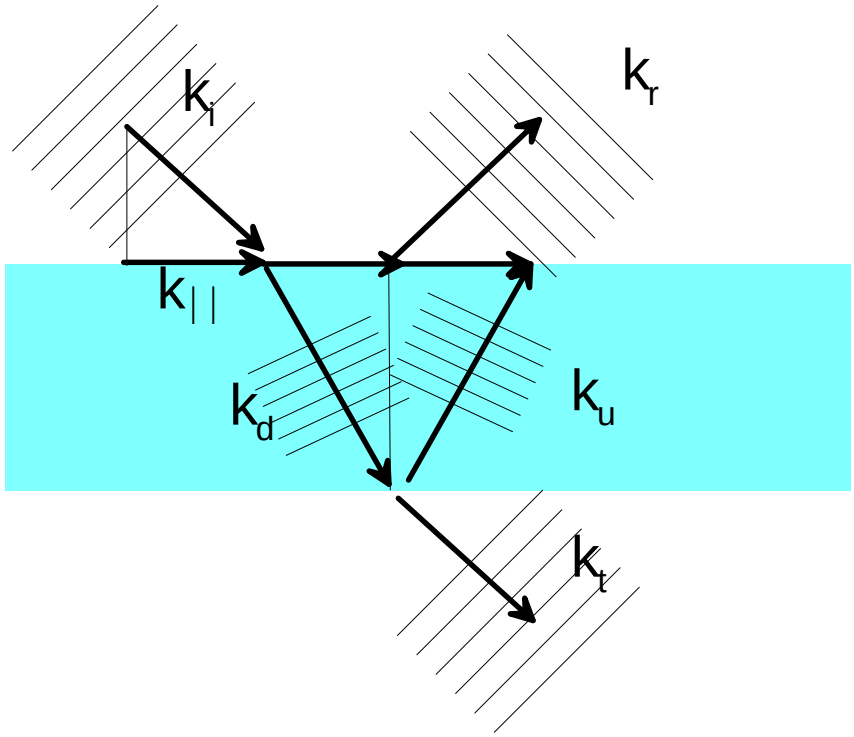

Fig. 2.2 Schematic representation of reflection on a planar 3-layer system. Each plane wave is represented by its wavevector **k**. The subscripts stand for 'incident' (i), 'reflected' (r), 'downward' (d), 'upward' (u), 'transmitted' (t). The in plane component $k_{||}$ is equal for all these contributions. The thin lines depict the planes of constant phase.

For example, consider the TE case. In each layer, only the complex amplitudes of the downward propagating wave and the upward propagating wave, E_d and E_u must be determined to obtain the electromagnetic field distribution in the entire system as well as the reflected and transmitted intensities. In the case of TM polarisation, an equivalent argument holds for the magnetic field. The transfer matrix algorithm (See e.g. [Kar91]) allows the determination of E_u and E_d for the case TE and of H_u and H_d for TM

polarisation in each layer. An arbitrary polarisation is described as linear superposition of the two fundamental polarisations. The local field distributions and the intensities and polarisation states of the reflected and transmitted intensities are calculated by linear superposition of the individual response of the system to TM and TE light.

2.3.2 Reflection on a grating

2.3.2.1 Definition of the geometry

In this work, only relief gratings in one dimension are considered as schematically depicted in Fig. 2.3.

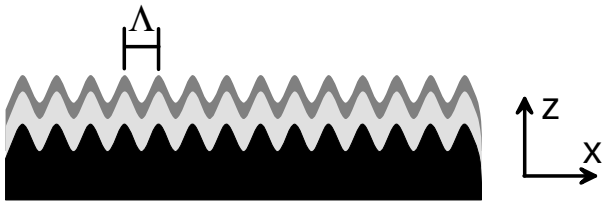

Fig. 2.3: Schematic representation of a multilayered grating.

Again, we deal with layers with a homogenous refractive index and thickness, but all interfaces are now periodically modulated in an identical way. These interfaces are described as the functional dependence z(x).

$$z(x) = z(x+\Lambda) = \sum_{i=0}^{\infty} A_i \cdot \sin\left(\frac{360°}{\Lambda} \cdot i \cdot x + \varphi_i\right) \qquad (2.12)$$

Where Λ is the grating pitch or period of the grating. Due to the periodicity this function may be decomposed into a Fourier representation with amplitudes A_i and phases φ_i.

The parameters that are required to describe the reflection geometry of a plane electromagnetic wave on such a structure are schematically sketched in Fig. 2.4.

The polarisation of the incident light is described as a superposition of TM and TE polarised light with components of the electrical field parallel to the two orthogonal unit vectors $\mathbf{p_{TM}}$ and $\mathbf{p_{TE}}$. If linearly polarised light is considered, the polarisation may be described by a real angle φ where

$$\mathbf{E_0} = E_0^{TE} \cdot \mathbf{p_{TE}} + E_0^{TM} \cdot \mathbf{p_{TM}} = E_0\left(\sin(\varphi)\mathbf{p_{TE}} + \cos(\varphi)\mathbf{p_{TM}}\right) \qquad (2.13)$$

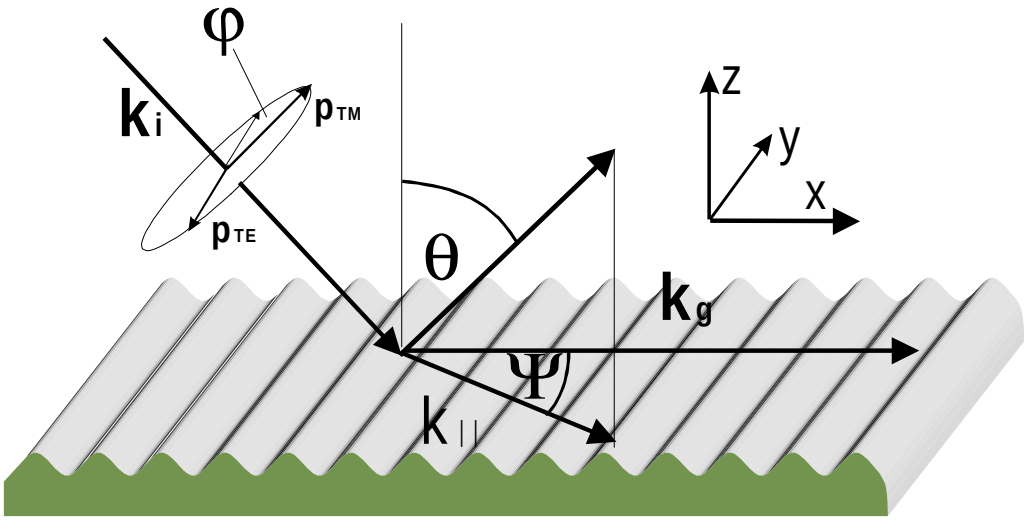

Fig. 2.4: Definition of the parameters that are used to describe reflection of a plane electromagnetic wave on a relief grating.

The co-ordinate system is by definition fixed relative to the symmetry axes of the grating. The z-axis is chosen along the surface normal, y parallel and x perpendicular to the grating grooves. The wavevector $\mathbf{k_i}$ of the incident beam is in the most general case described by the wavelength λ of the incident light, the polar angle θ which denotes the tilt of $\mathbf{k_i}$ relative to the surface normal, and the azimuthal angle Ψ which defines the counterclockwise rotation of the plane of incidence relative to the x-axis, seen along the incident beam (in the sketch, $\Psi \approx -20°$). The wavevector of the incident beam may be written in terms of θ and Ψ.

$$\mathbf{k_i} = k_0 \cdot \sqrt{\varepsilon} \cdot \begin{pmatrix} \sin(\theta)\cdot\cos(\Psi) \\ \sin(\theta)\cdot\sin(\Psi) \\ -\cos(\theta) \end{pmatrix} \qquad (2.14)$$

The vectorial representation of the fundamental polarisations will be treated to some more detail in chapter 7. The reciprocal grating vector $\mathbf{k_g}$ is defined as

$$\mathbf{k_g} = \begin{pmatrix} k_g \\ 0 \\ 0 \end{pmatrix} = \begin{pmatrix} 2\pi/\Lambda \\ 0 \\ 0 \end{pmatrix} \qquad (2.15)$$

2.3.2.2 About the electromagnetic problem

An introduction to the electromagnetic theory of gratings is given in the book edited by Petit [Pet80]. The Floquet-Bloch theorem is of fundamental importance for the optics of gratings. It states that for a periodically modulated interface, the electrical field outside the modulated area due to the reflected beam can be described as

$$\mathbf{E}(\mathbf{x},\mathbf{t}) = \sum_{m=-\infty}^{\infty} E_{TM}^{m} \cdot \mathbf{p_{TM}} \cdot e^{i(\mathbf{k}_m\mathbf{x}-\omega t)} + E_{TE}^{m} \cdot \mathbf{p_{TE}} \cdot e^{i(\mathbf{k}_m\mathbf{x}-\omega t)} \qquad (2.16)$$

With complex amplitudes of the electrical field in the two fundamental polarisations. Additional contributions, the higher diffracted orders are introduced which are characterised by the integer m, the order of the diffracted wave. The wavevector of the m'th diffracted order, $\mathbf{k_m}$ is defined as

$$\mathbf{k}_{\mathbf{m}} = \begin{pmatrix} k_x^i + m \cdot k_g \\ k_y^i \\ \pm\sqrt{(n \cdot k_0)^2 - (k_y^i)^2 - (k_x^i + m \cdot k_g)^2} \end{pmatrix} \qquad (2.17)$$

where the superscript i denotes the Cartesian components of the incident beam and k_g is the modulus of the reciprocal grating vector. The expression describing the z-component is readily derived from the x and y component with the aid of the dispersion of light (2.8). It is important to note that this decomposition into plane waves is valid only for those z which belong to planes normal to z that lie completely in one medium ('region outside the grating grooves'). The validity of this expansion inside the grooves, the Rayleigh assumption, is an approximation which may only be used for shallow gratings (See [Pet80], [Kaz96]).

The additional contributions to the electromagnetic field that are introduced by the presence of a surface relief grating are depicted schematically in Fig. 2.5.

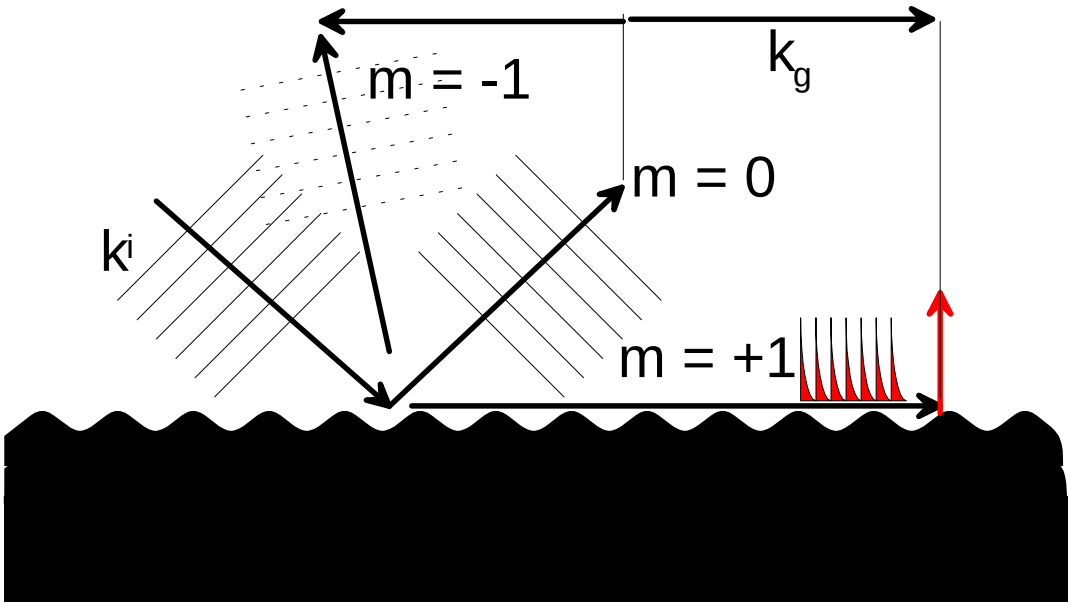

Fig. 2.5: Schematic sketch of the diffracted orders that are introduced by a relief diffraction grating.

In addition to the specular beam (m = 0) that would be there even without a modulation of the interface, new waves are introduced to the system which have an in-plane wavevector which is modified by a multiple integer of the reciprocal grating vector. They may be plane waves with a wavevector that has got only real components if the z-component in equation (2.17) is the square root of a positive number. This is the case for the -1st diffracted order in the example given above. The plane waves are drawn in

the sketch as dashed lines. For the $+1^{st}$ diffracted order, the situation is different. Here, the large $k_{||}$ leads to a negative denominator in the root in (2.17), as a consequence, k_z is purely imaginary. In this case the exponential function in (2.16) consists of a periodically oscillating part in x and y direction and an exponential part along z. These waves are bound to the surface, their intensity decays with a decay length which is given by $|k_z|^{-1}$. This property is expressed in the sketch by lines that become thinner with increasing distance from the sample. Because the intensity of these waves vanishes with increasing distance from the surface they are called evanescent (from lat. evanescere, vanish, die away) waves.

In general, the solution of the electromagnetic problem of a plane wave falling on a relief grating cannot be decomposed into linearly independent orthogonal waves that are excited either by TM or by TE polarisation like on a plane interface. Only for $\Psi = 0°$ these solutions remain independent. This geometry is called the classical mount, other geometries are referred to as conical incidence.

2.3.2.3 The solution of the electromagnetic problem

For the calculation of the response of a grating to illumination with a plane wave, it is necessary to find the amplitudes of all the diffracted orders by application of the boundary conditions to the electrical and magnetic field on the (curved) interface. Only numerical approaches to this problem are known. There are several mathematical concepts to solve this problem which are reviewed in the book of Petit [Pet80] and by Maystre [May82]. An overview over some more recent developments can be found in the paper of Barnes et al. [Bar96]. Even today, new mathematical approaches are being developed [Pla99].

In this work a computer code was used which is based on the work of Chandezon et al. [Cha82] and was progressively refined by various scientists. In the original version this code allows the calculation of the optical response of a multilayer system where the individual isotropic layers are separated by interfaces of equal shape in the classical mount.

Elston et al. [Els91] extended the approach of Chandezon to conical incidence.

Cotter et al. [Cot95] changed the method of transfer matrices to the ‘scattering matrix approach’, a concept which was developed by Li [Li94b] which enhances the numerical stability and therefore applicability of the algorithm.

Preist et al. [Pre97] made the calculation of highly blazed and even overhanging gratings possible by introducing a transformation to a non-orthogonal co-ordinate system which is parametrised by the ‘obliquity angle’ θ_{ob}. The Cartesian co-ordinates x, z of a point which has the oblique co-ordinates x_{ob} and z_{ob} is given by

$$\begin{aligned} z &= z_{ob} \cdot \sin\left(\theta_{ob}\right) \\ x &= x_{ob} + z_{ob} \cdot \cos\left(\theta_{ob}\right) \end{aligned} \qquad (2.18)$$

An illustrative example is given below (Fig. 2.6), the form of a pure sine function in an oblique co-ordinate system with $\theta_{ob} = 55°$ is plotted in real space. It is obvious that this line cannot be represented as a function in the Cartesian co-ordinate system because there y(x) is not unique.

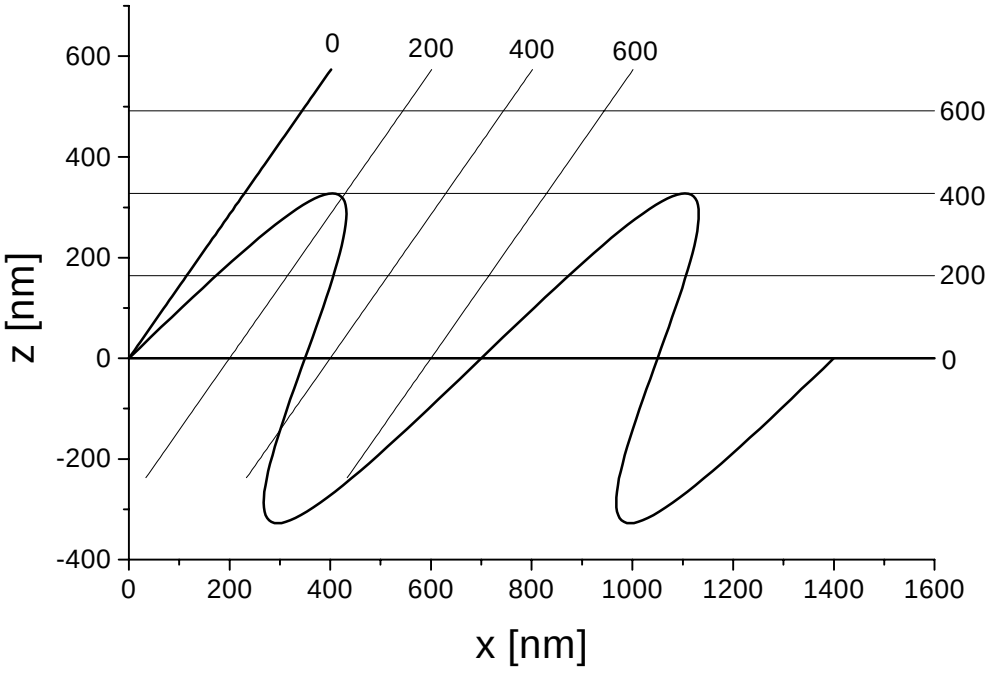

Fig. 2.6: The Cartesian representation of a sine function with a period of $\Lambda = 700$ nm and an amplitude of $A_1 = 400$ nm in a non-orthogonal co-ordinate system with $\theta_{ob} = 55°$. The grid indicates lines of constant z_{ob} and x_{ob} in the oblique system.

Other extensions of this modelling routine which are not used in this work are reported as the inclusion of anisotropic materials [Har96], an infinite periodicity in z-direction [Tan98] as well as the investigation of a multilayer system with different grating shapes [Pre95]. The extension to structures that are modulated in two dimensions has been demonstrated, too [Har96b].

2.3.3 The modelling code ‘oblique’

It is far beyond the scope of this introduction to explain the algorithms that are used for the modelling of the optical response of such a grating structure. As an alternative to the citations given above, a detailed description of the underlying mathematics is given by the author of the numerical modelling code [Wan99].

For the application of the numerical code it is necessary to specify which parameters are used to describe the electromagnetic boundary problem for the numerical evaluation. In addition, the results that are calculated by the code must be specified. This information is put together in Table 2.1.

Table 2.1: Input- and output- parameters of the numerical modelling code 'oblique'

Input Parameters	**Output Parameters**
Grating Profile	**Far field**
→ Pitch Λ	→ Intensities of all the outgoing beams, I_m
→ Amplitudes A_i, Phases φ_i	→ Phases of all the outgoing beams, φ_m
→ Obliquity angle θ_{ob}	**Near field**
Reflection geometry	→ Magnetic field distribution $H_x(x,y,z)$, $H_y(x,y,z)$, $H_z(x,y,z)$
→ Polar angle θ	
→ Azimuthal angle Ψ	→ Electrical field distribution $E_x(x,y,z)$, $E_y(x,y,z)$, $E_z(x,y,z)$
→ Polarisation (TM/TE)	
→ Wavelength λ	
Layer system	
→ Thickness of all layers except 1st and last	
→ Dielectric function, fixed (ε', ε'') or Drude (ω_p, τ)	

The grating profile is described by the pitch Λ, the obliquitiy angle θ_{ob} and the amplitudes A_i and phases φ_i of the Fourier representation. Only a few Fourier components are usually needed to get a reasonable agreement of the model calculation with nature.

The incident beam is specified by its wavelength λ, the propagation direction which is given by θ and Ψ and its polarisation which may be either TM or TE. Since the polarisations are defined relative to the plane of incidence, they have a non-trivial form in the co-ordinate system which is fixed relative to the grating. Arbitrary polarisations are deduced from those as linear superposition as discussed in Chapter 7.

The dielectric properties of each layer are expressed by its dielectric constant ε. It can be chosen either as fixed or a wavelength-dependence according to the Drude model may be assumed (compare section 2.2). In the latter case, the collision time τ and the plasma frequency ω_p must be specified. The thickness must be given for each layer except the first and the last one which are assumed to extend to infinity.

The physical quantities calculated by the program are the intensities (square of the complex amplitudes) of the two orthogonal polarisations of all diffracted orders which are not evanescent. All diffracted orders are used to calculate the electrical and magnetic field distributions in real space which are complex vector functions that vary in 3 dimensions.

2.4 The surface plasmon resonance as 2-dimensional light

In this section, a phenomenological introduction to the surface plasmon resonance is presented. From experimental observations on gratings (2.4.1) and special planar systems (2.4.2), the existence of a surface wave on the metal-dielectric interface can be deduced. This wave has a well defined in-plane wavevector for a given angular frequency ω. Some properties of the surface plasmon resonance in the easiest case of a flat interface between an infinitely thick metal and an infinitely thick dielectric are discussed in 2.4.3. Finally, after revealing some limitations of the approach of a plane surface wave (2.4.4), the importance of the alternative approach of rigorous modelling is highlighted in 2.4.5. The aim of this chapter is to give an introduction to the basics of the surface plasmon resonance. Special properties that are investigated in this work are introduced in the corresponding chapters.

2.4.1 Grating coupling

In 1902, Wood observed in the classical mount that under certain angles of incidence the intensity of the light reflected from a metallic diffraction grating is significantly reduced at certain wavelengths for TM polarisation [Woo02]. A qualitative explanation of these observations was given by Fano [Fan41] almost 40 years later who postulated ‘superficial waves which are excited by the impinging wave on the surface of the grating’. In Fig. 2.7, the measured reflectivity of a metal grating is shown as a function of the polar angle θ of the incident light. The reflectivity is defined as the fraction of the incident intensity which is specularly reflected.

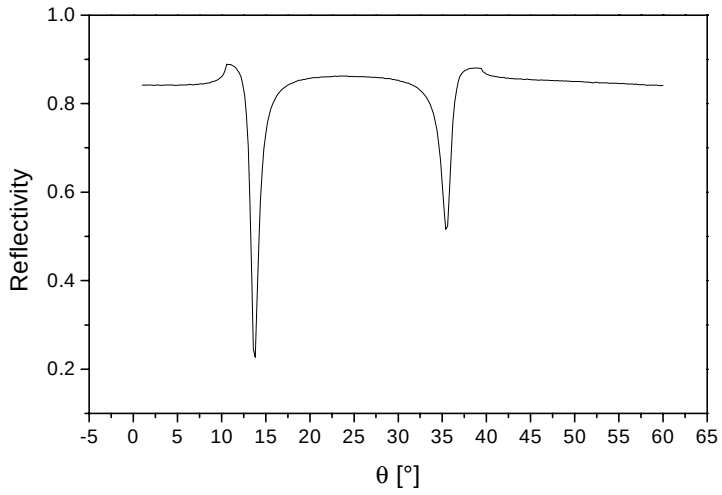

Fig. 2.7: Reflectivity of a gold grating with Λ = 773.6 nm at a wavelength of λ = 632.8 nm and TM polarised light in the classical mount (Ψ = 0°).

Clearly, the reflectivity is reduced at $\theta = 13.7°$ and at $\theta = 35.5°$. Furthermore, for $\theta = 10.6°$ and for $\theta = 39.4°$, sharp kinks are observed. These kinks are due to the transition of a diffracted order from a plane to an evanescent wave. It is straightforward to show with the aid of equation (2.17) that the -2nd diffracted order is a propagating wave only for $\theta > 39.4°$ while the +1st diffracted order is a propagating wave only for $\theta < 10.6°$. These kinks are referred to as 'pseudocritical edges' because they are originating, like the critical edges in the reflectivity from an interface separating two media of high and low refractive index from the transition of a light beam from a plane to an evanescent wave. The two minima can be explained by the existence of an electromagnetic wave which is excited whenever a diffracted order has an in-plane wavevector of a given length. From the data, the in-plane component of this wave is determined as $k_{||} = 1.055\, k_0$. The resonance at $\theta = 13.7°$ is excited by the evanescent +1st diffracted order while the resonance at $\theta = 35.5°$ is due to the evanescent -2nd diffracted order. At this point it can be readily seen that this electromagnetic wave is bound to the interface (evanescent) because with a $k_{||} > k_0$ equation (2.17) immediately yields a purely imaginary z-component of the wavevector.

In the conical mount ($\Psi \neq 0$), this approach of momentum matching in the surface plane is equally well suited to describe the position of the pseudocritical edges and the surface plasmon resonance minima. In Fig. 2.8, measured positions of surface plasmon-related minima and pseudocritical edges are compared to the positions that are obtained by momentum matching of the diffracted order to the surface plasmon resonance with a fixed $k_{||} = 1.055 \times k_0$.

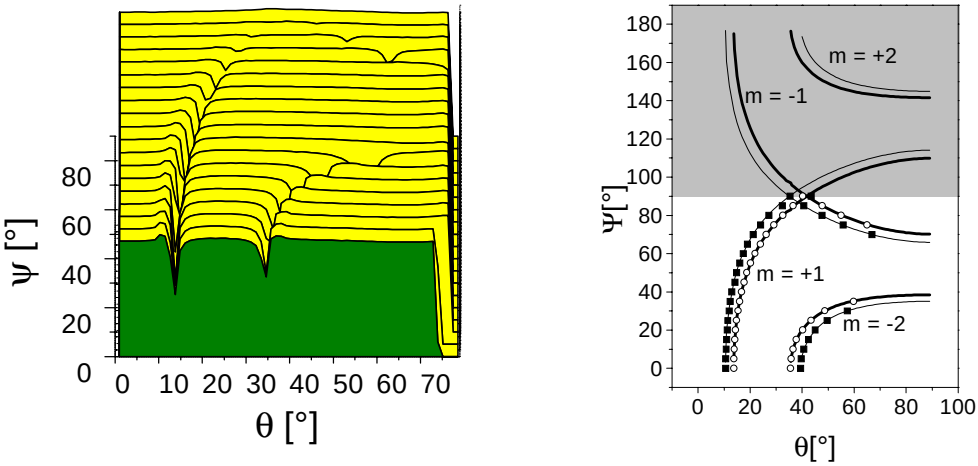

Fig. 2.8: Left: Measured TM-reflectivity of a gold grating as a function of θ and Ψ
Right: Positions of Wood anomalies as obtained from momentum matching and from the measurement: surface plasmons (measured: open circles, geometrical: thick line) and pseudocritical edges (measured: full squares, geometrical: thin line)

A good agreement between measurement and calculation is observed with respect to the position of the surface plasmon resonance and the pseudocritical edge. The depth of the minimum cannot be predicted by momentum matching as well as the vanishing of the

dip for Ψ = 90°. These effects will be treated in some detail in chapter 7. It should be noted, too, that the momentum-matching approach fails for the resonances at Ψ = 90° even if they are excited. A deeper analysis of this 'photonic band gap' is given in chapter 5.

2.4.2 Prism coupling

An alternative way to excite the surface plasmon resonance on a planar metal surface is based on the momentum enhancement of light in a high-index medium to establish coupling to the long $k_{||}$ of the surface plasmon resonance.

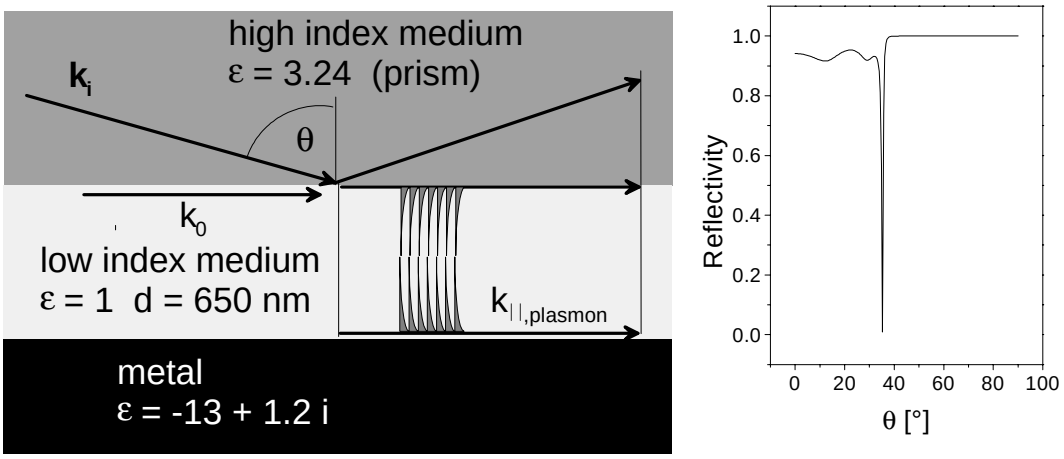

Fig. 2.9: Left: sketch of the planar system and the wavevectors involved in prism coupling in the Otto-geometry.
Right: the θ-dependent reflectivity that is obtained from a model calculation assuming λ = 632.8 nm and the layer system as indicated in the sketch.

Otto [Ott68] demonstrated that coupling to the surface plasmon resonance is possible with the aid of a 3-layer-system as depicted in Fig. 2.9 (left). Resonant excitation of the surface plasmon is achieved on the metal surface through the gap of low refractive index where the two evanescent fields overlap. At a certain angle of incidence θ, the projection of the wavevector of the incident beam matches the plasmon wavevector and coupling between the two electromagnetic waves is established. On the right, the θ-dependent reflectivity as obtained from a model calculation based on a transfer-matrix calculation is shown. A deep and sharp minimum is observed that is due to coupling to the surface plasmon. Since the high index medium must be a prism for geometrical reasons, this method to excite surface plasmons is referred to as 'prism coupling in the Otto configuration'. The precise values of dielectric constants and thickness are chosen for illustrative purposes, different values are common.

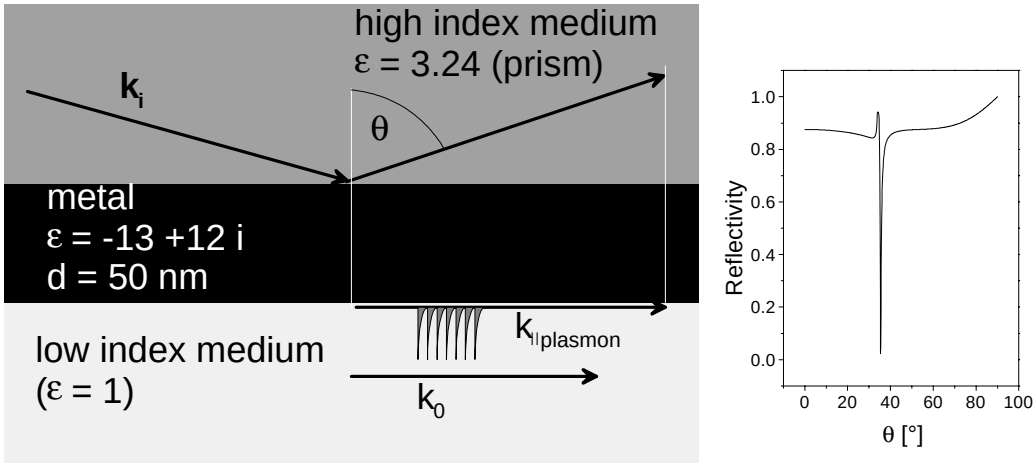

Fig. 2.10: Left: sketch of the planar system and the wavevectors involved in prism coupling in the Kretschmann-geometry.
Right: the θ-dependent reflectivity that is obtained from a model calculation.

Kretschmann [Kre71] found a similar behaviour of the structure that is depicted in Fig. 2.10. Again, coupling to the surface plasmon resonance leads to a well pronounced minimum in the reflectivity. Here, the surface plasmon is excited through a thin metal film. Please refer to [Aus94], [Kno97], [Kno98], Kno91], [Rae88], [Sam91], [Yea96] or [Bur74] for a deeper treatment of prism coupling.

2.4.3 The plane interface between two infinite media

In the last two sections it became evident that the existence of the surface plasmon resonance which is an electromagnetic surface excitation with a well-defined wavevector for a given frequency is very helpful for the understanding of the results of optical experiments[1]. In some sense, the z-component of this resonance may be disregarded which leads to the interpretation of the surface plasmon as 2-dimensional light. A modulated interface between two infinitely thick media may be regarded to a first approximation as flat with the modulation as a perturbation. Similarly, in the prism coupling set-up one may treat the finite thickness of the gold (Kretschmann-configuration) or of the air gap (Otto configuration) as perturbation to the case of two infinitely thick media. The mathematics for this system is relatively easy which makes it worth discussing some properties of the plasmon resonance in this simple model case.

The existence of the surface plasmon resonance as an electromagnetic wave can be derived by an analysis of Maxwell's equations on a planar metal-dielectric interface. It turns out that there is an electromagnetic wave which decays exponentially away from the interface both into the dielectric and the metal with a magnetic field distributions according to equation (2.5) where the magnetic field vector $\mathbf{H_0}$ is parallel to the

[1] Some recent extensions of this concept to a corrugated metal film of finite thickness are reported by Schröter et al. [Sch99].

interface, and the in-plane component $k_{||}$ of the wavevector is given by the dispersion relation:

$$k_{\parallel}(\omega) = k_0 \sqrt{\frac{\varepsilon_m(\omega) \cdot \varepsilon_d(\omega)}{\varepsilon_m(\omega) + \varepsilon_d(\omega)}} \qquad (2.19)$$

where the subscript 'm' stands for metal and 'd' for dielectric. For the detailed derivation of this equation, please refer to the literature e. g. the book of Raether [Rae88]. One important observation is made on this dispersion relation: in order to obtain an in-plane wavevector $k_{||}$ which exceeds k_0, it is necessary to have dielectric constants with opposite sign. This is the case in metals due to the 'plasma-like behaviour' of the electron gas (compare section 2.2). Because of that and the confinement to the interface, the term 'surface plasmon' was chosen.

One way to prove the existence of this resonance experimentally without a grating or by introducing a finite thickness of one of the two media is the scattering of electrons from a metal surface [Rae88]. The transferred energy and momentum can be determined and it turns out that one possible scattering process is the excitation of surface plasmon quanta. This shows that, even when it is not detectable by optical means, the surface plasmon resonance is a fundamental excitation of the surface.

2.4.4 Limitations of the momentum matching approach

In the last section, the surface plasmon resonance was treated as a fundamental excitation of the metal-dielectric interface. The angular positions of minima in the reflectivity can be explained by resonant coupling to the incident light, momentum matching is achieved either by the addition of reciprocal grating vectors in the case of grating coupling or by enhancement of the wavevector of the incident light in a high index medium. This picture is very helpful for the intuitive understanding of the coupling to the surface plasmon. A quantitative treatment of reflectivity measurements in this framework is plagued with the following difficulties:

- It is not clear how the coupling strength of a grating with a given amplitude or of a gold film of a certain thickness can be deduced.
- There are more processes involved than the conversion of light to the surface plasmon. The reversed process must be taken into account as well as all other channels of energy transfer between excitations. For example the observation that in Kretschmann-configuration the reflectivity minimum does not coincide with the maximum field enhancement on the metal-dielectric interface [Lieb99] [Bar85] can be explained by considering the coherent superposition of different channels of energy transfer. This approach has been developed to some extend by Herminghaus et al. [Her94] for plane metal surfaces but a quantitative descriptions turns out to be very difficult with this approach.

- The surface plasmon itself is altered by the introduction of a grating or by changing the thickness of one layer. This effect may be treated in a perturbative way but complicates the calculations significantly. The explanations of effects that are due to the self-coupling of surface plasmons like the ‘photonic band gap’ will be complicated within this framework.

2.4.5 Treatment as purely optical problem

A quantitative description of the optical response of a planar multilayer system is possible with the aid of the transfer matrix algorithm (compare [Kar91]). Only the geometry of the problem and the dielectric constants of the involved materials are required. For a grating, numerical methods like the extended Chandezon method (compare 2.3.2.3) can be applied. The measured reflectivity curves, including reflectivity minima which can be assigned to the excitation of the surface plasmon resonance, are well reproduced by the appropriate choice of parameters (compare chapter 3). It should be noted that it is not necessary to know about the existence of a surface resonance beforehand for the quantitative modelling, the minima appear ‘automatically’. So, this approach, which considers the reflection process as a purely optical problem is fully applicable for a quantitative description of the experimental findings. Nevertheless, the picture of a resonance of well defined dispersion which may be excited by light is much more intuitive. Both approaches should therefore be used for the explanation of experimental data in order to combine mathematical accuracy with intuitive insight.

3 Experimental

Some background information about the experimental techniques that are important for the investigation of the interaction of light with modulated metal surfaces is given in this chapter. First, the preparation of metallic grating surfaces is described in 3.1. Slightly different approaches are used to obtain shallow structures with a depth-to-pitch ratio smaller than 0.1 and deep structures. The experimental set-up that was used to record the optical response of the gratings is introduced in 3.2. Finally, in section 3.3, some remarks are made concerning the optical characterisation of the grating surface. Some special experimental techniques which are applied only in the experiments which are dealt with in one chapter will be described there.

3.1 Preparation of gratings

3.1.1 Small amplitude

The major steps in the production routine for shallow gold gratings are depicted in Fig. 3.1. The grating structure is written into photoresist by a holographic technique and transferred into the surface of a glass slide by standard photolithographic procedures. Only a thin gold layer is responsible for the optical properties of the surface. This gold layer may be removed and the substrate may be reused several times.

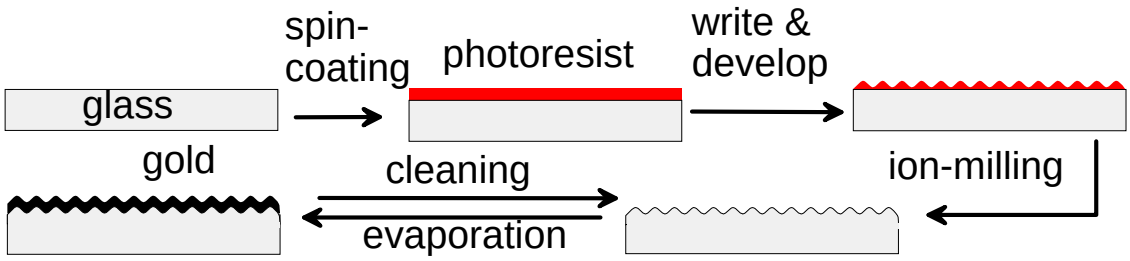

Fig. 3.1: The production of shallow gold gratings. The amplitudes of the gratings are not to scale.

In the following subsections, details of the different steps are explained. The complete sample preparation was done in the cleanroom of the Max-Planck-Institut für Polymerforschung in Mainz (class 100).

3.1.1.1 Preparation of the substrate

A fused silica slide (Hellma, optical quality) is carefully cleaned by the following procedure:

- 10 × rinsing in purified water (Milli-Q, Millipore)
- 15 minutes cleaning in the ultrasonic bath in a solution of 2% detergent (Hellmanex, Hellma) in purified water

- 15 × rinsing in purified water
- 5 minutes cleaning in the ultrasonic bath in ethanol (Fluka)
- Drying of the slides in a flow of nitrogen. For optimum results the ethanol should withdraw from the glass surface as a compact lamella.

3.1.1.2 Deposition of photoresist

As a next step, a photoresist layer (Shipley microposit) is deposited on the glass surface by spin coating. In order to enhance the adhesion of the photoresist to the surface, the glass surface is pre-treated with liquid hexamethyldisilazane ('Primer', Shipley). Best results were obtained by heating the glass close to the evaporation temperature of the primer. The glass slide is put on the spin-coater and the surface is completely wetted with the primer solution. After 30 s the remaining solution is removed by spinning the sample at moderate speed (2000 rpm). Immediately afterwards the photoresist is applied to the resting sample. The thickness of the photoresist layer is tuned by dilution in 'thinner' (Shipley) and by adjusting the rotation frequency of the spin-coater. For symmetric grating structures a thickness around 100 nm is favourable because of the enhanced stability of the photoresist. For highly asymmetric gratings, though, it is necessary to use a very thin photoresist layer (40-50 nm). Thick photoresist films are dried for 30 minutes under vacuum at 95° C (softbake). For very thin films, this step is not necessary.

3.1.1.3 Writing of the grating structure

In this work, a method for the fabrication of relief gratings in photoresist was used that was first reported by Mai et al. [Mai85]. The sample is mounted in the optical set-up that is depicted in Fig. 3.2. The beam of a TE-polarised He-Cd laser (λ_{HeCd} = 442 nm, Optilas) is passing through a spatial filter which produces a parallel beam which does not show significant variation in intensity in the vicinity of the optical axis over an area of a few cm^2.

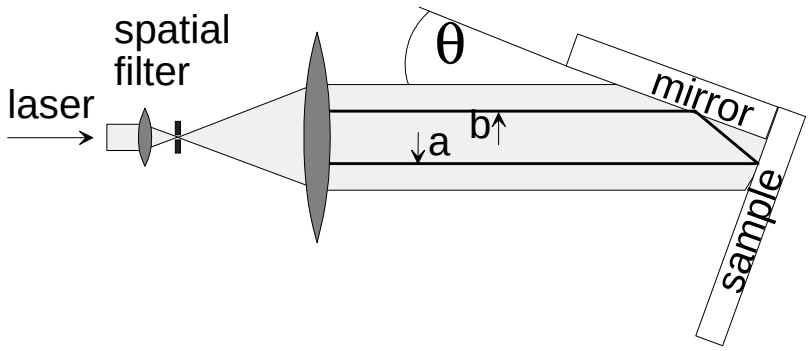

Fig. 3.2: The optical set-up that is used to prepare holographic gratings.

While one half of the beam (ray a) is incident directly on the sample, the other half (ray b) is reflected by a mirror. Depending on the phase difference between these two possible paths there may be either constructive or destructive interference on the sample

surface. Ideally, the intensity distribution on the grating surface is sinusoidal with a period Λ that is given by

$$\Lambda = \frac{\lambda_{HeCd}}{2 \cdot \sin(\theta)} \qquad (3.1)$$

as it can be shown with elementary geometry. The polar angle θ is defined as the angle between the optical axis and the normal of the sample surface (compare Fig. 3.2).

Care must be taken to avoid the interference effects with laser light which is reflected from the backside of the glass slide. Black adhesive tape on the backside of the sample helps to reduce the intensity of this unwanted light.

In the intensity maxima of this interference pattern, the photoresist undergoes a photochemical reaction, which leads to solubility of the material in the developing reagent while photoresist that was not illuminated remains insoluble. Developing this structure leads to a surface relief grating in the photoresist. A coherent photoresist layer with a modulation of the surface may be obtained by exposing the sample only shortly to the laser light or by choosing a short developing time. This structure is needed for the production of highly asymmetric gratings. Longer times lead to separated stripes of photoresist with areas of bare substrate in-between. For the production of symmetric gratings, such structures are required.

3.1.1.4 Reactive ion beam etching

By exposure to an ion beam, the photoresist grating is transferred into the glass substrate. A sketch of the ion mill (Roth & Rau) is found in Fig. 3.3.

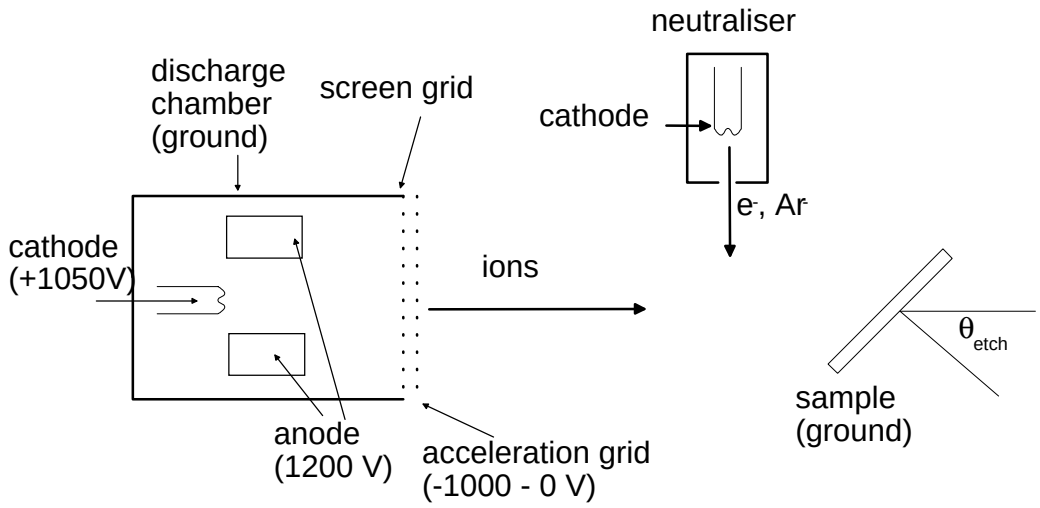

Fig. 3.3: Sketch of the ion mill.

The ion mill supplies accelerated ions that bombard the sample surface. In detail this works as follows:

A dilute mixture of gases (O_2 and CF_4) is flowing into the discharge chamber. Electrons which are emitted by the cathode are accelerated towards the anode and by scattering

gas molecules are ionised. So, inside the anode ring, a plasma is built which lies at a high positive potential. The numbers given in the sketch are for illustrative purpose and values different from those are common. Positive ions are accelerated towards the screen grid which lies on ground potential. A second grid (acceleration grid) where a potential between 0 V and -1000 V may be applied allows focusing of the beam. The ion beam finally reaches the sample (which is at ground potential) with a kinetic energy corresponding to the potential of the anode. The neutraliser adds negative ions and electrons to the beam in order to avoid charging of the sample. By adjusting the orientation of the sample relative to the ion beam an anisotropy may be introduced to the etching process.

For symmetric gratings the etching angle θ_{etch} is adjusted to 0° (normal incidence of the ion beam). For the shallow asymmetric gratings θ_{etch} up to 80° were used to obtain the high anisotropy that is needed for the measurements that are presented in chapter 6. Best results for the highly asymmetric, shallow gratings were obtained by etching for 1 minute at θ_{etch} = 0° first (ablation of 20 nm photoresist and 40 nm glass) before switching to the high θ_{etch}. The asymmetric gratings are etched long enough that no photoresist remains on the glass. They are therefore immediately ready for the next step. On the symmetric gratings there are some residues of photoresist which are removed in warm acetone.

The combination of reactive gases (O_2 and CF_4) is optimised for the etching of fused silica where a mechanical ablation (sputtering) and a chemical etching by the radicals that are deduced from the reaction gases takes place. As a consequence, the etching efficiency depends on the partial pressures of gases for glass. The ablation of other materials as gold or chromium is a pure sputtering process and no influence of the chemistry of the gases could be observed.

3.1.1.5 Evaporation and removal of the metal coatings

A gold layer (Balzers, purity 99.99%) is thermally evaporated onto the sample in a commercial evaporation chamber (Balzers). By choosing a thickness exceeding 150 nm, the gold layer can be assumed as infinitely thick for the optical analysis. The adhesion of the gold to the silica substrate may be enhanced by a thin (3 nm) layer of chromium (Balzers, purity 99.9%) between gold and glass which is thermally evaporated in the same chamber. After the experiment, the gold layer is removed with aqua regia (mixture of HCl and HNO_3 in the ratio 3:1). The chromium layer is removed with an aqueous solution of ammonium cerium (IV) nitrate (Aldrich, purity 99 %, 12 g in 50 ml water).

3.1.2 Deep gold gratings

3.1.2.1 Preparation routine

In order to obtain gratings that are as deep as possible, the standard process for the production of holographic gratings that was described in the previous section had to be

modified. A schematic overview over the different steps of the production routine is shown in Fig. 3.4.

Standard microscope slides (obtained from Menzel) are carefully cleaned (compare 3.1.1.1) and by thermal evaporation a thin chromium layer followed by a ca. 1000 nm thick gold layer and another chromium layer with a thickness of 200 nm are deposited on the sample. The first chromium layer enhances the adhesion of the gold to the surface, the second is chosen as masking material because it is very resistive to ion-etching processes (The etching rate in Au is roughly 4-5 times higher than in chromium). For the production of highly asymmetric gratings, a large contrast in etching resistance between mask and the material where the structure is finally written is needed. Such thick gold layers are required because the gratings have a very high amplitude and, in order to simplify the evaluation, the gold should be thick enough to allow the assumption of an infinite thickness. The evaporation materials were obtained from Balzers with a purity of 99.99 % (Au) and 99.9 % (Cr).

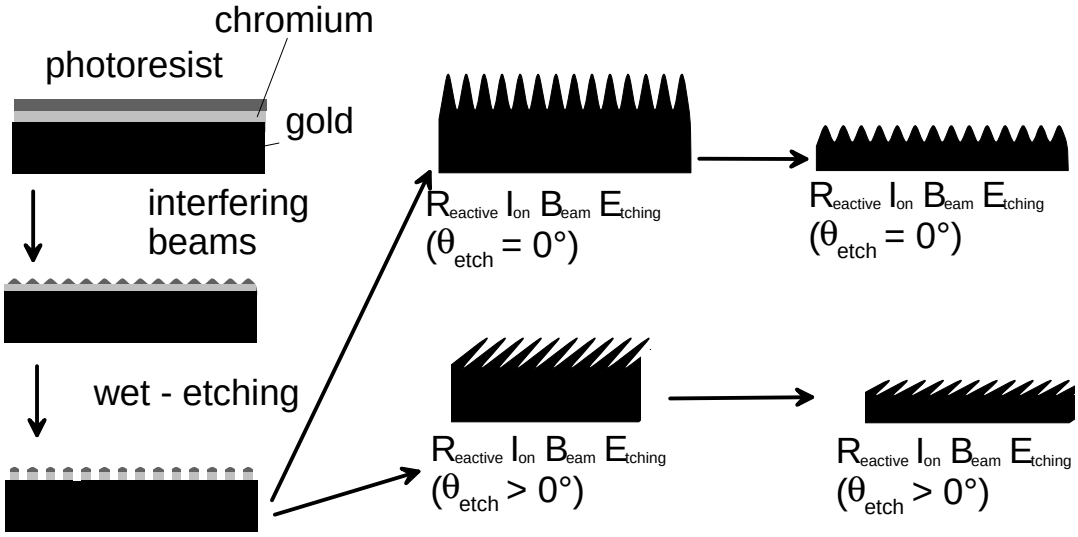

Fig. 3.4: Sketch of the different steps for the preparation of the deep gold gratings.

This system serves as support for a photoresist film (Shipley Microposit) of 100 nm thickness which is deposited by spin coating (compare 3.1.1.2) without application of primer. A holographic grating is written into the photoresist. The development is long enough to ensure that the photoresist structure has already evolved from a coherent layer to separated stripes. Subsequently, the sample is exposed to an aqueous solution of ammonium cerium (IV) nitrate (Aldrich, 99 %, 12 g in 50 ml water) for 70 seconds. This step serves to transfer the photoresist structure into the chromium. As a next step, the sample is treated by reactive ion beam etching (see 3.1.1.4) until the chromium is completely etched away. By choosing the etching angle θ_{etch} (angle between the direction of the ion beam and the surface normal of the grating, compare Fig. 3.3) between 0° (normal incidence) and 40°, gratings with different degrees of asymmetry can be obtained. The orientation of the grating is chosen so that the ion beam is orthogonal to the grating grooves.

To some extend, the grating amplitude can now be decreased by etching further into the pure gold grating.

3.1.2.2 Characterisation

The gratings that were produced this way were characterised with a scanning electron microscope (leo 912) in order to obtain as much information about the shape of the grating profile as possible. The samples are broken along a line orthogonal to the grating grooves from the backside of the substrate. This is followed by focusing the objective of the electron microscope onto the freshly cleaved edge at an angle of 5° relative to the normal of the cleaved surface. This allows the surface profile to be read from these images without applying a stretching factor. Fig. 3.5 shows the grating profile for different etching angles.

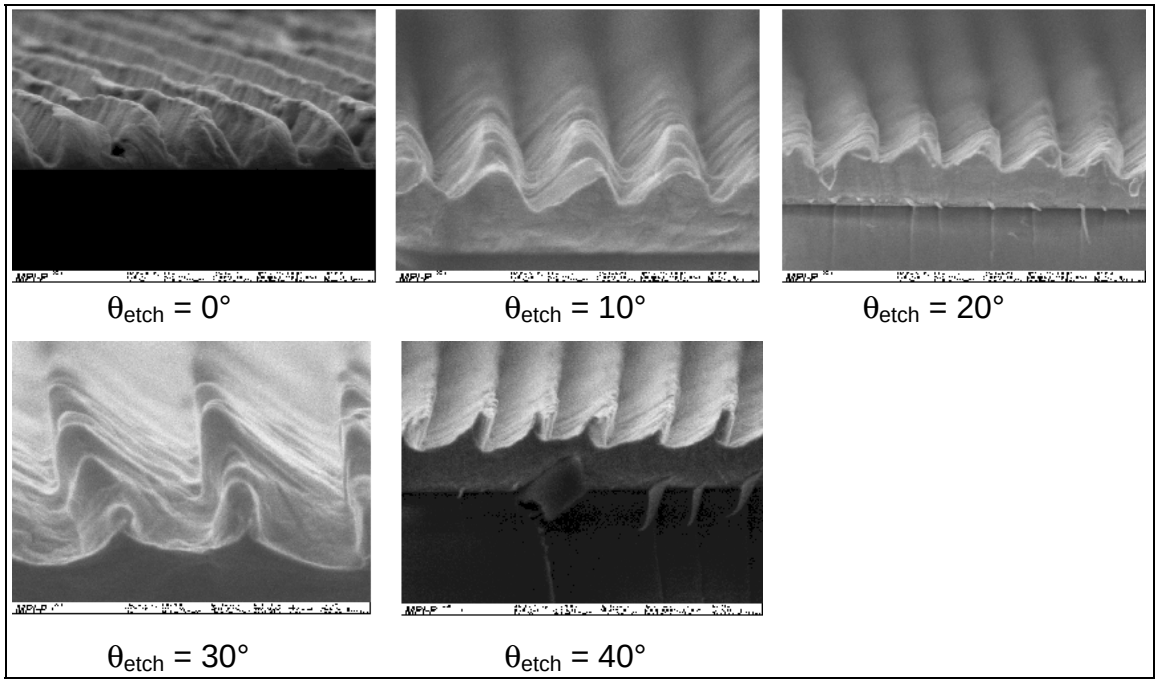

Fig. 3.5: Electron micrographs of grating structures that were obtained by etching under the angles that are indicated on the graphs. The grating period is Λ = 700 nm.

It is clearly seen that with this technique, it is possible to obtain gold gratings with a depth-to-pitch ratio close to 1. The grating shape can be varied from a mirror symmetric profile when etched under 0° to overhanging structures when etched under 40°. From images like these, the grating shape had to be extracted. This was done by drawing a curve by hand into the images that reproduced the surface profile as good as possible. This curve was then transformed into discrete points z(x). A least squares-fit to the average of five data sets that were obtained on different grating peaks gave finally the parameters for the description of the profile. The first three amplitudes A_i and phases φ_i of the Fourier sum and the oblique angle θ_{ob} (compare chapter 2) were obtained that way. One major disadvantage of this characterisation technique should be mentioned: the sample must be destroyed to allow a measurement. Therefore, it was not possible to

characterise the identical sample for different exposure times in the reactive ion beam etcher.

3.2 Optical set-up for reflectivity measurements

The reflectivity of the gratings was measured for linearly polarised light as a function of the wavelength λ, the polarisation φ and angle of incidence (θ, Ψ) of the incoming light.

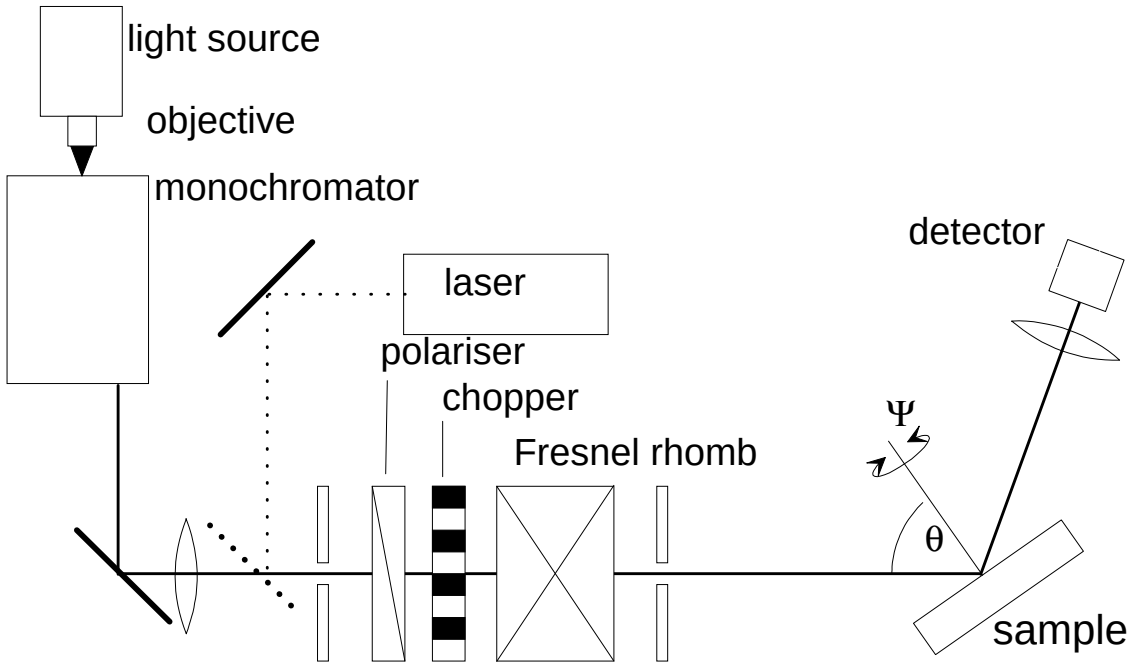

Fig. 3.6. Sketch of the optical set-up for reflectivity measurements.

In Fig. 3.6 the optical experimental set-up is shown schematically. The light of a Xenon light bulb (Osram Xenophot, 300 W in a Müller SVX 1530 housing) is collimated by an objective onto the slit of a grating monochromator (Chromex 250 SM). After its exit slit, a lens turns the light into a parallel beam. Linear polarisation is fixed by a Glan-Thompson polariser (OWIS) and the polarisation plane can be deliberately rotated with a Fresnel rhomb (Bernhard Halle). Two pinholes select the components of the beam which are close to the optical axis and are therefore almost parallel. A laser beam (HeNe, $\lambda = 632.8$ nm, Uniphase 1125P) is coupled into the optical path with a removable mirror. It serves both for the optical alignment in experiments where the wavelength of the incident light is varied and as a light source for reflectivity measurements with monochromatic light.

The sample is fixed on a goniometer (sample-goniometer) (Huber) that allows variation of the polar angle θ. For $\theta = 0°$, the sample surface is orthogonal to the incident beam. The axis of this goniometer coincides with the sample surface. A second goniometer (Ψ-goniometer) (Spindler & Hoyer) is mounted on top of the first one. For $\theta = 0°$, its axis is coincident with the incoming beam. It allows the variation of the azimuthal angle Ψ which is counted as clockwise rotation of the sample viewed along the incident beam

and which is 0° when the grating grooves are perpendicular to the drawing plane. By comparison with Fig. 2.4, the geometry may become clearer.

The specularly reflected light is focused onto the detector by a lens with a focal length of 50 mm. These two components are mounted on a third (detector-) goniometer (Huber) on an optical bench. The axis of this goniometer coincides with the one that varies θ. It tracks the direction of the reflected beam in θ/2θ geometry. The detector is either a silicon-photodiode (for λ = 500 to 1100 nm) or a germanium-photodiode (for λ = 1000 to 1800 nm)

The incoming beam is chopped at 1234 Hz and the voltage signal from the photodetector is analysed by a lock-in amplifier (EG&G, model 7260) with this frequency as reference signal. The three goniometers, the Fresnel rhomb and the monochromator are controlled by a PC. The output of the lock-in amplifier is also fed to this PC.

The spectral intensity for the two fundamental polarisations of the incoming beam is recorded by adjusting the detector goniometer to 180° and removing the sample. In order to measure reflectivities of the sample the readings of the lock-in in a reflection experiment are normalised to this reference. While the output power of the laser is relatively stable over time, there are significant drifts in the intensity spectrum of the combination of white light source and monochromator. Therefore, those reference spectra must be taken at the same day as the reflected intensities.

3.3 Optical characterisation of a grating

The parameters that determine the optical response of a metal grating without additional coatings are the grating period Λ, the dielectric constant ε of the gold and the shape of the grating profile which is expressed as a Fourier sum with phases φ_i and amplitudes A_i.

The grating period is easily determined in the 'Littrow mount' which is defined as the position of the grating where the -1st diffracted order is propagating back in the direction of the incident beam. In this case, obviously Ψ = 0° holds and basic geometry shows that the grating period can be calculated from the Littrow angle θ_{Lit} by the following equation:

$$\Lambda = \frac{\lambda}{2 \cdot \sin\left(\theta_{Lit}\right)} \qquad (3.2)$$

where λ denotes the wavelength of the incident light.

The remaining parameters are determined by a least square fit to the data. This procedure is illustrated by taking the data set as an example that was already used to illustrate coupling to the surface plasmon in chapter 2.4.1.

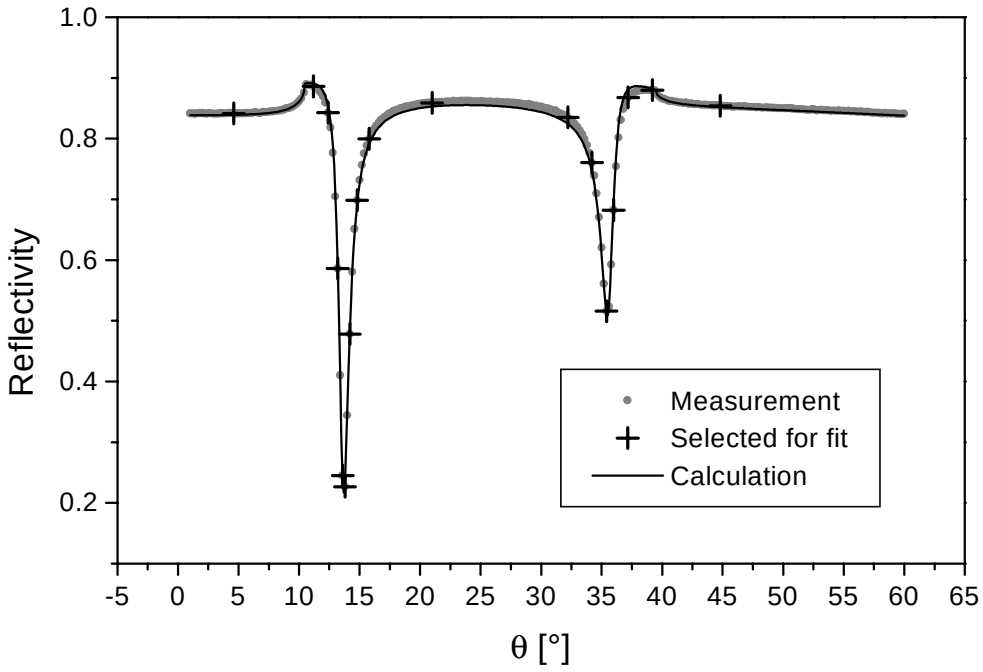

Fig. 3.7: Reflectivity of a grating with a pitch of Λ = 773.6 nm which was illuminated with a TM-polarised HeNe laser (λ = 632.8 nm). The fit yields ε = -10.37 + i 1.014, A_1 = 19.82 nm, A_2 = 5.98 nm, φ_1 = 40.3°, A_3 = 2.97 nm, φ_2 = 46°.

It turns out that 3 Fourier components are sufficient to obtain a reasonable fit to the measured points. A computer program, based on the 'oblique' code calculates the sum of squares of the difference between the measured reflectivities of up to 20 selected pairs (R, θ) and the modelled reflectivities based on a certain set of parameters. By variation of the fitting parameters within a pre-defined range, the set of parameters which leads to a minimum deviation from the measured results is stepwise approached. For details of the fitting algorithm, the reader is referred to the thesis of Wanstall [Wan99].

In the case of a grating profile which was etched symmetrically, the phases of the higher Fourier components may only take discrete values. For a φ_1 which is chosen as 0, φ_2 may equal either 90° or 270°, φ_3 may be 0° or 180° and so on (compare chapter 5). Therefore, this parameter should be kept constant during the fit. The real value may then be determined by comparing the results of fitting routines with the different possible choices. Alternatively, φ_2 may be determined by mapping of the photonic band gap which is composed of two coupled resonances. On symmetric gratings there is always one of the two coupled resonances suppressed, which one is determined by φ_2. For more information regarding the photonic band gap, the reader is referred to chapter 5 and chapter 6. It is important to note that the set of parameters that gives an optimum description of the experimental results does not necessarily yield exactly the real shape

of the grating profile. This is illustrated in Fig. 3.8. It is not very reasonable that such a profile would be obtained by the preparation technique that was described above.

This difference between the real grating profile and the one that gives an optimum description of the data can be interpreted as an effect of the roughness of the sample which is not accounted for in the numerical modelling code. An overestimation of the higher harmonics of the grating profile leads to short-pitch modulation of the profile. It seems that this periodic roughness has a similar effect on the reflectivity as random scattering.

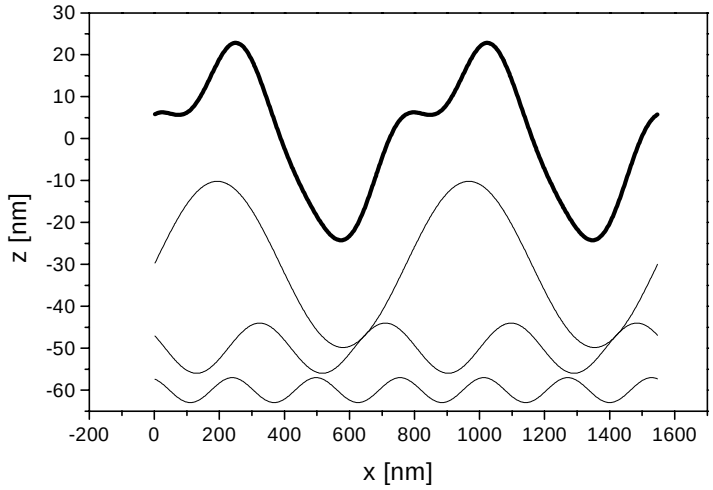

Fig. 3.8: Grating profile as it is deduced from the fit to the data (thick line). The individual Fourier components are plotted below the sum profile as thin lines.

This interpretation is supported by the analysis of the impact of variation of the fitting parameters on the quality of the fit. By model calculations under variation of these parameters, it turns out that small changes in A_1, A_2 and φ_2 will lead to a significant decrease of the quality of the fit. Especially in $\Psi = 90°$ geometry (compare Chapter 5) the gap between the coupled resonances as well as their relative strength depend strongly on these parameters. Variations in φ_3 do not lead to significant changes. This allows the conclusion that the first two components of the Fourier representation reflect the real grating profile. The third order as an additional fitting parameter is necessary for a good model calculation, it accounts for both the real effects of the third harmonic component and for roughness effects. Because of the weak influence of φ_3 on the reflectivity, the surface profile as it is reconstructed, including the third component, deviates from the real geometry.

It should be mentioned that to a good approximation the amplitude of the i'th order of the grating profile is responsible for the coupling to the surface plasmon resonance in i'th diffracted order. For this reason, on gratings with bigger Λ where surface plasmon resonances in higher diffracted orders can be observed, the determination of more

Fourier components of the grating profile is possible by a fit to the reflectivity. Similarly, it is difficult to obtain much information about the profile of a grating with a short pitch as it is used for the experiments that are described in chapter 4 and chapter 8. Detailed descriptions of the fitting process as well as comparisons to real grating profiles that were determined independently by scanning probe methods can be found in literature [Woo95], [Wat97], [Wat97b].

4 Thermally induced emission of light from a metallic diffraction grating, mediated by surface plasmons

4.1 Introduction

It is well known that good light absorbers are good emitters when they are heated; a black body shows the highest output of radiation at a given temperature. This fact is called Kirchhoff's law and is treated in most standard textbooks on physics like [e. g. Ger82].

On metal gratings, due to the resonant excitation of surface plasmons a strong angular variation of the reflectivity is observed. The fraction of light which is absorbed upon reflection may vary between about 10 % outside resonance up to ideally 100 % when the surface plasmon resonance is excited. As a consequence, a reciprocal angular variation in emission is expected. Observed under the angle of vanishing reflectivity due to surface plasmon excitation, the metal grating should have the emission properties of a black body for the corresponding wavelength. Fig. 4.1 shows how the underlying processes may be qualitatively understood in a simplified picture. In a reflection experiment, some fraction of the light is lost due to 'direct absorption' of the incident radiation. This contribution is independent from the existence of a grating. In the long-wavelength regime of the visible light, less than 10% of the incident light is lost in this decay channel. Under certain angles an additional strong process may be observed which is sketched in Fig. 4.1 (a) the light is transformed to a surface plasmon by adding a reciprocal grating vector. The energy of the surface plasmon is then finally transformed into heat by absorption within the gold. When the thermal energy of the metal is high enough, the same processes in the reversed direction may have a significant probability as shown in Fig. 4.1 (b): the thermal energy may be transformed directly into plane electromagnetic radiation which is not expected to show a strong angular variation. This is the glowing that would be observed from a not-modulated gold surface as well. Additionally some of the surface plasmon states are populated according to Boltzmann's law and these electromagnetic waves may pick up the pseudo-momentum corresponding to a reciprocal grating vector and leave the sample as light. This contribution is expected to be strongly angle-dependent.

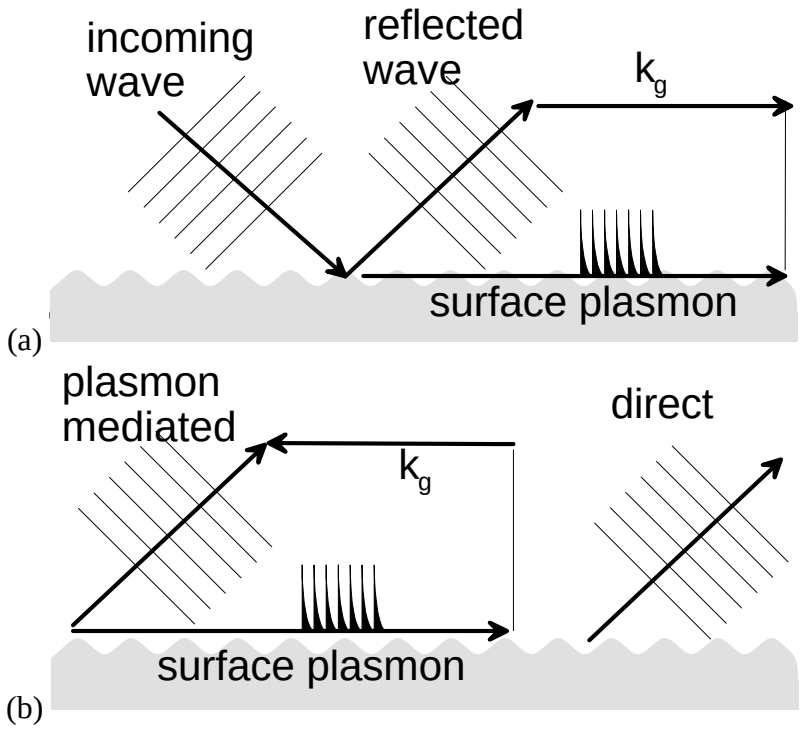

Fig. 4.1: Processes of energy transfer between light and thermal energy of a metal grating.
(a) Loss of energy in a reflection experiment due to intermediate excitation of the surface plasmon resonance. Additionally, direct absorption may take place.
(b) Processes that lead to light emission from a hot sample. Either direct emission or the intermediate excitation of the surface plasmon may take place.

It is the goal of this chapter to demonstrate this effect experimentally. First, details of the sample preparation are given and the experimental set-up is described. Then, the measured angle dependent emission is compared to the reflectivity at the corresponding wavelength.

4.2 Experimental

4.2.1 Sample preparation

A grating with a pitch of Λ = 484.9 nm was fabricated on a fused silica substrate as described in chapter 3.1. A gold film with a thickness of 140 nm was thermally evaporated onto the grating. A thin (3 nm) chromium layer between the glass and the gold prevented dewetting of the gold at temperatures up to 700° C. The grating was optically characterised by a reflectivity measurement in the classical mount as described in chapter 3.2.

4.2.2 Emission measurement from the grating at 700°C

The experimental set-up that was used to record the intensity of light at certain wavelengths emitted from the gold grating is shown schematically in Fig. 4.2. The grating is fixed on a turning stage which contains a heating unit that is used to adjust the

sample temperature to roughly 700°C. The grating grooves are perpendicular to the drawing plane (classical mount, $\Psi = 0°$). To avoid chemical reactions, the chamber is evacuated to a pressure of 10^{-3} mbar.

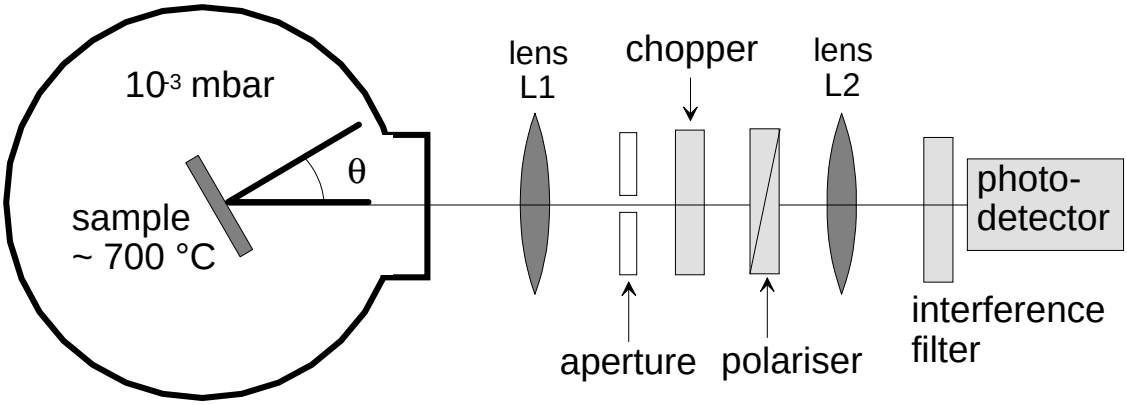

Fig. 4.2: Experimental set-up for angle-resolved emission measurements. Refer to the text for further details.

Light emitted from the grating is passing through the window of the vacuum chamber. Outside the vacuum chamber, an optical bench is set up with its optical axis pointing towards the grating. A lens (L1) collects the emitted light. L1, having a distance of 40 cm to the grating and a diameter of 3.8 cm yields an angular resolution of 2.7°. In the image plane of L1, an aperture is positioned to restrict the area on the sample from which light reaches the photo-detector to the corrugated part. An optical chopper modulates the beam as needed for a lock-in detection technique. Next, a polariser may be brought into the optical path. A second lens (L2) collimates the beam onto the detector, which is positioned behind an interference filter (alternatively maximum transmission at $\lambda = 710 \pm 6$ nm or $\lambda = 810 \pm 6$ nm). The output of the photo-detector is analysed by a lock-in amplifier (EG&G, model 7620) with the chopper frequency set as reference.

The signal of the lock-in amplifier is recorded as a function of the angular position of the surface normal of the gold grating with respect to the optical axis of the detection system (polar angle θ).

4.3 Results

4.3.1 Reflectivity of the grating

The pitch of the diffraction grating was determined in the Littrow mount (refer to chapter 3) to be 484.9 nm. The reflectivity of the grating for TM polarised light with $\lambda = 632.8$ nm as a function of the angle of incidence is shown in Fig. 4.3. The grating geometry and the dielectric function of the gold were determined by a least squares fit to the reflectivity (refer to chapter 3). It can be seen that due to the short pitch of the grating, the fit is slightly worse than in the example that was given in chapter 3.3.

Nevertheless, this description is good enough for the following analysis. Based on this data, model calculations of the reflectivities at the wavelengths of the emission experiments were performed. The surface profile was used as obtained from the fit to the reflectivity data at 632.8 nm. Since the dielectric constant ε of gold depends on the frequency of the electromagnetic radiation as well as on the temperature, an estimate has to be made for ε for the wavelength and temperature of the emission experiment.

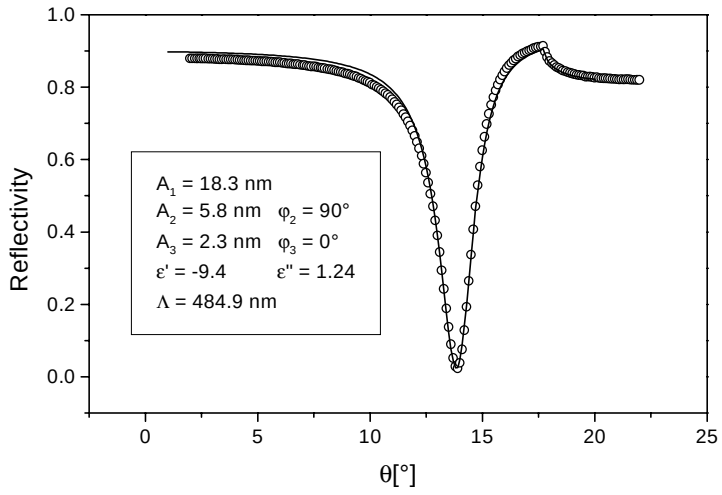

Fig. 4.3: Measured (dots) reflectivity of the grating under investigation at 632.8 nm. The geometrical parameters and the dielectric constant of the gold as determined from the fit are shown in the inset. The line is a model calculation which is based on these parameters.

As a rough estimate, the impact of the change in wavelength on the dielectric constant is determined by linear extrapolation to the wavelength-dependence as given in [Yeh98].

$$\varepsilon_e(\lambda) = \frac{\varepsilon_m(632.8nm)}{\varepsilon_t(632.8nm)} \cdot \varepsilon_t(\lambda) \qquad (4.1)$$

where λ may be 710 or 810 nm and the subscripts stand for ‘extrapolated’ (e), ‘measured’ (m) and ‘tabulated’ (t)[2] respectively.

Reports in the literature on temperature dependent dielectric constants of gold for the wavelengths under investigation are rare. Krishnan [Kri90] found no drastic change in the real part of ε for molten gold at 1400 K compared to the values at room temperature (λ = 632.8 nm and 1064 nm). For that reason, the effect of heating on Re(ε) was neglected. Winsemius [Win76] reports a linear rise of the imaginary part of ε with temperature which is of the order of $1 \cdot 10^{-3}$ K^{-1} for the wavelengths that were used here (710 and 810 nm). Therefore, 0.7 (= 700 K × 10^{-3} K^{-1}) was added to the imaginary part

[2] ε_m(632.8 nm) = -9.4 + i 1.24 from the fit. From the literature, ε_t(632.8 nm) = -10.46 + i 1.11, ε_t(710 nm) = - 15.4 + i 1.05 and ε_t(810 nm) = -22.35 + i*1.43 is found. This yields ε_e(710 nm) = -13.8 + i 1.18 and ε_{te}(810 nm) = -20.1 + i 1.6.

of the dielectric constant of the gold. The values that were finally chosen for the model calculation for T = 700°C are:

$$710\ \text{nm}: \varepsilon = -13.9 + i\cdot 1.88$$
$$810\ \text{nm}: \varepsilon = -20.1 + i\cdot 2.3 \qquad (4.2)$$

4.3.2 Angular dependence of the light emission from a gold grating at 700° Celsius

The emission of light at two different wavelengths, 710 and 810 nm, from the gold-covered grating is shown in Fig. 4.4.

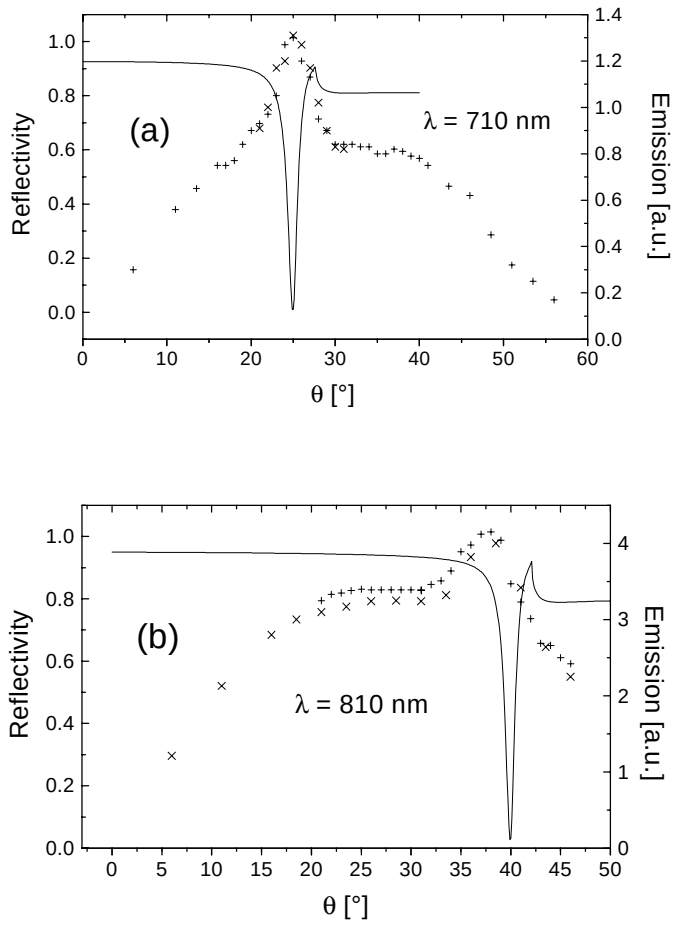

Fig. 4.4: Calculated reflectivity (straight line) and measured emission (crosses) as a function of θ. Different types of crosses correspond to data sets taken with one hour delay. The wavelengths of the experiment are indicated in the graphs.

For both wavelengths there is a large background in the range from θ = 15° to θ = 40°. This background, being constant, implies that the emission direction of this radiation is random. This contribution is attributed to the emission that is due to light ‘directly’ emitted from the gold. The decrease of emission intensity at angles above 40° and below

15° is an artefact due to imperfect experimental geometry. For both wavelengths, there is a distinct emission peak visible, which can be attributed to surface-plasmon-enhanced emission. This is proven by comparing the observed emission peaks to calculated reflectivities for the two wavelengths under investigation, which are plotted as straight lines.

Coupling of light to surface plasmons in a reflectivity experiment would occur in the same angular range where the maximum in emission is observed. From this, it can be concluded that indeed the coupling of thermally excited surface plasmons to light via the grating is responsible for these emission maxima. The widths of the emission peak and the plasmon minimum differ significantly: the emissivity maxima appear to be much broader than the reflectivity minima. This can be attributed to the limited resolution in wavelength and emission angle in the emission measurement, giving an experimental resolution of about 3 degrees. This effect is responsible for the relatively small height of the emission maximum, too. At a wavelength of 810 nm it seems that the emissivity maximum is slightly shifted with respect to the reflectivity minimum. This can be regarded as an artefact which is due to imperfect imaging of the grating onto the photodetector.

4.3.3 Polarisation of the plasmon enhanced emission

In reflectivity measurements, only TM-polarised light couples to surface plasmons in the classical mount. Thus, the radiation due to thermally excited surface plasmons, coupled out by a diffraction grating, is expected to be TM-polarised.

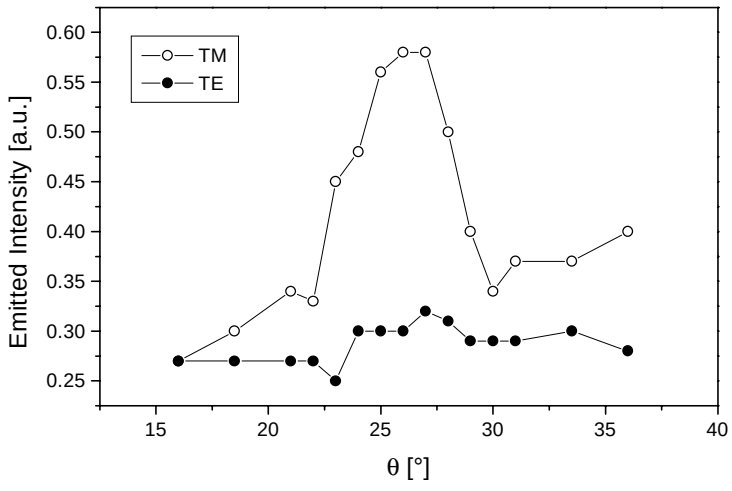

Fig. 4.5: Intensities of the TM-polarised and the TE-polarised component of the emitted light for λ = 710 nm as a function of the polar angle θ of the emission.

The above predicted behaviour was found for the maxima in the emission as it can be seen in Fig. 4.5 for λ = 710 nm where the separately recorded TM- and TE-component

of the emitted radiation are shown. The radiation background which contributed to both polarisations in roughly the same strength does not show a specific polarisation behaviour while the peak due to surface plasmon enhanced emission is purely TM polarised.

4.4 Conclusion

The emission of light in the visible/NIR from an optical gold grating at 700°C was investigated with respect to it's propagation direction and polarisation. For wavelengths of 710 and 810 nm, there is a maximum observed in the emission-angle scan that is purely TM-polarised. From the polarisation behaviour and the analysis of the direction of the emission, these maxima are attributed to thermally excited surface plasmons coupled to light by the grating.

5 Resonances on deep and overhanging gratings

5.1 Introduction

The best known example for coupled surface plasmon-related resonances is observed at normal incidence already on relatively shallow gratings. Fig. 5.1 shows a measurement of the wavelength-dependent reflectivity at finite polar angles θ in the classical mount (Ψ = 0°).

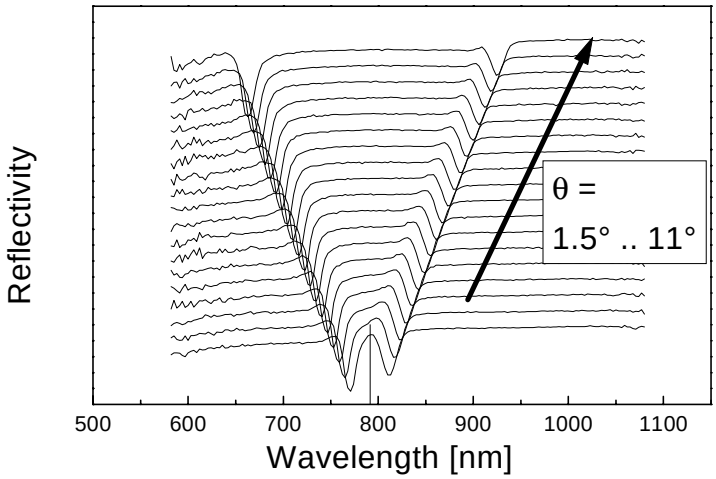

Fig. 5.1: Wavelength-dependent reflectivity for Ψ = 0° (classical mount) and polar angles θ between 1.5° and 11°. The straight, vertical line indicates the wavelength that is reached by both resonances when they are linearly extrapolated to θ = 0°.

Two minima are observed that are due to coupling to the surface plasmon in $+1^{st}$ and -1^{st} diffracted order. Their resonance wavelength as a function of θ can be found with the aid of the momentum matching condition (compare chapter 2.4.1). This implies that the existence of the grating does not significantly influence the dispersion of the surface plasmon, but it allows the exchange of energy with incident plane light waves.

At normal incidence, these two diffracted orders will have equal in-plane momentum due to the symmetry of the experimental geometry. So, naively one would expect only one minimum at 791.5 nm, indicated by the straight, vertical line in Fig. 5.1. Instead, in Fig. 5.2.[3], two minima are observed. One is shifted from the position that would be anticipated from the momentum matching to shorter wavelength and is narrower than

[3] The small deviation from normal incidence along Ψ = 90° has no significant effect on the reflectivity and is necessary for experimental reasons.

the ‘ordinary’ surface plasmon resonance. The other one appears at a longer wavelength and shows a broadening. In analogy to the band gaps of electronic and vibrational states at the Brillouin zone edge of a solid, this splitting is referred to as a ‘Photonic band gap’ [Bar96].

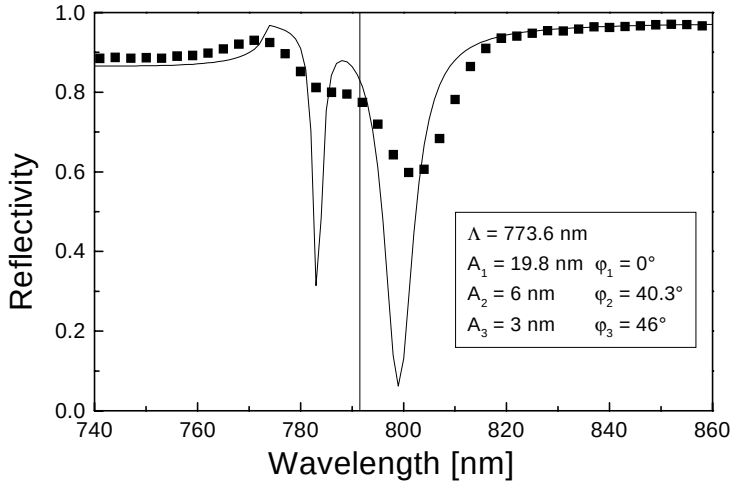

Fig. 5.2: Wavelength-dependent reflectivity for $\Psi = 90°$ and $\theta = 1.5°$, The measured values (dots) are compared to a model calculation (straight line) based on a grating profile which is described by the parameters shown in the inset The dielectric function is assumed as Drude-like with $\omega_p = 1.2 \times 10^{16} s^{-1}$ and $\tau = 7 \times 10^{-15} s$. The position where a resonance would be expected from the momentum matching approach is indicated by a vertical line ($\lambda = 791.5$ nm).

Here, the effect of the grating cannot be reduced to a channel that allows the coupling of light to a surface plasmon resonance which propagates then along the grating like on a plane surface. Instead, there is an additional effect of the surface geometry on the resonances themselves. In order to distinguish these electromagnetic waves from the surface plasmons which behave like 2-dimensional light, they are called ‘coupled resonances’ in this work.

The effect of an increased perturbation of the surface plasmon resonance, due to an increased depth of the grating grooves is explored in this chapter for deep and overhanging gratings. In the next section (5.2), a classification of the expected resonance phenomena is presented, based on model calculations. The theoretical predictions are compared with measurements in chapter 5.3.

5.2 Classification of resonances in model calculations

This section attempts to bring some order to the big variety of resonances on deep diffraction gratings. The already well studied ‘photonic band gap’ on shallow gratings is shortly reviewed and a new interpretation, that highlights the symmetry of the electromagnetic problem is given. Then, the reflectivity of deep gratings is studied. The

properties of deep, symmetric gratings are re-interpreted with special emphasis on their symmetry. This will allow some understanding of the features that are found on slightly asymmetric gratings that have, to my knowledge, not been reported in literature. A short look at extremely asymmetric gratings will complete this overview. But first, some general remarks have to be made about the reflection geometry and a definition must be given what is meant by 'symmetry' of a grating in the further considerations.

5.2.1 Reflection geometry

The model calculations that are presented below are all referring to light that falls on the grating structure along the surface normal ($\theta = 0°$). The electrical field vector is perpendicular to the grating grooves ($\Psi = 0°$, $\varphi = 0°$). The dielectric constant of the metal is assumed to have a Drude-type behaviour (see Chapter 2.2) with a plasma frequency of $\omega_p = 1.2 \times 10^{16} s^{-1}$ and a collision time of $\tau = 7 \times 10^{-15} s$. These parameters are chosen to give dielectric constants similar to gold.

5.2.2 Symmetries in the grating profile

The profile of the gratings under investigation is modelled as a Fourier sum

$$z(x) = \sum_{i=1}^{\infty} A_i \cdot \sin\left(i \cdot \frac{360°}{\Lambda} \cdot x + \varphi_i \right) \qquad (5.1)$$

Where z and x denote the Cartesian co-ordinates of the profile, A_i are the amplitudes and φ_i the phases of the i'th harmonic. The phase of the first Fourier component is chosen to be $\varphi_1 = 0°$. Λ is the grating pitch which should be in the range of the wavelength of the electromagnetic radiation that is to be diffracted. In all the following calculations, $\Lambda = 700$ nm is assumed because the experimental results in the next chapter will be on gratings with roughly this pitch.

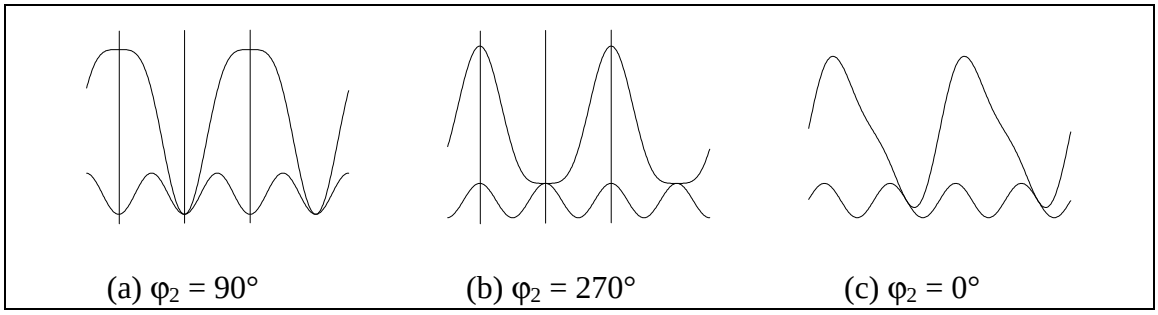

Fig. 5.3: Grating profiles formed of a fundamental of unit amplitude $A_1 = 1$ and a second harmonic with an amplitude of $A_2 = ¼$, and different choices for the phase of the second harmonic φ_2. Below the resulting profile, the 2nd harmonic is shown. For the two possible choices with mirror symmetry, the mirror planes are indicated as lines.

The investigation of a profile that is composed of only two components already yields important insights to the physical processes and symmetry properties involved in the coupling of light to surface plasmon related resonances. Fig. 5.3 shows three selected

grating profiles that can be constructed by choosing different φ_2. The ratio of the first two amplitudes, A_1/A_2 is chosen to be 4. It is important to note that there are only 2 possible choices for φ_2 that lead to a profile with mirror symmetry with respect to the mirror planes that are indicated in the graph, namely $\varphi_2 = 90°$ which leads to a 'broad peak profile' and $\varphi_2 = 270°$ describing a 'broad trough profile'.

With all other choices for φ_2, asymmetric profiles are obtained as, for example in Fig. 5.3 (c), where $\varphi_2 = 0°$. Such asymmetric gratings are called 'blazed gratings' (e. g. [Tam77]) . The higher Fourier components can be treated in a similar way. There are only two choices for the phase of the higher harmonic components that preserve the mirror symmetry.

There are two reasons why this mirror symmetry is important. Firstly, in many cases, there is no asymmetry in the grating preparation process so that 90°/270° are the only possible values φ_2 may take. Secondly, the symmetry of the profile has a strong influence on the resonances that are supported by the grating, as will be shown in the next section.

5.2.3 Shallow gratings

The resonances at the 'photonic band gap' on shallow[4] gratings at normal incidence have been intensely investigated [Kit95b], [Fis95], [Bar95]. For a comprehensive and detailed treatment of the subject the reader is referred to the excellent review article by Barnes et. al. [Bar96]. Here, only the aspects that are essential for the following are presented.

When the coupling condition for the surface plasmon is fulfilled at normal incidence, this is the case simultaneously for the 1^{st} and -1^{st} order. Furthermore, the second harmonic component of the grating profile provides the momentum that is required for coupling between these two energetically degenerate states. As a consequence, they split into a high energy and a low energy coupled state.

In Fig. 5.4, reflectivities for different grating shapes are shown. The profiles are the ones that were already shown in Fig. 5.3: either the fundamental Fourier component only, (pure sine function) or the fundamental and a second harmonic.

In the absence of a second harmonic component ($A_2 = 0$ nm), the surface plasmon position is exactly where it is expected from the momentum-matching approach (λ = 720 nm). For such a grating, there is an unperturbed crossing between the surface plasmons coupled in $+1^{st}$ and -1^{st} order. For the asymmetric grating ($A_2 = 5$ nm, $\varphi_2 = 0$), two resonances are clearly seen, one is shifted to smaller wavelengths relative to the original resonance and has become narrower, the other one has shifted to longer wavelengths and has become broader. Since for optical resonances, broad features

[4] The total vertical peak-to-trough distance is much smaller than Λ.

correspond to a short propagation (or rather coherence-) length, the terms ‘Long range surface plasmon’ (LRSP) for the narrow and ‘Short range surface plasmon’ (SRSP) for the broad resonance were chosen for this work[5]. From this observation, the conclusion can be drawn that the second harmonic component of the grating profile plays an important role in the formation of coupled resonances.

The two symmetric gratings support only one resonance each. The resonance wavelength on the ‘broad peak’ profile (A_2 = 5 nm, φ_2 = 90°) is identical to the SRSP whereas the resonance wavelength on the ‘broad trough’ profile (A_2 = 5 nm, φ_2 = 270°) is the one of the LRSP.

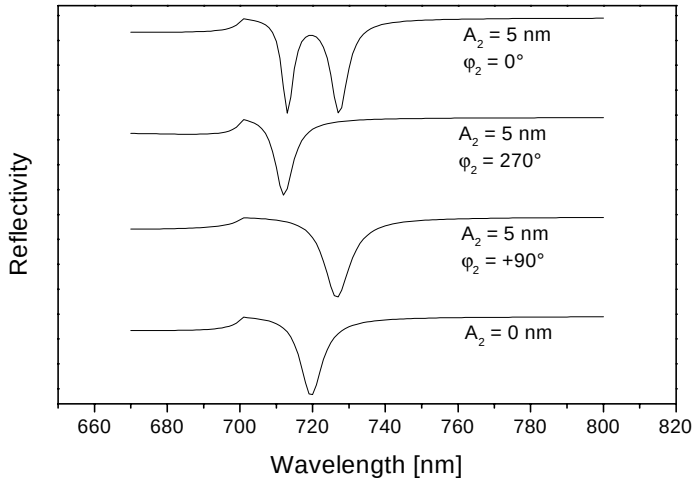

Fig. 5.4: Reflectivity for different wavelengths for a grating with a pitch of Λ = 700 nm and a profile with a first Fourier component A_1 = 20 nm and A_2 as indicated.

For the deeper understanding of the nature of these surface resonances, it is helpful to analyse their electromagnetic field distribution. Fig. 5.5 shows the magnetic field distributions for the one coupled resonance each which is observed on a purely sinusoidal, on a ‘broad peak’ and on a ‘broad valley’ grating. For the blazed grating, field distributions corresponding to the two resonances that are visible in Fig. 5.5 are shown.

For geometrical reasons, only the y-component of the magnetic field (The one parallel to the grating grooves) does not vanish, therefore the magnetic field can be represented as a (complex) scalar function. In all field distributions, the modulus of this function is plotted.

[5] The same terms are used in the case of surface plasmon coupling between two identical surfaces of a very thin metal film. In this case, too, there are two coupled resonances formed with different widths [Sar76].

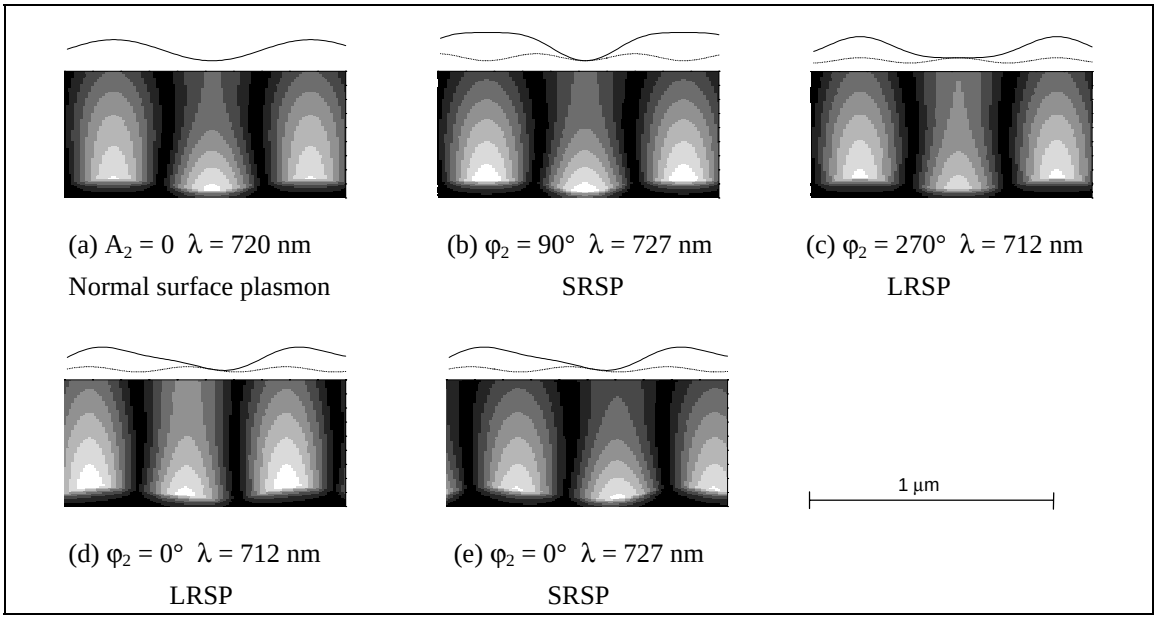

Fig. 5.5: Modulus of the magnetic field for grating profiles as introduced in Fig. 5.3. The phase of the second harmonic and the wavelength of the incident light are indicated below the pictures. White corresponds to the maximum value, black to 0. Above the pictures, the surface profile and the second harmonic are sketched with an exaggerated amplitude. The scale corresponds to the field distributions.

Strong modulation of the magnetic field along the interface is observed with two intensity maxima per fundamental oscillation of the grating profile. The positions of these maxima depend on the surface profile. For the pure sine (a), the 'broad peak' case (b) and the 'broad valley' case (c) they are located in the valleys and on the tops of the fundamental component. Nodes are observed in the slopes of the surface profile. The two resonances on the blazed gratings have similar field distributions but the field maxima are shifted by roughly 1/8 of the fundamental. The LRSP is characterised by a to the left (d) whereas the SRSP is shifted to the right (e).

In the next step, two questions will be addressed: what is responsible for the shift in resonance wavelength of the coupled resonances and why are they partly missing for symmetric gratings?

5.2.3.1 The role of the second harmonic of the grating profile

It has been already mentioned that the second component of the Fourier representation of the grating profile is responsible for the mutual coupling between the two 'free' plasmons and the formation of the band gap. It turns out that the direction of the shift in wavelength of a coupled resonance depends on the position of the magnetic field maxima relative to the second harmonic of the grating profile. The SRSP has its magnetic field maxima in the minima of the second harmonic whereas the LRSP's magnetic field is concentrated on the maxima of the second harmonic. For the detailed discussion of the underlying physics, the reader is referred to the paper of Barnes et al. [Bar96]. Now, by comparison of the magnetic field distributions (Fig. 5.5) with the relative position of first and second harmonic (as drawn in Fig. 5.3), the shifts in

wavelength that are observed in Fig. 5.4 can be understood. Magnetic fields in the maxima of the second harmonic lead to a LRSP at $\lambda = 712$ nm. A SRSP ($\lambda = 727$ nm) is characterised by magnetic fields in the minima of the second harmonic. Without a second harmonic, there is no shift.

5.2.3.2 'Selection rules'

Another important question is why for symmetric gratings there is always one of the resonances missing. In the paper of Barnes et. al. this is explained by considering the component of the incident electrical field normal to the metal surface which is needed to produce a surface charge[6]. Coupling is possible only to the surface modes with a charge distribution that is in phase with the one produced by a non-vanishing component of the exciting electrical field normal to the metal-dielectric interface. An analysis of the charge distribution that would be needed to set up resonances with maxima in the peaks or troughs of the second harmonic of the grating profile, it turns out that on symmetric gratings there is always one in phase with the exciting charge distribution while the other one is phase shifted by 90°. As a consequence, the one is maximally coupled and the other one is not observed. With the same reasoning, it can be explained why there is coupling to both resonances for the blazed grating: here, we twice deal with a phase shift of exciting charge distribution and resonance intrinsic charge distribution of 45°.

I wish to present a slightly different approach to the problem, which seems to be more intuitive. The underlying physics is, of course, the same. It is based on considerations of the symmetry of the grating and the exciting field. We start again by examining the response of the two symmetric gratings in the example given above. The 'missing' resonances would have nodes of the magnetic field intensity on the peaks and in the troughs of the fundamental in order to have the correct position relative to the second harmonic of the grating profile. Why are they not coupled to?

In order to answer this question, we need to recall that the mathematical problem of reflection of a monochromatic electromagnetic wave on any dielectric configuration can be either described by the electrical or magnetic field. Both give the full description of the solution and if one is given, the other one is easily calculated by using Maxwell's equations. In the case that is considered here, the easier choice is the magnetic field since it has only one non-vanishing component, H_y.

Now, consider the symmetry of the entire system. The geometry is specified by the propagation direction and polarisation of the incident magnetic field and the surface profile. Obviously, all the physical quantities and therefore the full problem have mirror symmetry with respect to the mirror planes as indicated in Fig. 5.3. An allowed solution must exhibit the same symmetry. In Fig. 5.5, the modulus of the magnetic field of the

[6] Please note that the assumption that only the normal component is responsible for the excitation should be doubted, compare chapter 7. Nevertheless, the analysis of Barnes et al. is still valid with minor adaptations.

allowed solution is plotted, and the predicted symmetry is observed in this example. But, since the time dependent magnetic field is given by a complex function, we have to consider the phase as well. When a node in the magnetic field distribution is observed, there is always a phase jump by 180° associated with it (because the first derivative of the magnetic field must be continuos).

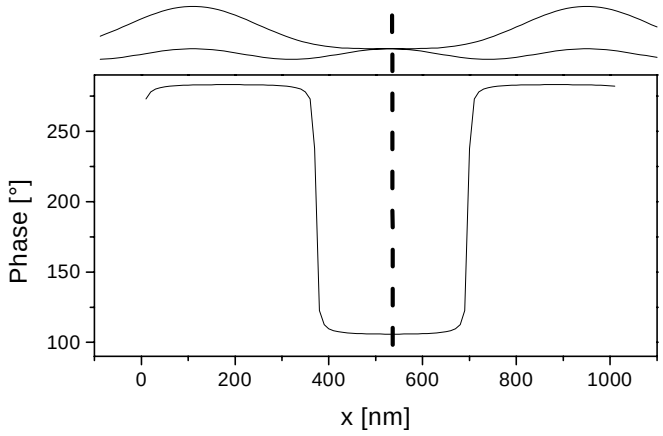

Fig. 5.6: Phase of the magnetic field 200 nm above the surface for the resonance on the 'broad valley' profile (see Fig. 5.5 c). Above, the surface profile is sketched together with its second harmonic component, the vertical line indicates the common mirror plane of surface profile and field distribution.

This is illustrated in Fig. 5.6 for a 'broad valley' mirror symmetric grating. Comparison with (Fig. 5.5, c) shows that indeed a phase jump of 180° is observed at each node of the magnetic field. Furthermore, the right symmetry of the phase (Fig. 5.6) and the modulus value of the magnetic field is seen for this example.

Now, it is obvious, why there is no SRSP for the 'broad valley' grating. Such a mode, having its magnetic field maxima in the troughs of the 2nd harmonic of the grating profile would have a node right in the mirror plane. The associated phase jump would break the mirror symmetry and a solution with odd symmetry (symmetric modulus but reversed sign upon reflection) would be obtained instead.

It is instructive to do the same analysis for the electrical field. Here, things are a little more complicated because there are two components of the electrical field that have to be considered, z and x direction. The absolute values of these field components are plotted in Fig. 5.7. For each component there is again a phase jump of 180° at each nodal plane for the same reasons as discussed above.

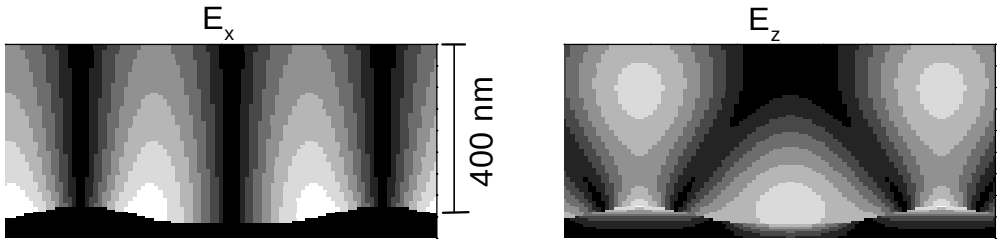

Fig. 5.7: Electrical field distribution for LRSP of the 'broad valley' profile. The absolute value of the x and z component are plotted as grey values. White indicates the maximum value, black 0.

The calculated x component has odd symmetry with respect to the mirror plane. This behaviour is expected, because the incident electrical field is polarised in x direction. Upon inversion on the mirror plane, this field reverses its sign. Therefore, the initial problem has odd symmetry.

The calculated z component has even symmetry with respect to the mirror plane. This, again, reflects the symmetry of the system: like a vector in y-direction (as the magnetic field in the example considered above), a vector in z-direction keeps its orientation upon reflection.

As soon as the grating looses mirror symmetry, there are no restrictions to the symmetry of the electromagnetic field distributions. That is why both resonances are coupled to incident light on a blazed grating.

5.2.4 Deep gratings with mirror symmetry

Now, after having got some insight into the coupled resonances in the relatively simple case of a shallow grating, the focus now is on the additional effects that come into play when the grating amplitude is increased. It is most instructive to vary both the wavelength of the incident light and the grating amplitude continuously and investigate the dispersion of the resonances which can be observed as areas of reduced reflectivity in the plane which is spanned by these two parameters. The grating amplitude is always varied by applying a linear scaling factor sc to all Fourier components of one grating profile, thus keeping the ratios between the individual amplitudes fixed.

$$z_{scaled}(x) = sc \cdot z(x) = sc \cdot \sum_{i=1}^{\infty} A_i \cdot \sin\left(i \cdot \frac{360°}{\Lambda} \cdot x + \varphi_i \right) \qquad (5.2)$$

Since sc is not a very intuitive quantity, the resulting fundamental amplitude sc. A_1 is used as a measure of the total grating amplitude. In Fig. 5.8, the reflectivity of a deep 'broad peak' grating is plotted as grey values when the wavelength of the incident light and the grating amplitude are varied.

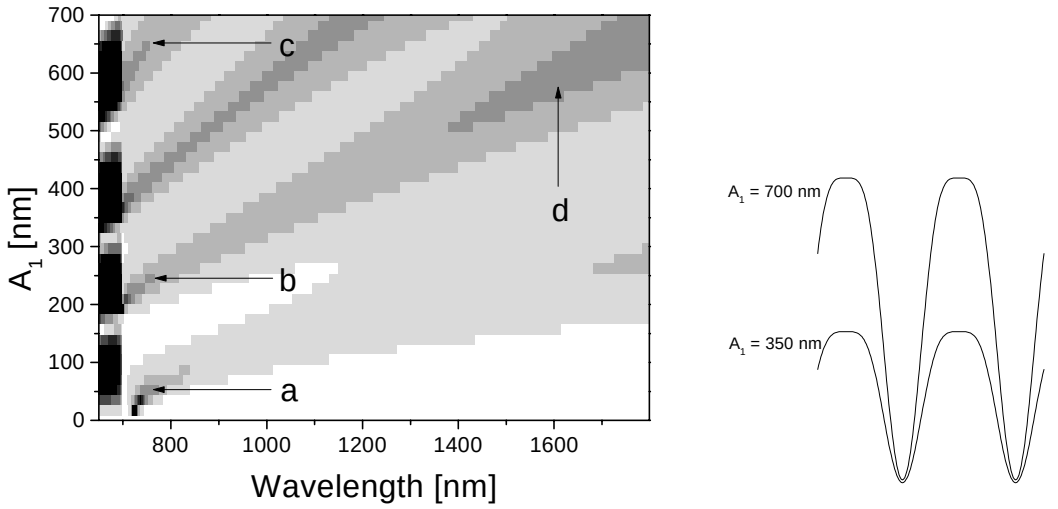

Fig. 5.8: Calculated reflectivity map of a grating (Λ = 700 nm) of the form as shown on the right as a function of grating amplitude and wavelength of the incident light. The grey values indicate different reflectivities from 0.5 (black) to 1 (white). The arrows indicate where field distributions will be calculated. The maximum grating profile has the Fourier components A_1 = 700 nm, A_2 = 175 nm, φ_2 = 90°.

The pseudocritical edge at λ = 700 nm where the first diffracted orders become evanescent is clearly seen as a sharp rise in intensity. For longer wavelengths, the grating is of zero order, that means that all diffracted orders are evanescent. In this region, four extended dark stripes, indicating low reflectivity, are observed. These resonances move to the infrared for increasing grating amplitudes.

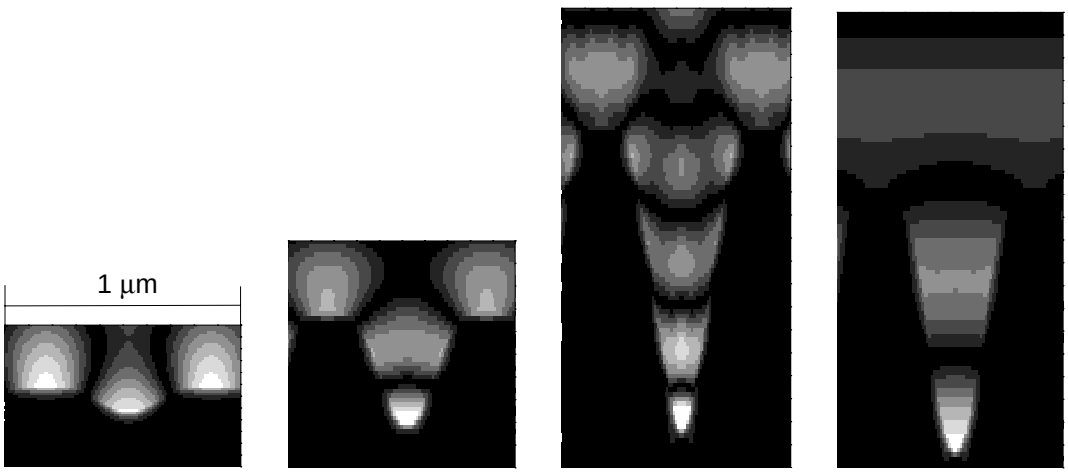

(a) λ = 750 nm A_1 = 52.5 nm (b) λ = 757 nm A_1 = 245 nm (c) λ = 750 nm A_1 = 648 nm (d) λ = 1595 nm A_1 = 578 nm

Fig. 5.9: Spatial distribution of the magnetic field strength as grey values (white indicating high magnetic field strength) for some selected resonances in the reflectivity map (Fig. 5.8). The scaling bar applies to all images.

An analysis of the magnetic field distribution across the grating structure in these resonances, shown in Fig. 5.9, gives some insight into the nature of these features.

The distributions (a, b, c) are taken at about the same wavelength for increasing amplitude of the grating as indicated in Fig. 5.8. They correspond to the first, second and forth 'branch'. It can be seen that each branch has a unique topology of the magnetic field distribution, with a characteristic number of nodal planes and maxima. For each 'step upwards', one nodal plane, spanning the grating groove, is added. Fig. 5.9 (d) lies on the same branch as (b) which is reflected in the same number of maxima and nodes of the magnetic field inside the groove. In the following, these higher resonances will be called ME_i ('magnetic even') where the integer i denotes the number of separated field maxima inside the grating groove.

If we recall the symmetry constraints to an allowed solution of the electromagnetic boundary problem, it is seen that these 'ladders' have the required even symmetry. It should be noted that they are not the only possible solutions. Lopez-Rios [Lop98] has investigated a shallow grating with very widely separated grooves where additional nodes show up on top of the grating peaks. Additionally, closed loops of nodal planes inside the grating grooves cannot be excluded by symmetry considerations.

It should be mentioned that predictions for this type of resonances on deep diffraction grating can be found in literature. The first of these resonances is identical to the SRSP in the limit of very small grating amplitudes. For higher amplitudes, the field gets more concentrated inside the groove at the expense of the field strength on the top of the grating. This resonance has been described by various authors [Gar96], [Lak81].

The whole family of resonances that is found on deeper gratings was described by Watts et al. [Wat97] and Sobnack at al. [Sob98], the latter giving a good intuitive interpretation. The electromagnetic surface modes propagate along the grating tops as surface plasmons while they have to be described as waveguide modes inside the groove. The total phase that is picked up by such a mode between two equivalent points on the grating must equal a multiple integer of 2π. An approximate analytical calculation based on this model leads to a good agreement compared to the rigorous modelling. Maradudin et al. [Mar97] considered a single groove in an otherwise plane metal surface and found similar resonances.

Currently there is much interest in the transmission through slits in metal layers which are of the order of the wavelength of light or smaller as recent theoretical papers show [Ast00], [Por99]. A strong enhancement of the transmission due to excitation of localised resonances inside the grooves is predicted. Experimental results on 2-dimensional arrays of holes are presented by Ebbesen [Ebb98], in this work, no localised resonances inside the holes were found because of the small thickness of the metal film.

A purely sinusoidal grating shows almost no resonance features for increasing depths (not shown). The conclusion must be drawn that the reflectivity of a deep grating is very sensitive to its shape.

5.2.5 Deep, asymmetric gratings

From the investigations on shallow gratings it can be already assumed that a broken symmetry will make the optical response of deep gratings richer. Some theoretical investigations on this problem are presented in a paper by Preist et al. [Pre97]. Wanstall et al. [Wan98] concentrate on highly overhanging gratings and find a family of resonances similar to the ladder of the ME_i resonances that was discussed above. Still, there is no investigation on slightly blazed, deep gratings in the literature. For this reason, the additional features that are introduced by the asymmetry of the grating and their evolution when the asymmetry is increased are presented in this subsection.

5.2.6 A 'new' resonance

The asymmetry is introduced to the grating shape by applying the oblique transformation which is given by the obliquity angle θ_{ob} (See chapter 2) to the points that describe the grating profile

Already a very small blaze (θ_{ob} = 87°) has got a drastic effect on the resonance structure as it can be seen in Fig. 5.10.

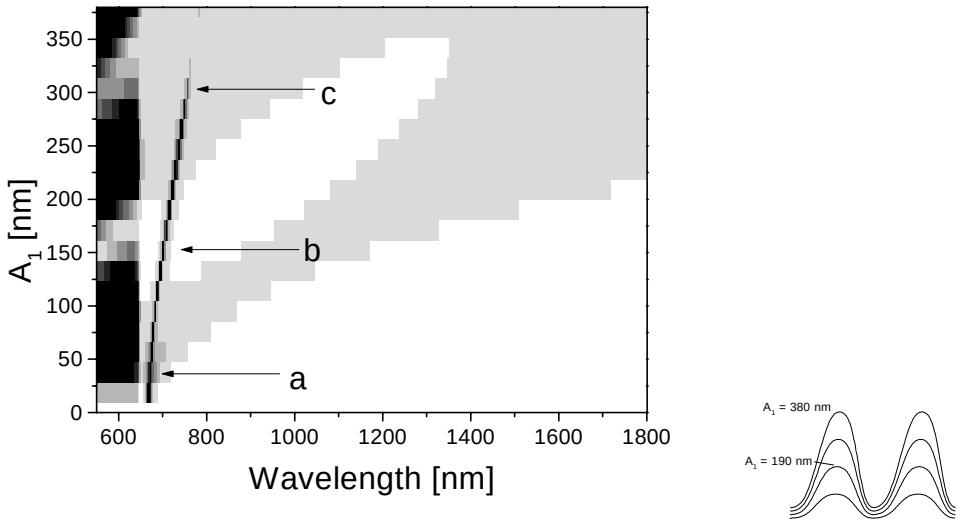

Fig. 5.10: Calculated reflectivity map of a grating of the form as shown on the right as a function of grating amplitude and wavelength of the incident light. The grey values indicate different reflectivities from 0.5 (black) to 1 (white). The arrows indicate for which parameters field distributions will be calculated. The maximum grating profile has the Fourier components A_1 = 380 nm, A_2 = 10.6 nm, φ_2 = 26.3°, A_3 = 23.4 nm, φ_3 = 36.3°, the oblique angle equals θ_{ob} = 87°.

The first two ME_i resonances are visible in this plot only very weakly due to the small deviation of the profile from the pure sine. Additionally, a very deep and narrow resonance appears which had not been observed for mirror symmetric gratings. In the limit of a shallow grating this new feature is identical to the LRSP. A view on the magnetic field distributions (Fig. 5.11) reveals why this resonance appears only on blazed gratings. The magnetic field distributions show almost odd symmetry which is only possible because the mirror symmetry of the grating is slightly broken.

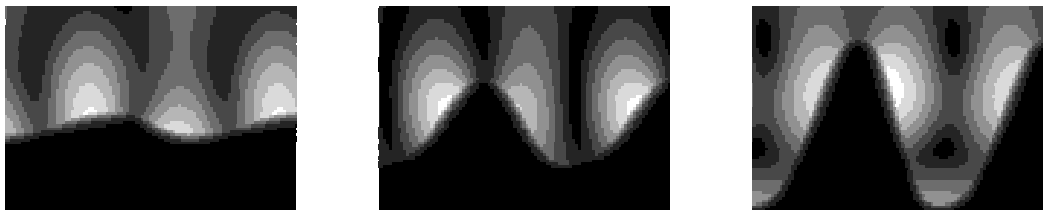

(a) A_1 = 38 nm, λ = 673 nm (b) A_1 = 152 nm, λ = 703 nm (c) A_1 = 304 nm, λ = 757 nm

Fig. 5.11: Spatial distribution of the magnetic field strength as grey values (white indicating high magnetic field strength) for some selected resonances in the reflectivity map (Fig. 5.10). The images are drawn to scale. The scale has been suppressed for better readability, each section is 1000 nm wide.

This finding allows an extension of the interpretation of the deep grating as array of small waveguides as it was shortly reviewed above. It seems that these 'waveguides' are able to support two families of surface plasmon-related 'lamellar' resonances. The one family (ME_i) is characterised by a magnetic field with even and an electrical field with odd symmetry. On shallow 'broad peak' gratings, this family is represented by the SRSP. The other family has an magnetic field with odd and an electric field with even symmetry. It is not coupled to free electromagnetic radiation normally incident on a mirror symmetric grating. Breaking of the symmetry of the grating profile allows coupling and in consequence its observation.

An alternative way to excite modes with a magnetic field distribution with odd symmetry is described by Watts et al. [Wat97]. They report the observation of a resonance that is coupled with TM light in a geometry where the plane of incidence is parallel to the grating grooves (Ψ = 90°) and the polar angle (θ) is different from 0°. There, additionally the existence of higher orders of this family of resonances for very deep gratings has been shown in a model calculation. This experimental geometry preserves the symmetry of the grating but offers an exciting magnetic field with odd symmetry. The electrical field has even symmetry now. In some sense, the roles of electrical and magnetic field are exchanged compared to the ME_i resonances. From these considerations, these resonances are identified with the ones that are observed on slightly asymmetric gratings. In the further investigations these resonances will be called 'magnetic odd' MO_i.

It should be noted that due to the slightly broken symmetry of the grating profile, the even or odd symmetry of these modes is not exact. But if the grating asymmetry is not

too big, these labels are still helpful to understand the observed resonance patterns and are used in this and the following section.

5.2.6.1 Interaction between the two families of resonances

When the appropriate grating profile is chosen, the two families of resonances with even and odd symmetry may appear in significant strength simultaneously. This makes the reflectivity map of such a grating relatively complex. Fig. 5.12 shows calculated reflectivities for a 'broad peak' profile which is tilted by an obliquity angle of $\theta_{ob} = 70°$. The first 3 resonances with magnetic field with even symmetry (ME_1, ME_2, ME_3) are seen as broad areas of slightly reduced reflectivity which move quickly to the infrared for increasing grating amplitude.

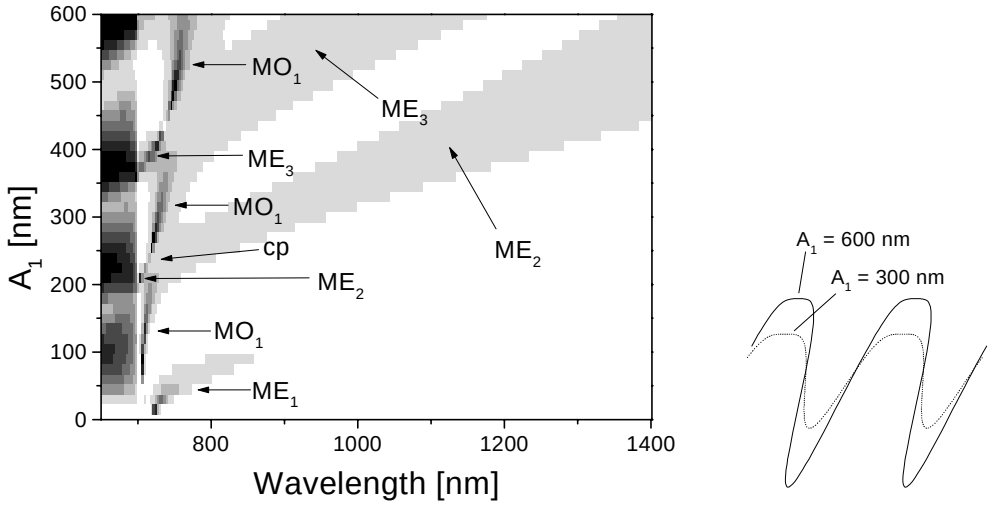

Fig. 5.12: Calculated reflectivity map of a grating of the form as shown on the right as a function of grating amplitude and wavelength of the incident light. The grey values indicate different reflectivities from 0 (black) to 1 (white). The maximum grating profile has the Fourier components $A_1 = 600$ nm, $A_2 = 150$ nm, $\varphi_2 = 90°$. The oblique angle is $\theta_{ob} = 70°$. The assignments on the arrows are explained in the text.

Close to the pseudocritical edge, a rich structure is seen that can be interpreted as follows:

The areas of low reflectivity marked with an 'MO_1' correspond to the first resonance with a magnetic field of odd symmetry. The minima right at the pseudocritical edge belong to the resonances with even-symmetric magnetic field again. That means: A crossing of the MO_1-resonance with the ME_2 and ME_3- resonances leads to this reflectivity behaviour.

Of course, one must check that the assignment given above reflects the real physics. The magnetic field distributions of the MO_1 resonance and the ME_2 resonance are shown in Fig. 5.13 right before and after crossing each other. The 'crossing point' is indicated in Fig. 5.12 as 'cp'.

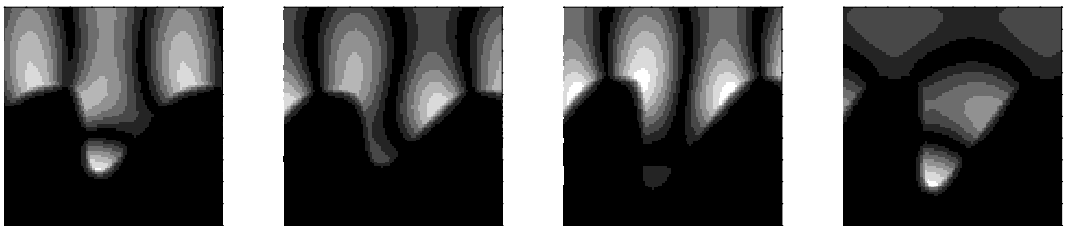

(a) ME_2	(b) MO_1	(c) MO_1	(d) ME_2
λ = 704 nm	λ = 717 nm	λ = 721 nm	λ = 854 nm
A_0 = 180 nm	A_0 = 210 nm	A_0 = 270 nm	A_0 = 270 nm

Fig. 5.13: Magnetic field distributions for the grating profile as specified in Fig. 5.12 for the amplitudes of the first harmonic and the wavelengths of the incident light as indicated below the individual pictures. Black indicates vanishing, white maximum field strength. The scales have been omitted for better readability. Each graph represents a 1000 nm wide section of the grating.

It can be seen that the symmetry of the field distributions is highly distorted. Nonetheless the topology of the nodal planes still reflects the original symmetry: The plots (a) and (d) correspond to the ME_2 resonance left and right from the crossing point that is indicated in Fig. 5.12. The characteristic nodal plane across the grating groove is visible in both cases. In contrast, (b) and (c) which correspond to the MO_1 resonance below and above the crossing point clearly show a nodal plane which is lying on the 'symmetry axis' of the grating which is typical for odd symmetry. One further observation is made in the field distribution (c): on the extreme bottom of the profile, a weak portion of magnetic field has built up with even symmetry. Upon each subsequent crossing, a new horizontal nodal plane will be added, which leads to the formation of resonances that may be described as even type at the bottom and odd type near the peaks of the profile.

Finally a strongly overhanging grating is investigated. The reflectivity of such a structure is shown in Fig. 5.14. The resonances have become deeper and narrower. No crossing points with destructive interference of the resonances belonging to different symmetries are now observed. This shows that on such a highly asymmetric structure, the classification that was given above is not applicable. For a detailed analysis of the magnetic field distributions, the reader is referred to the work of Wanstall et al. [Wan98].

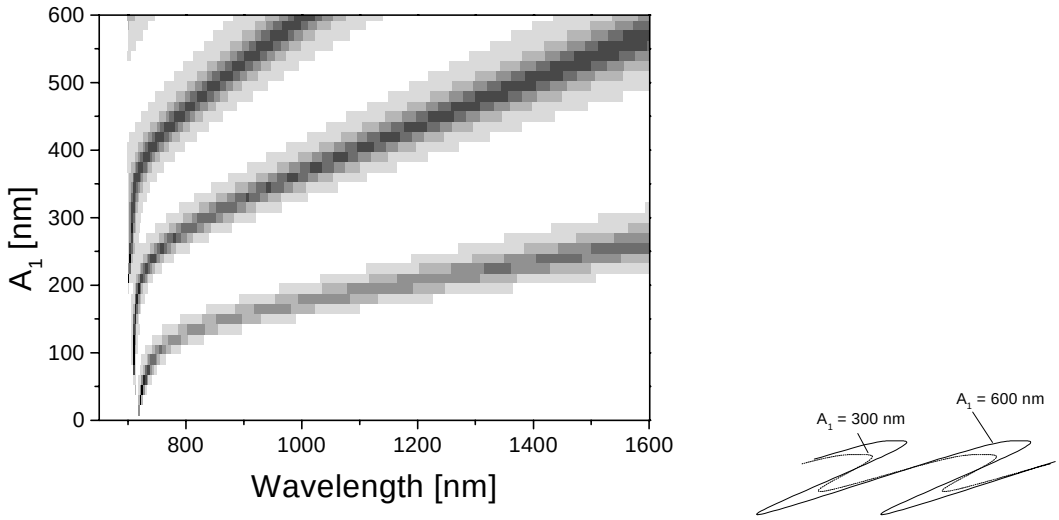

Fig. 5.14: Calculated reflectivity map of a grating of the form as shown on the right as a function of grating amplitude and wavelength of the incident light. The grey values indicate different reflectivities from 0 (black) to 1 (white). The maximum grating profile has the Fourier components $A_1 = 600$ nm, $A_2 = 150$ nm, $\varphi_2 = 90°$. The obliquity angle is $\theta_{ob} = 20°$.

5.2.7 Conclusion

The resonances that lead to absorption of light falling vertically on metallic gratings were investigated in model calculations for a Drude-type metal. It was found that, on symmetric gratings, two classes of resonances may exist with magnetic field distributions that exhibit either even or odd symmetry. At normal incidence, only the even ones couple to light.

By introduction of a slight asymmetry to the grating profile, the resonances can still be roughly classified like in symmetric gratings. Now, both types are observed in the same experimental geometry and mutual interaction takes place. In the resonance pattern of highly asymmetric gratings the two classes are completely mixed.

An alternative way to couple to the resonances with odd symmetry of the magnetic field consists in choosing an appropriate reflection geometry which differs from normal incidence. This observation was only shortly mentioned but will be explored to some more detail later in this chapter.

5.3 Experimental results

In this section, reflectivity measurements on gratings with varying blaze and amplitude are discussed and compared to model calculations. The depth and degree of asymmetry was tuned by varying the geometry and exposure time in the etching process as is described in chapter 3.

First (5.3.1), wavelength-dependent reflectivity data are presented that were taken at (almost) normal incidence on asymmetric gratings with the set-up that is described in chapter 3. For four different degrees of asymmetry, the measurements are compared to completely independently obtained theoretical calculations. Additionally, measurements are shown for varying amplitude for these blazed gratings. In the following subsection (5.3.2), the theoretical prediction of stationarity of the red-shifted ME resonances is proved experimentally. Another subsection deals with measurements on a symmetric grating where the experimental geometry is varied (5.3.3). Finally, (5.3.4) an experimental observation that cannot be described with the idealised model of a perfect grating is presented and an explanation is proposed.

5.3.1 Blazed gratings at 'normal' incidence

In this section, gratings, etched under different angles θ_{etch} = (10°, 20°, 30°, 40°), are investigated. See chapter 3 for details of the sample preparation and the optical measurements. The experimental geometry is chosen to have the same symmetry as normal incidence (polar angle θ = 4°, azimuthal angle Ψ = 90°) In this case, TE-polarisation has an electrical field perpendicular to the grating grooves. It is essentially the same as TM polarisation in the classical mount: The polarisation where coupling to the surface plasmon resonance is possible. For each etching angle, the following measurements and model calculations of the wavelength-dependent reflectivity are discussed:

One sample is measured once and the surface profile obtained by electron microscopy. For this sample, the measured reflectivities are compared to theoretical predictions that were obtained on the basis of the grating profile as determined from the electron microscopy images. For these model calculations, the dielectric function of the gold was modelled as a Drude metal with plasma frequency $\omega_p = 1.22 \times 10^{16}\ s^{-1}$ and a collision time $\tau = 7 \times 10^{-15}$ s. (compare chapter 2).

The effect of the variation of the grating amplitude on the surface resonances is studied by recording the reflectivity spectrum after subsequent etching steps of another sample. It is intuitively clear that etching a pure gold grating will lead to a decreasing grating amplitude. The precise grating shape after each individual step could not be measured because the samples have to be broken to do so. For this reason, the profile that was obtained from the first sample was used for model calculations of this experiment, too. These experimental data is compared to numerical data where a scaling factor between 0

and 2 is applied to the surface profile that allows observation of the amplitude-dependent dispersion of these resonances. It is neither known how much the grating amplitude is decreasing by etching into the pure gold, nor if the originally determined grating profile is still applicable for strongly etched gratings. For this reason, a quantitative modelling of these experiments is not possible.

The interpretation of the data is delayed to the end of this subsection where a comparison of all experimental results is possible.

5.3.1.1 Etched at 10°

The measured and calculated reflectivity of a grating etched under 10° is shown in Fig. 5.15 and Fig. 5.16 for illumination with TE and TM polarised light, respectively. Between λ = 1000 and 1100 nm the data sets taken with the two detectors overlap and form some 'kinks' which should not be regarded further. It is clearly seen that although there is quantitative agreement between measurement and modelling, there are some discrepancies with respect to the observed resonances.

The pseudocritical edge is observed at 650 nm in good agreement of theory and experiment as expected. For short wavelengths, the measured reflectivity is much too low while further in the infrared the measured values are approaching the theoretical prediction for both polarisations.

For illumination with TE light, two resonances can be observed.

A very narrow and deep minimum appears around 700 nm which is predicted slightly too far in the infrared. This feature is assigned to the lowest resonance with magnetic field with odd symmetry (MO_1)[7]. The measured minimum appears broader and shallower than in the model calculation what is due to the finite wavelength resolution of the set-up and the inhomogenity of the real grating.

The other resonance is much broader and further in the infrared. Again, there is a discrepancy between theory and experiment with respect to its precise position. Additionally, this resonance appears deeper in the measurement than in the model calculation. It is assigned to the strongly red-shifted ME_1 resonance.

The measurement with TM polarisation doesn't show any resonance minimum in agreement with theory. This is the case for the other 3 degrees of blazing that will be discussed later, too, for this reason these measurements with TM polarisation will not be shown.

[7] In Fig. 5.10, exactly the same profile as here was used in a model calculation to introduce this kind of resonance.

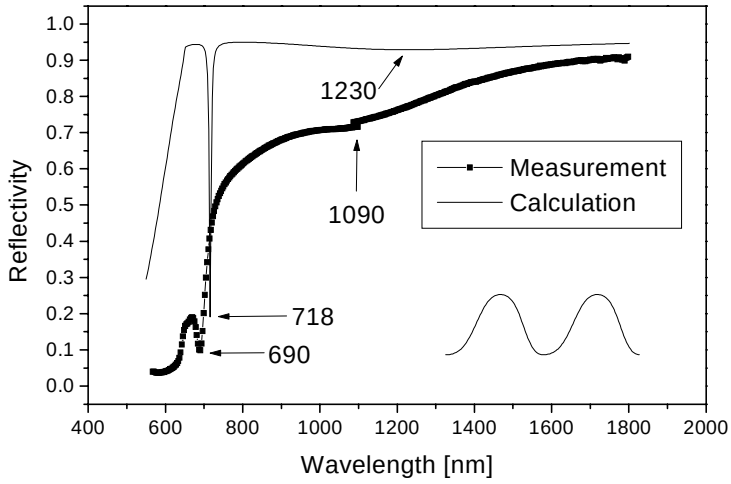

Fig. 5.15: Measured (line with dots) and modelled (straight line) wavelength-dependent reflectivity of the sample etched at 10° for TE polarisation. The surface profile as determined from the SEM-image is shown in the graph. The arrows indicate the wavelengths of reflectivity minima that are attributed to surface resonances.

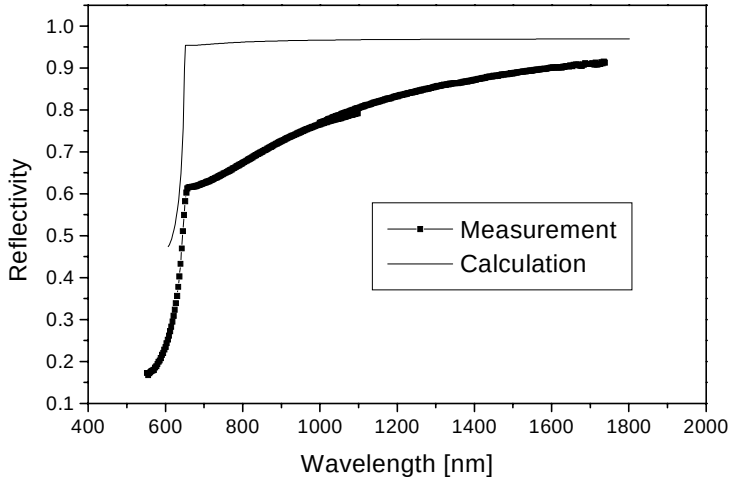

Fig. 5.16: Measured (line with dots) and modelled (straight line) wavelength-dependent reflectivity of the sample etched at 10° for TM polarisation . The model calculation is based on the same surface profile as for the TE case. (Fig. 5.15)

The measured dispersion of these two resonances as a function of the grating amplitude are presented in Fig. 5.17 and the corresponding model calculation is shown in Fig. 5.18. By comparison of the positions of the two resonances that are visible both in theory and experiment, the model calculations with scaling factors between 0.5 and 1 are seen to correspond roughly to the measured data.

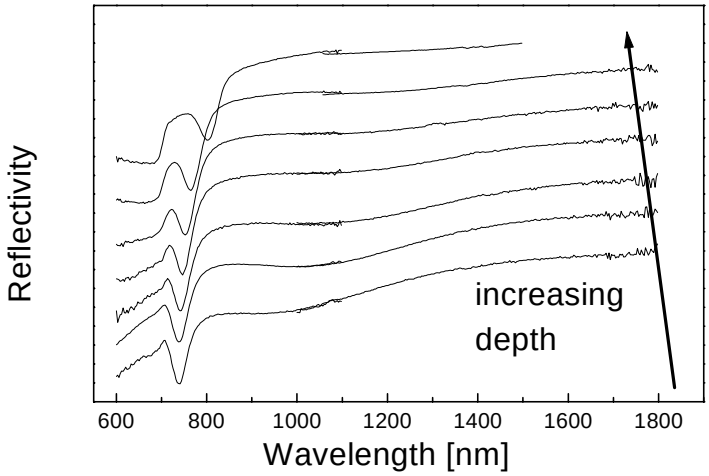

Fig. 5.17: Measured wavelength-dependent reflectivity of a gold grating etched under 10°. The deepest grating was measured first and then the amplitude was decreased by subsequent etching steps.

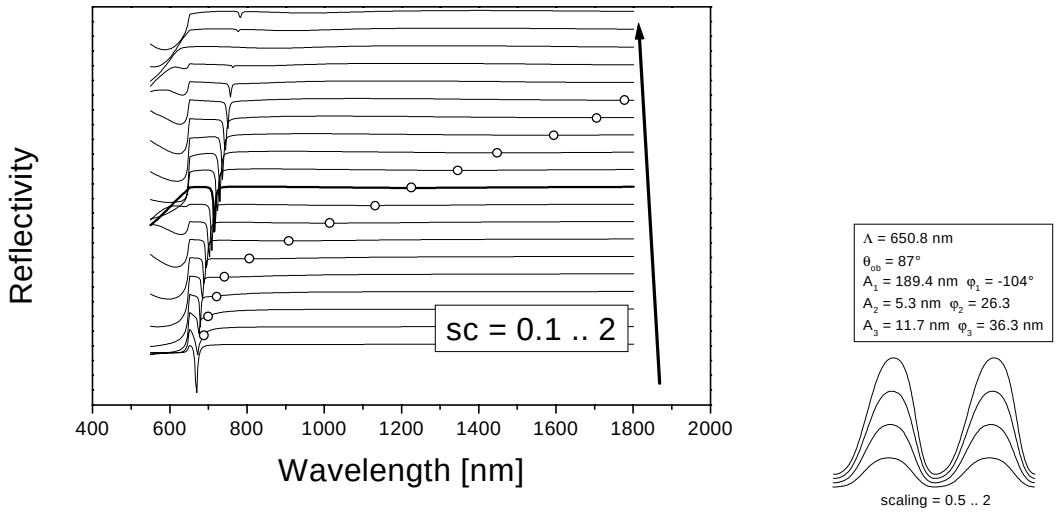

Fig. 5.18: Modelled wavelength-dependent reflectivity for the grating shape that is produced by etching under 10° with scaling factors applied to the grating profile that vary between 0.1 and 2. The parametrisation of the grating profile and sketches of the grating shape for some scaling factors are shown on the right. The position of the ME_1 is indicated by open circles. The thicker line corresponds to the grating shape as determined by electron microscopy.

With respect to the dispersion of the MO_1 resonance, the correspondence between theory and experiment is good. With increasing depth, this feature is slowly shifted into the infrared. The strength of the resonance is not significantly altered for varying amplitudes. The decreasing strength in the model calculation is observed for grating amplitudes that were significantly higher than the measured ones (sc = 1.8). They were not accessible to experimental investigations.

The influence of an increasing grating amplitude on the position and strength of the ME_1 resonance is measured as predicted by the model calculation: A fast redshift is accompanied by a significant weakening that makes the resonance difficult to see, especially in the model calculations. The absolute depth of this minimum is smaller in the calculation than in the experiment.

5.3.1.2 Etched at 20°

The measured and modelled reflectivity of a grating etched under 20° is shown in Fig. 5.19. Again, the measured reflectivity is significantly too low everywhere except at very long wavelengths. The same resonances as in the previous section can be seen, still there are only slight differences between theory and experiment.

The MO_1 resonance is again measured at a shorter wavelength than predicted. Its strength has decreased with respect to the 10°-grating which is reflected both in theory and experiment.

The position of the symmetric resonance is this time measured at a longer wavelength than predicted. Furthermore, a slight increase in strength of this resonance can be seen.

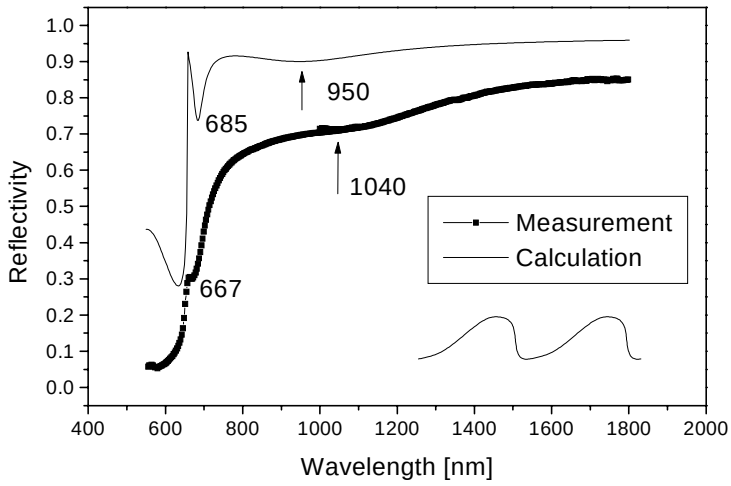

Fig. 5.19: Wavelength-dependent reflectivity of the grating etched at $\theta_{etch} = 20°$ as determined from a measurement compared to a model calculation. The surface profile as determined from the SEM-image is shown in the graph.

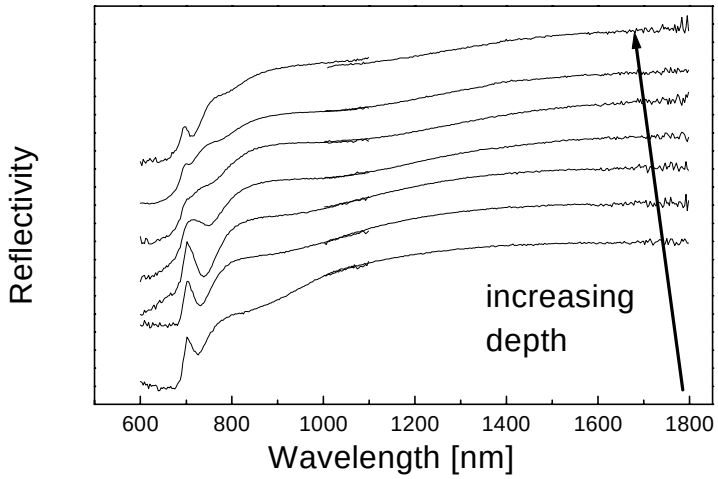

Fig. 5.20: Measured reflectivity as a function of wavelength of the incident light for a gold grating etched under $\theta_{etch} = 20°$. The deepest grating was measured first and then the amplitude was decreased by subsequent etching steps.

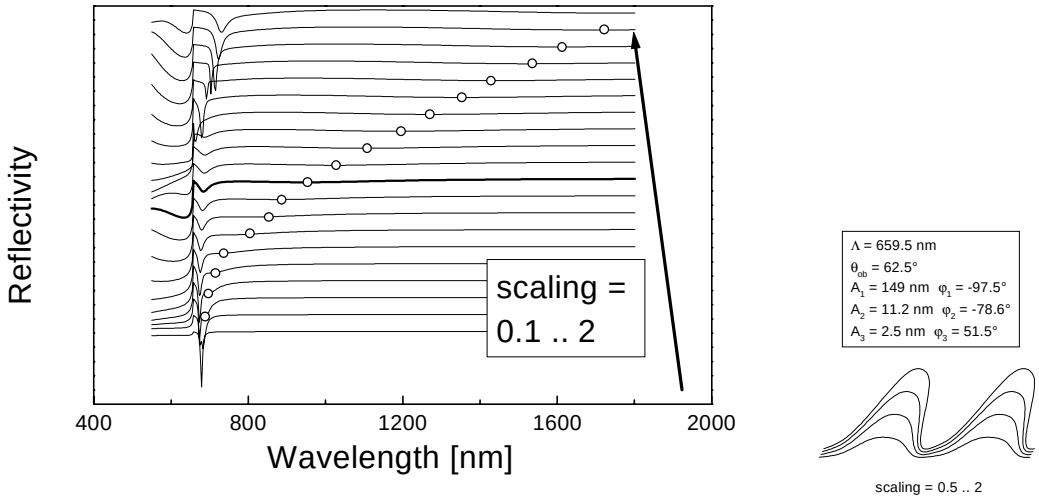

Fig. 5.21: Modelled reflectivity for $\theta_{etch} = 20°$ as a function of wavelength for different grating amplitudes. On the right, a graphical representation of the grating shapes and numerical values of the parameters are shown. The position of the very weak ME_1 resonance is indicated by open circles. The thick line corresponds a grating shape as determined by electron microscopy.

The measured dispersion as a function of the grating amplitude is presented in Fig. 5.20 and the corresponding model calculation is shown in Fig. 5.21. Good agreement between theory and experiment was found regarding the changes that are due to the increased asymmetry of the grating profile.

Little has changed with respect to the ME_1 resonance compared to the grating etched at 10° except a slight increase in strength.

The MO_1 resonance shows a peculiar behaviour in the measurement. It shifts slightly to the infrared and broadens. At the two deepest gratings, a new feature comes in from the pseudocritical edge while the MO_1 has almost completely disappeared. Exactly this behaviour is seen in the model calculation. The model calculation of the region around the pseudocritical edge is shown in an enlarged representation in Fig. 5.22.

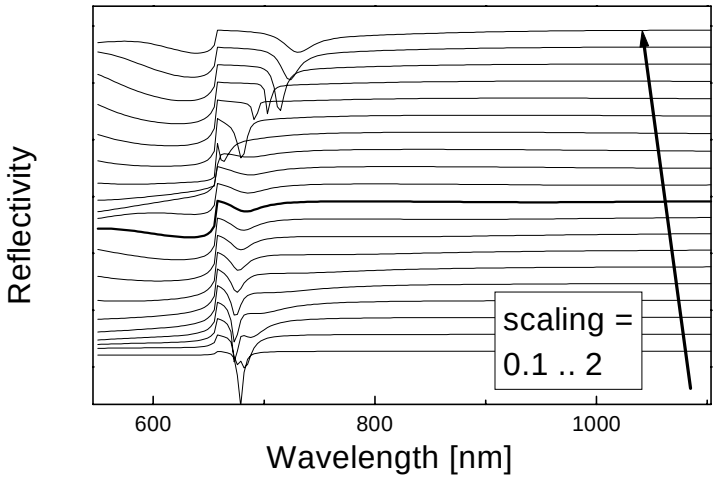

Fig. 5.22: Enlargement of Fig. 5.21

A comparison with the section 5.2.6.1 leads to the conclusion that this new minimum is due to the second resonance with a magnetic field of even symmetry, ME_2. From this, it can be concluded that the maximum grating amplitude that could be produced lies slightly below the crossing point of the MO_1 and the ME_2 resonance. Because both the measured wavelength of ME_1 and the appearance of ME_2 is expected for higher amplitudes, it can be assumed that the amplitude as it was determined from the electron micrographs is too small. The model calculations with scaling factors between 0.7 and 1.4 are tentatively assigned to the range of amplitudes that was experimentally accessible.

5.3.1.3 Etched at 30°

The measured and modelled reflectivity of a grating etched under 30° is shown in Fig. 5.23. ME_1 and MO_1 can still be seen and the effect of the increasing asymmetry is consistent in theory and experiment.

MO_1 is again observed at a shorter wavelength than predicted. It has become shallower than in the previous examples.

ME_1 is observed at a wavelength that is smaller than predicted. It has significantly gained in strength in the measurement. While the absolute strength is still significantly underestimated in the model calculations, an increase compared with the other model calculations can be observed.

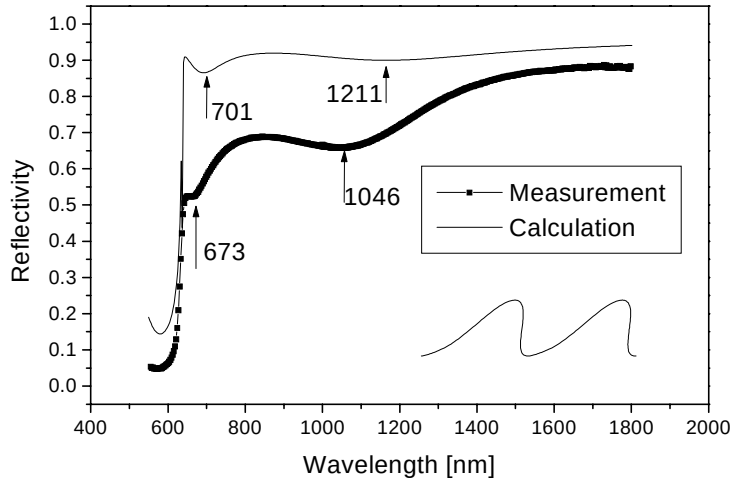

Fig. 5.23: Wavelength-dependent reflectivity of the grating etched at $\theta_{etch} = 30°$ as determined from a measurement compared to a model calculation. The surface profile as determined from the SEM-image is shown in the graph.

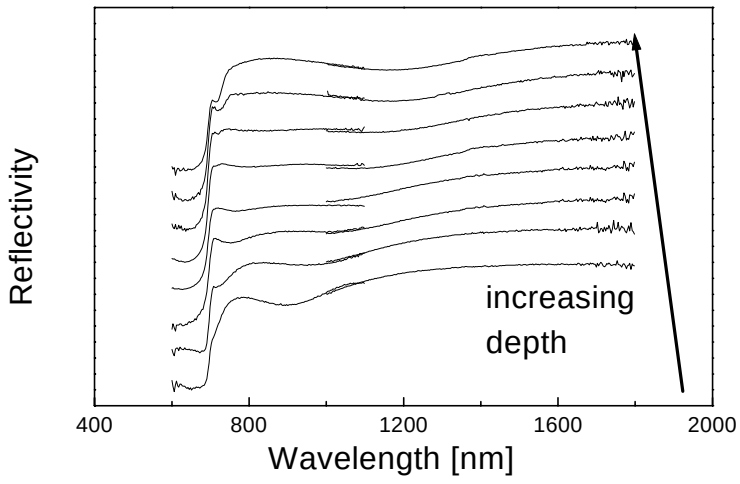

Fig. 5.24: Measured wavelength-dependent reflectivity of a gold grating etched under 30°. The deepest grating was measured first and then the amplitude was decreased by subsequent etching steps.

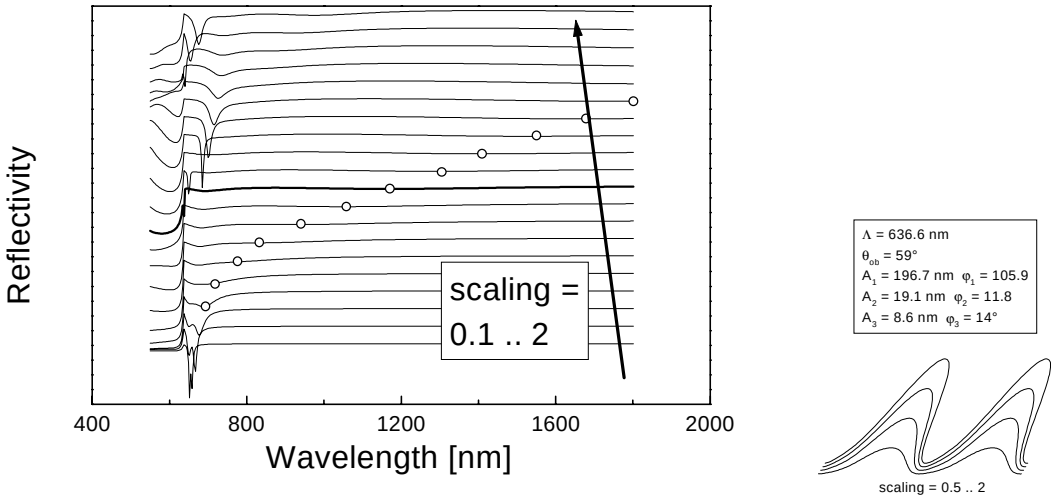

Fig. 5.25: Modelled reflectivity for $\theta_{etch} = 30°$ as a function of wavelength for different grating amplitudes. The ME_1 resonance is marked with open circles. The reflectivity corresponding to the grating amplitude as determined from the electron microscopy images is drawn as thick line. On the right, a graphical representation of the grating shapes and numerical values of the parameters are shown.

The measured dispersion of the resonances on this grating, as a function of the grating amplitude is presented in Fig. 5.24 and the corresponding model calculation is shown in Fig. 5.25. The MO_1 resonance is relatively weak and weakens further with increasing amplitude, accompanied by a redshift. Similarly to the grating etched at 20°, for the highest amplitude, this resonance has died out and the ME_2 resonance comes in from the pseudocritical edge. This time, the appearance is predicted only for amplitudes that are slightly higher than measured. The measurements can be roughly assigned to the model calculations based on scaling factors between 0.5 and 1.1.

The ME_1 resonance is still showing a redshift with increasing amplitude. Its strength has increased compared to the less blazed grating profiles that were discussed before but it is still much weaker in the model calculation than in the experiment.

5.3.1.4 Etched at 40°

The measured and modelled reflectivity of a grating etched under 40° is shown in Fig. 5.26. There are still two resonances visible. But since the grating is already strongly blazed, they cannot be labelled as MO/ME resonances although they seem to evolve somehow from those.

This time, theory and experiment give the same wavelength where the short-wavelength-resonance is excited. A significant shift to shorter wavelengths of this feature is observed in comparison to the cases that were discussed above. The model calculation predicts that this resonance is expected to be very strong again. In the

measurement the strength is hard to estimate because of the finite resolution in wavelength.

The long wavelength resonance is again blue shifted in the measurement with respect to the model calculation. It is stronger compared to all other profiles that were investigated before. The absolute strength is underestimated in the model calculation.

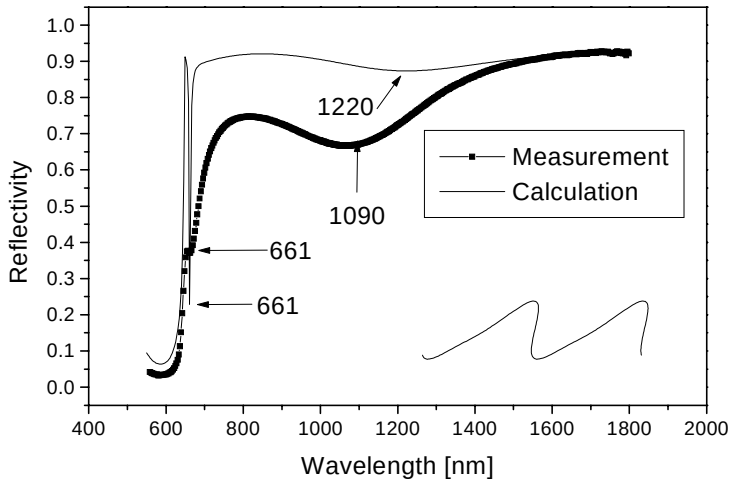

Fig. 5.26: Wavelength-dependent reflectivity of the grating etched at $\theta_{etch} = 40°$ as determined from a measurement compared to a model calculation. The surface profile as determined from the SEM-image is shown in the graph.

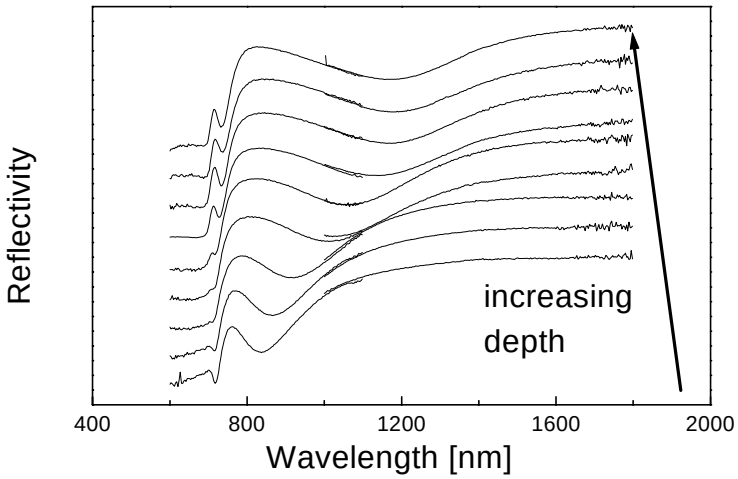

Fig. 5.27: Measured reflectivity of a gold grating etched under 40°. The deepest grating was measured first and then the amplitude was decreased by subsequent etching steps.

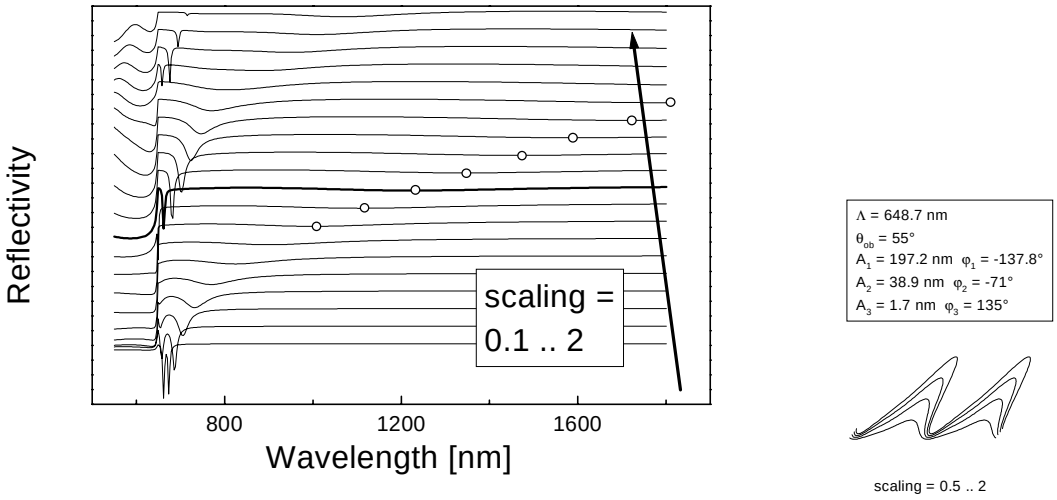

Fig. 5.28: Modelled reflectivity for $\theta_{etch} = 40°$ as a function of wavelength for different grating amplitudes. A weak resonance is marked by open circles where it is hard to see. The thick line corresponds to the surface profile as determined from electron microscopy (scaling factor of 1). On the right, a graphical representation of the grating shapes and numerical values of the parameters are shown.

The measured dispersion of the resonances on this grating, as a function of the grating amplitude is presented in Fig. 5.27 and the corresponding model calculation is shown in Fig. 5.28. In the measurement, the left resonance is first moving to shorter wavelengths with increasing amplitude, and comes back then to longer wavelengths when the grating amplitude is further increased. In the calculation, the resonance also first moves to the left, but it disappears completely left from the pseudocritical angle. With further increasing amplitude, a well pronounced resonance comes in again from shorter wavelengths, moving quickly to the infrared without disturbance. This suggests that the grating is already blazed so strongly that the original description as resonances having even and odd symmetry with mutual perturbation at the crossing points is not appropriate any more. The observed behaviour resembles already the reflectivity that is found for strongly overhanging structures (compare Fig. 5.14).

The long wavelength resonance may be identified with ME_1. It is still showing a redshift with increasing amplitude. It appears stronger than in the previously investigated cases. This tendency is reflected in the model calculation, too, but the absolute intensity of this resonance is predicted weaker than observed.

5.3.1.5 Overview on blazed gratings

The observations that were made regarding the impact of varying depth and asymmetry on the reflectivity of gold gratings are repeated here in a concentrated form to extract the important results. On the blazed gratings, three different types of resonances were observed for illumination by TE polarised light at $\Psi = 90°$, $\theta = 4°$: two resonances with a magnetic field with even symmetry of the magnetic field, ME_1 and ME_2, and one with odd symmetry, MO_1. In model calculations that are based on the independently

measured grating profiles, the essential features could be reproduced but there are some inconsistencies, too.

The first resonance with even magnetic field, ME_1, is shifting to the infrared and gets weaker with increasing grating amplitude. This effect is well reflected in the model calculation. The difference between predicted and measured position could be accounted for by applying a small scaling factor (ca. 0.9) to the grating profile in all cases except $\theta_{etch} = 20°$ (where the measured amplitude was too small). The strength of this resonance increases with increasing blazing of the grating profile. This is well reflected in the model calculations, while the theoretical prediction for the absolute depth of this resonance is significantly smaller in all investigated cases.

The reflectivity minimum close to the pseudocritical edge can be addressed as the first resonance with odd symmetry of the magnetic field (MO_1) for the $\theta_{etch} = 10°$, 20° and 30°-gratings. It shows a slight redshift with increasing amplitude. This is theoretically predicted but its exact position is observed at smaller wavelengths in the measurement than in the model calculation. This discrepancy cannot be overcome by a slight change of the grating amplitude. Presumably, in this case it would be necessary to introduce effects that are due to roughness of the grating. This resonance is fairly strong for the $\theta_{etch} = 10°$ grating and its strength decreases for increasing blaze. Additionally, this resonance dies out for the deepest measured $\theta_{etch} = 20°$ and $\theta_{etch} = 30°$-gratings. Both of the latter observations are made on the measurements as well as in the model calculations.

An additional reflectivity minimum is observed in the vicinity of the pseudocritical edge on the deepest 20° and 30° gratings that could be fabricated. The agreement of measurement and calculation regarding its strength and the grating amplitude of its appearance is satisfactory. This allows the conclusion that this is the second resonance with even symmetry of the magnetic field (ME_2).

The correct prediction of the appearance of ME_2 would require an increased amplitude for the model calculation, whilst the correct position of MO_1 requires a decreasing. This implies that there are still refinements in the mathematical modelling to be developed. Presumably, the incorporation of sample roughness would give better results. Alternatively, the preparation of gratings with less roughness may give better correspondence to theory.

The grating that was etched at 40° is already too strongly blazed for the resonances to be described in terms of the even and odd symmetry. This is reflected in the fact that the short wavelength minimum is fairly strong again, in contrast to the trend that was observed on the less strongly tilted gratings. Its position as a function of the grating amplitude differs significantly from the latter behaviour, too. Instead of a red shift, a ‘curve’, moving to the blue first and then coming back to the red is observed. All these aspects are surprisingly well reproduced in the model calculation.

Independent of grating shape and polarisation there is much less light reflected than predicted by the model calculations, especially close to the pseudocritical edge. This effect may be attributed to scattering on some random roughness of the samples.

No resonances are observed for TM polarised light. This indicates that the excitation of the observed minima requires a component of the electrical field normal to the metal / dielectric interface. This supports the interpretation of these resonances as self-interacting surface plasmons.

5.3.2 A stationary resonance

It was already pointed out by Wanstall et al. [Wan98] that the wavelength where resonances are found on very deep and overhanging gratings does not change when the (polar) angle of incidence of the incoming beam is varied in the classical mount. This is totally different from the behaviour of 'ordinary' surface plasmons on shallow diffraction gratings whose excitation wavelength obeys the momentum matching condition and is strongly angle-dependent (See Fig. 5.1). This theoretical prediction is checked here on the sample that was etched under θ_{etch} = 40°. The wavelength-dependent reflectivity is shown for polar angles between 4° and 54° as determined from measurement and modelling in Fig. 5.29. For the calculation, a linear scaling factor of sc = 0.95 was applied to the function representing the grating shape (compare Fig. 5.27) so that the minimum position for θ = 4° coincided with the one that was measured (λ = 1166 nm).

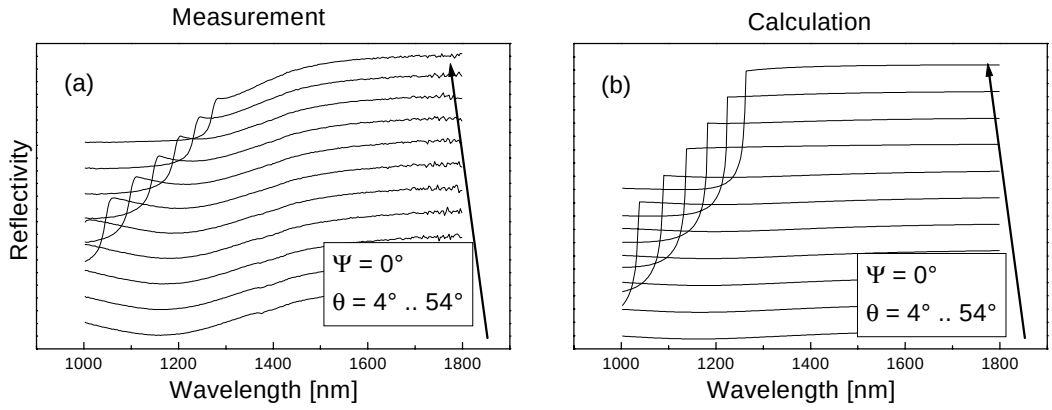

Fig. 5.29: Measured (a) and modelled (b) wavelength-dependent reflectivity of the grating that was etched at θ_{etch} = 40° as a function of wavelength. Different polar angles (θ) are chosen for Ψ = 0° (classical mount).

A good agreement between model calculation and measurement is observed with respect to the resonance wavelength of the broad minimum, until (at θ = 54°) the pseudocritical edge reaches the resonance and makes its observation impossible. It should be noted that this minimum is, as before, far deeper in the measurement than in the model calculation. The change of resonance wavelength with changing polar angle θ is far less pronounced

than for the ‘free’ surface plasmons on shallow gratings (compare Fig. 5.1). The remaining dispersion leads to the interpretation that this grating cannot be regarded as ‘very deep’ according to Wanstall et al.

5.3.3 The deep, symmetric grating

On the symmetrically etched gratings no deep resonances were observed for wavelength scans at normal incidence. This is shown in Fig. 5.30 where the wavelength-dependent reflectivity is plotted.

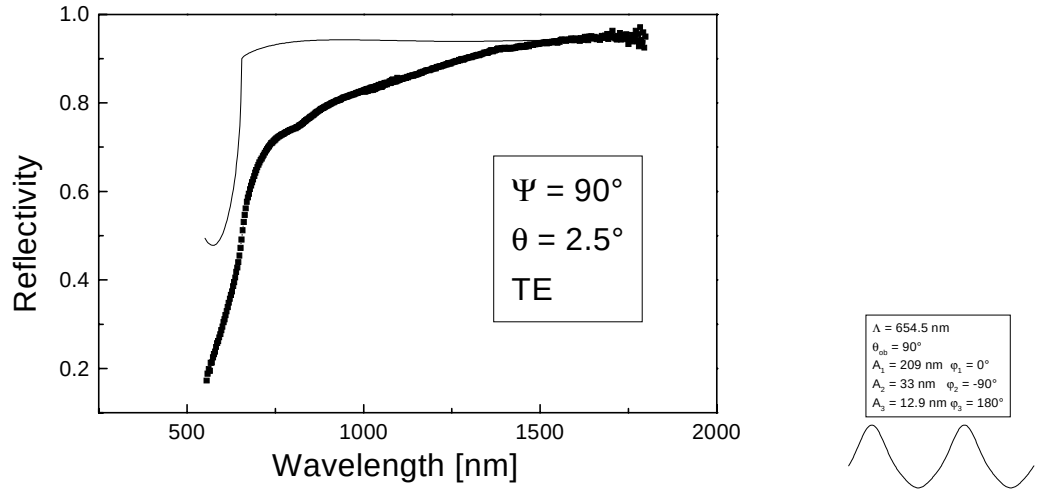

Fig. 5.30: Wavelength-dependent reflectivity of a symmetric grating. The dots mark measured points and the straight line is a model calculation based on the grating shape that is described by the parameters that are printed on the right together with a sketch of the surface profile.

It is clear that the coupling to a resonance with a magnetic field with odd symmetry (MO_1) to a symmetric problem is not possible because that would break the symmetry of the initial problem. The very weak minimum at λ = 812 nm in the measurement indicates that the etching process may have been not perfectly symmetric. The absence of the first resonance with even magnetic field cannot be explained by symmetry arguments, for a symmetric ‘broad peak’ grating as discussed in section 5.2.4. The very weak signature of this ME_1 indicates that the we are dealing with a ‘broad trough’ profile. For these calculations, the grating profile as indicated in Fig. 5.30 was used instead of the one that was determined by electron microscopy because the latter one would not have given the right position of the MO_1 resonance. However for the following considerations, this position with respect to the pseudocritical edge is important to know since it allows a comparison between model calculation and experiment.

In the following argument, the possibility to excite the MO_1 resonance on this grating by breaking the symmetry of the reflection geometry is illustrated by measurement and theoretical modelling (Fig. 5.31).

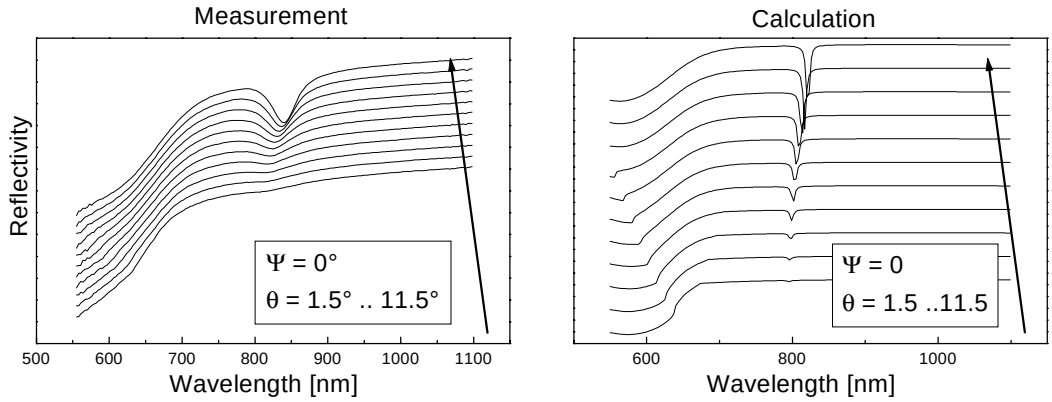

Fig. 5.31: Measured and modelled wavelength-dependent reflectivity (TM) of the symmetric grating for varying polar angle θ in the classical mount (Ψ = 0)

It is clearly seen by both experiment and theoretical modelling that for increasing polar angle θ, a distinct resonance is observed. This can be interpreted within the framework of symmetry considerations: the broken symmetry of the experimental geometry for $\theta \neq 0°$ allows coupling to the MO_1 resonance. It should be noted that the minimum shows a redshift for increasing polar angle θ. Comparison with Fig. 5.10 shows that this resonance has evolved from the LRSP in the shallow grating limit which exhibits a blue shift (compare Fig. 5.1) for increasing θ. This observation underlines the interpretation that MO_1 is a strongly localised resonance for a broad range of angles of incidence. In contrast, the LRSP that represents the limit of MO_1 for vanishing grating amplitudes is existing as a coupled resonance for normal incidence only (compare Fig. 5.1).

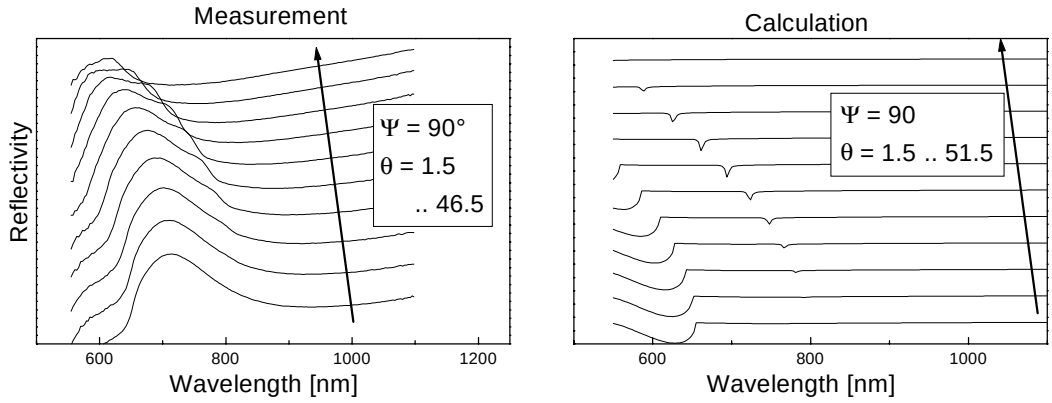

Fig. 5.32: Measured (a) and modelled (b) wavelength-dependent reflectivity of the symmetric grating for Ψ = 90° and varying θ.

An alternative way to excite the MO_1 resonance on a symmetric grating has been described by Watts et al. [Wat97] and was already mentioned in section 5.2.6. They

illuminate under $\Psi = 90°$ with TM[8] polarised monochromatic light. At the appropriate polar angle θ there is coupling possible because in this geometry the magnetic field has odd symmetry. Similarly, this resonance can be excited for $\Psi = 90°$ and fixed polar angle θ when the wavelength is varied. This is illustrated in Fig. 5.32. In the model calculation, a weak minimum is observed that shows a blue shift for increasing polar angle θ. For normal incidence, this resonance is not coupled to incident light because there is no component of the electrical field normal to the metal surface that may excite a charge density modulation. From symmetry considerations this resonance would be allowed.

The measurement, although looking quite different from the model calculations, shows some anomaly which does not exist for very small θ, and which shows the dispersion that is predicted for the MO_1. It is therefore tentatively assigned to this resonance.

Much more pronounced in the measurement is a broad minimum around $\lambda = 950$ nm which is completely missing in the model calculation. I do not have an explanation for that.

Another peculiarity is found on the symmetric grating that doesn't show up in the model calculation. It is presented in the next section and a 'handwaving' explanation given.

5.3.4 The photonic mode density on the surface

In the last section of this chapter, a phenomenon is described that was found in the experiment but not in the calculations. Fig. 5.33 shows the measured reflectivity of a symmetric grating as a function of wavelength in the classical mount ($\Psi = 0°$) for different polar angles θ, exceeding the ones that were already investigated in section 5.3.3.

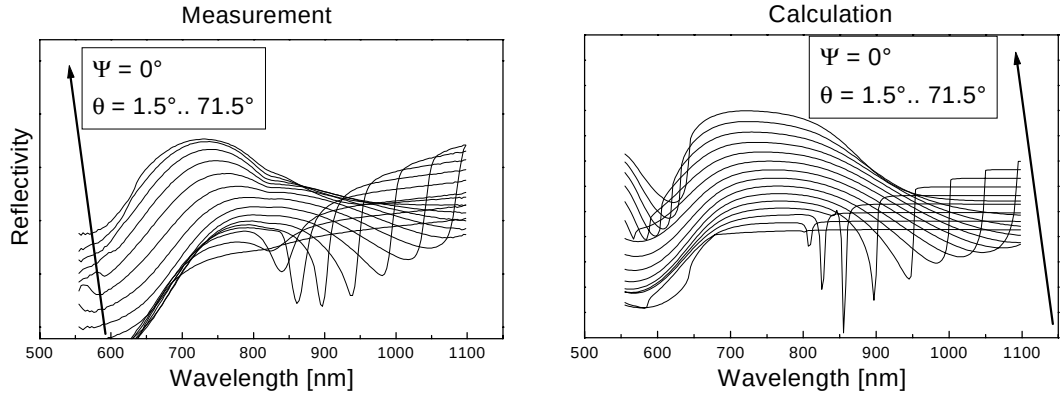

Fig. 5.33: Wavelength-dependent reflectivity of a symmetric grating in the classical mount ($\Psi = 0°$) for polar angles (θ) between 1.5° and 71.5° in measurement and model calculation.

[8] At first sight, it is surprising to excite any resonance in this polarisation because on shallow grating, surface plasmon excitation for $\Psi = 90°$ requires TE polarisation , compare chapter 7.

Some rapid changes in reflectivity with wavelength are observed due to different mechanisms. At $\theta = 1.5°$, the MO_1 resonance is located at 812 nm. For increasing polar angle, it gets deeper due to the broken symmetry, and shows a redshift. The pseudocritical edge is found at 676 nm for $\theta = 1.5°$ and this shifts to the red, too. These two effects can be found in the model calculation, but a third effect is only visible in the experiment: A kink at $\lambda = 820$ nm that is completely independent from the angle of incidence and becomes more pronounced for increasing polar angle. The following explanation for this kink is proposed:

The existence of a surface resonance enhances the number of possible electromagnetic waves with a given frequency. This concept of 'photonic mode density' will be explored in more detail in chapter 7. This has the consequence that random scattering processes become stronger when surface resonances with the appropriate wavelengths are supported because new decay channels are established for the photon. Since the kink is observed at the shortest possible wavelength where the MO_1 resonance may be excited, it is attributed to these additional 'photonic modes', that are introduced for wavelengths that are exceeding 820 nm.

5.4 Conclusion and outlook

The reflectivity of deep gratings with different depths and degrees of asymmetry was investigated in this chapter. First, an overview of the resonances that are supported by deep metallic gratings was given, based on model calculations. By considering the symmetry of the electromagnetic field distributions, the observations that are known from literature, as well as effects that are presented here for the first time could be assigned to two families of resonances, that are characterised by a magnetic field with either even (ME) or odd (MO) symmetry.

On asymmetric metallic gratings, two ME-resonances and one MO resonance were identified in experiments and their dispersion and strength was found to be in satisfactory agreement with model calculations. A theoretical prediction about a strongly decreased effect of the angle of incidence on the resonance wavelength, could be experimentally verified

On symmetric metallic gratings, the possible geometries that allow coupling to the MO_1 resonance can again be explained by symmetry considerations. Illustrative experimental and theoretical results were presented.

Some other experimental observations were not reflected by the theoretical modelling. Scattering processes may explain the reduced reflectivity close to the pseudocritical edge in all measurements, and the appearance of a stationary kink that was discussed in section 5.3.4. A broad minimum that was found experimentally on symmetric gratings in section 5.3.3 is not yet explained.

Many questions remain open after these investigations and give a strong motivation to continue working on deep metallic gratings. The most obvious challenge is the

preparation of deeper grating structures in order to see the higher order members of the two families of resonances. A classification of the possible resonances that is valid not only on symmetric and slightly blazed gratings, but for all possible shapes of the grating surface is still to be developed. The introduction of scattering processes in the modelling routine may allow one to eliminate the discrepancies between theory and measurement.

Finally, a structure that has a dispersion-free resonance, not only for variation of θ but although for Ψ, would be interesting for potential applications. A chemically and thermally inert material would be available that has a well-defined absorption- and therefore emission maximum, which can be tuned within a broad wavelength range. One example where such material properties are desirable is solar energy applications [Boe99].

6 Fluorescence in the field of coupled surface resonances

In this chapter, the effect of a nearby metallic diffraction grating on the excitation and emission properties of fluorescing molecules is examined. In section 6.1, some background on coupled surface resonances and fluorescence near interfaces is reviewed. A theoretical approach to the problem is discussed in 6.2. Then, after experimental details (6.3), the results are presented and analysed in 6.4. Finally (6.5), the effect of 'selective bleaching' is discussed and a possible application is proposed.

6.1 Introduction

Some concepts underlying the investigations in this chapter require explanation.

First, the existence of a 'photonic band gap' for monochromatic illumination is demonstrated for the sample under investigation: a golden diffraction grating with a dielectric coating. A special emphasis lies on the strong localisation of the electrical field of the coupled resonances opposed to the free surface plasmons outside the band gap that is obtained by numerical modelling. Then, the influence of the dielectric environment on the excitation and the decay channels of a fluorescing molecule is briefly discussed. This will finally lead to the underlying idea of the experiments that are presented in this chapter: The fluorescent molecules on the surface can be divided into two ensembles lying on closely spaced stripes having different excitation and emission characteristics.

6.1.1 The structure under investigation

The studies presented in this chapter are made on the 3-layered grating structure that is schematically depicted in Fig. 6.1. A thin (ca. 20 nm) polymer film is spin coated on a blazed gold grating. It is assumed that the surface structure of the polymer film follows the grating surface.

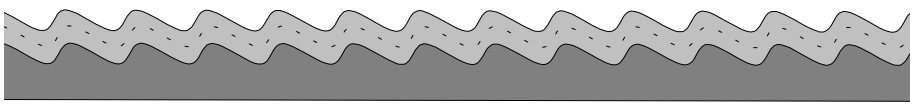

Fig. 6.1: Scheme of the structure under investigation. A blazed gold grating is coated with a dielectric film (polymer). The modulation height is strongly exaggerated. The dashed line indicates the middle of the polymer film.

6.1.2 Photonic band gaps with monochromatic light

The formation of a photonic band gap in the reflectivity of a golden diffraction grating was already discussed in detail in chapter 5. There, the wavelength-dependent reflectivity at varying polar angle , $\theta(\lambda)$ was recorded. It turned out that the simple model of momentum matching of the diffracted orders of the grating with the surface plasmon resonance (see chapter 2) could be applied at non-normal incidence. At normal incidence, a splitting of the reflectivity minimum into two coupled resonances, the LRSP and the SRSP was observed. When the position of these resonances is plotted in the plane spanned by the wavelength λ and the polar angle θ, a structure is observed that is analogous to the bandgap of electronic states in a crystal. For this reason, the splitting of the surface plasmon in the λ/θ plane into two coupled resonances is referred to as 'photonic band gap'. The prerequisite for this splitting is that $+1^{st}$ and -1^{st} order surface plasmons are excited simultaneously and that the second harmonic of the grating profile provides the momentum to couple these two modes.

Mills [Mil77] was the first to demonstrate that coupled resonances will be formed whenever the propagation direction of the incoming beam is orthogonal to the reciprocal grating vector. In terms of the parametrization of the experimental geometry as it is used here, this is the case for $\Psi = 90°$ for any θ. This fact allows the observation of photonic band gaps with monochromatic light. For the appropriate choice of the grating pitch Λ and the wavelength of light λ, the two surface plasmons that are coupled to the incident light in first order may cross in the plane spanned by θ and Ψ and a band gap may be observed.

This is illustrated in Fig. 6.2 where the measured reflectivity of a blazed, polymer-coated gold grating is plotted as a function of the two angles of incidence Ψ and θ for $\lambda = 632.8$ nm. The dark stripes can be attributed to the coupling of the incident light to the surface plasmon resonance in $+1^{st}$ and -1^{st} order. Far away from $\Psi = 90°$, the two minima are independent and their position can be found by the momentum matching condition. But instead of crossing each other at $\Psi = 90°$, there are two clear minima for $\Psi = 90°$. The lower and narrower branch evolves into the plasmon coupled in $+1^{st}$ diffracted order for $\Psi < 90°$ and into the one coupled in -1^{st} diffracted order for $\Psi > 90°$. Similarly, the upper, broader branch can be followed to become the surface plasmon coupled in $+1^{st}$ order ($\Psi > 90°$) and -1^{st} order ($\Psi < 90°$). These resonances are identified with the narrow LSRP and the broad SRSP that were introduced in chapter 5.

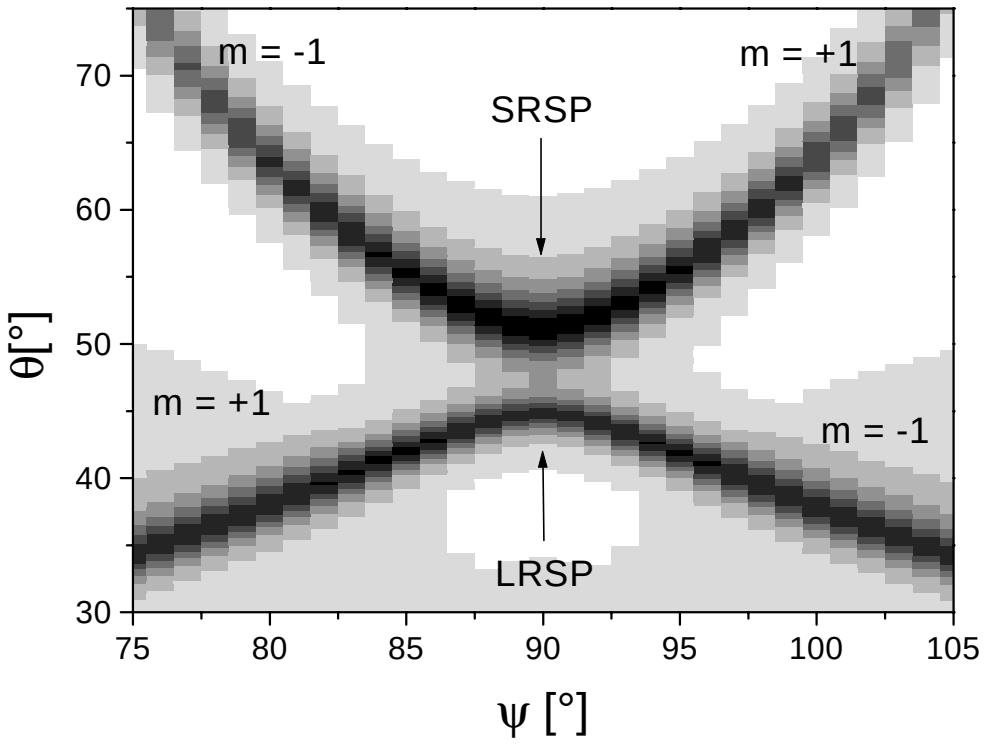

Fig. 6.2: Measured reflectivity of a gold grating with a dielectric coating for TE-polarised light with λ = 632.8 nm as a function of polar angle θ and azimuthal angle Ψ. The grey values represent the reflectivity, from white (1) to black (0).

When the same experiment is performed with another wavelength, a similar reflectivity behaviour can be observed. The only significant difference is a shift of the resonances in their polar angle (θ). This is demonstrated in Fig. 6.3 in a model calculation of the reflectivity of the same grating structure when the illuminating light has a wavelength of 670 nm.

In chapter 5 the characterisation of the different kinds of coupled resonances was based on their magnetic field distributions in the vicinity of the grating surface. Since for fluorescence phenomena, the electrical field is the driving force, we will turn our attention now to the electrical field distributions. Unlike at normal incidence, here all three Cartesian components are not vanishing and therefore the (time independent) electrical field is given by the complex vector

$$\mathbf{E}(\mathbf{x}) = \begin{pmatrix} E_x \cdot e^{i\cdot\varphi_x} \\ E_y \cdot e^{i\cdot\varphi_y} \\ E_z \cdot e^{i\cdot\varphi_z} \end{pmatrix} \qquad (6.1)$$

where each Cartesian component is given by its modulus and its phase. The averaged electrical field strength E is defined as

$$E(\mathbf{x}) = \sqrt{\left[E_x(\mathbf{x})\right]^2 + \left[E_y(\mathbf{x})\right]^2 + \left[E_z(\mathbf{x})\right]^2} \qquad (6.2)$$

Four 'typical' electric field distributions are shown in Fig. 6.4, chosen to represent the coupled modes as well as the 'freely' propagating surface plasmons. In Fig. 6.3 the selection of the chosen angles of incidence is indicated.

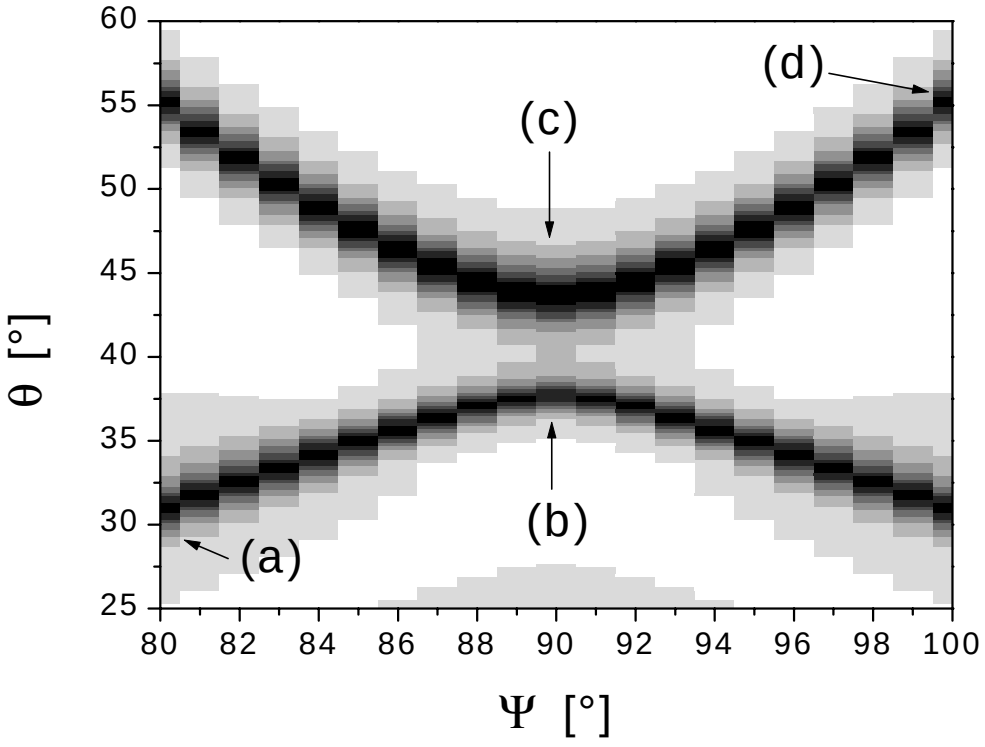

Fig. 6.3: Modelled reflectivity of a gold grating with dielectric coating for TE-polarised light with λ = 670 nm as a function of polar angle θ and azimuthal angle Ψ. The grey values represent the reflectivity, where white indicates maximum (1) and black a reflectivity of 0.

Fig. 6.4 (b) and (c) correspond to the two coupled resonances. A strong lateral modulation of the strength of the electrical field along the grating surface is observed, showing that the coupled modes are highly localised. By comparison of the two field distributions, one observes the coincidence of the minima of the LRSP (b) with the maxima of the SRSP (c) and vice versa. As it has been shown for the magnetic fields in chapter 5, it is the second harmonic of the grating profile that determines the positions of the maxima of the electric field. The positions of maximum field strength of the SRSP coincide with the maxima of the second harmonic of the grating profile while the LRSP has its maximum electric field in the minima.

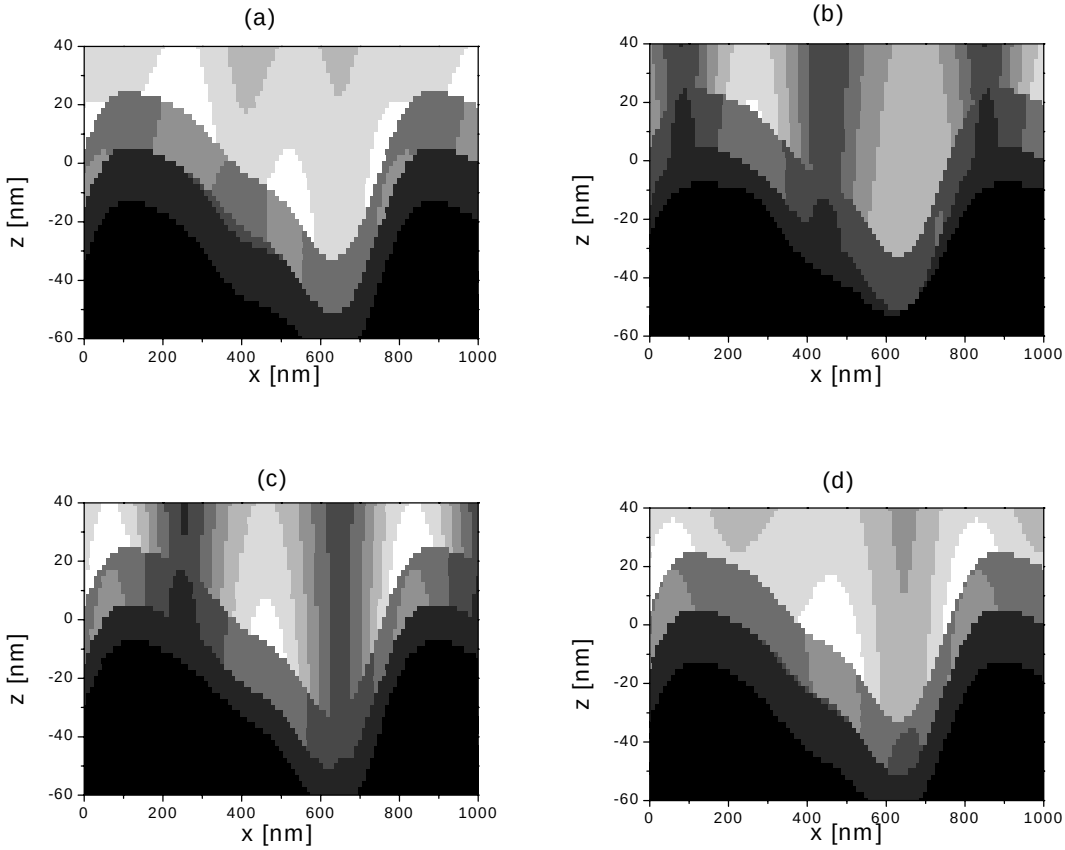

Fig. 6.4: Distributions of the electrical field strength over one grating period for gratings illuminated at
(a) Ψ=80°, θ = 31.1° (m = +1)
(b) Ψ=90°, θ = 37.7°, (LRSP)
(c) Ψ=90°, θ = 43.7°, (SRSP)
(d) Ψ=100°, θ = 55.1°, (m = +1)
White corresponds to maximum, black to vanishing field.

For the ‘normal’ surface plasmons outside the band gap region (a) and (d) there is some lateral variation in the electrical field strength visible, but it is much weaker and the correlation of the maximum position with the second harmonic of the grating profile is gone. This is the expected behaviour for surface plasmons, propagating like 2-dimensional light waves along the interface.

The contrast between these resonances can be seen clearer in Fig. 6.5, where the electric field distribution along a line 10 nm above the metal surface (which is the middle of the polymer layer, compare Fig. 6.1) is plotted. Neglecting some perturbation at 650 nm (right in the gratings minimum), the two coupled resonances show electrical field distributions that are close to sinusoidal and phase-shifted by 180° with respect to each other. The other two distributions show much less variation in intensity and the correlation to the maximum / minimum-positions of the second harmonic of the grating profile is very weak.

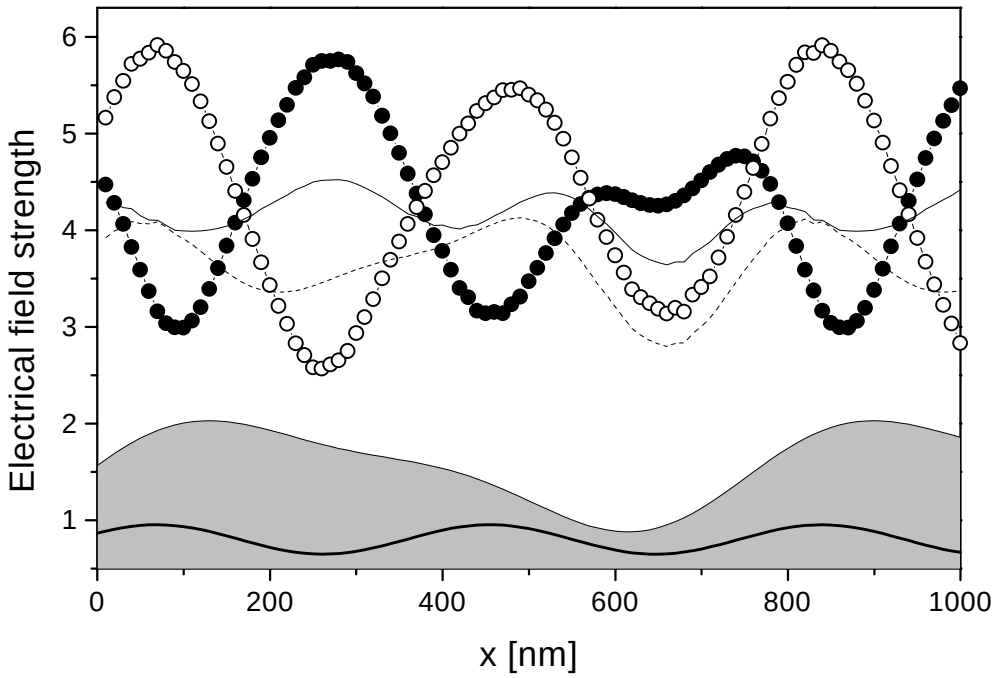

Fig. 6.5: Electrical field strengths at a constant distance of 10 nm above the metal surface for the 4 cases depicted in Fig. 6.3.
(a): $\Psi = 80°$, $\theta = 31.1°$, straight line, free surface plasmon (m = +1)
(b): $\Psi = 90°$, $\theta = 37.7°$, full circles, LRSP
(c): $\Psi = 90°$, $\theta = 43.7°$, open circles, SRSP
(d): $\Psi = 100°$, $\theta = 55.1°$, dashed line, free surface plasmon (m = +1)
The total grating profile is indicated as a grey area graph, the thick line represents the second harmonic component.

This observation shows that by adjusting the angle of incidence, an experimental parameter which can be easily varied, it is possible to set up high electrical field strengths which have a characteristic lateral distribution. They show a modulation which has half the wavelength of the fundamental period of the grating.

6.1.3 Fluorescent dyes in inhomogenous dielectric surroundings

6.1.3.1 The density of states

Fluorescing dyes (Chromophores) absorb light of a certain wavelength spectrum and re-emit light with a spectrum of longer wavelengths, corresponding to lower energies. As an easy model, the excitation of a chromophore can be described as the local electric field driving a dipole. Then, the probability for excitation will depend on the strength of the electric field. When the electrical field of an incoming light beam is enhanced by an appropriate dielectric environment, the excitation probability will be enhanced, too and the result is an increased fluorescence. An enhancement factor of 20 can be achieved by

surface plasmon coupling on gold films in Kretschmann geometry and has been extensively applied to biochemical problems [Lie99]. Similar approaches based on dielectric optical waveguide geomtries have been reported [Bus00], [Plo96]

Not only the excitation probability is sensitive to the dielectric environment of the dye molecule. According to Fermis golden rule, the emission probability P_{em} of the chromophore from the excited state m to the ground state k depends both on the intrinsic properties of the molecule and on the surrounding.

$$P_{em} = \frac{4 \cdot \pi^2}{h} \left| V_{mk} \right|^2 \cdot \sigma_{mk} \qquad (6.3)$$

The matrix element V_{mk} gives the intrinsic probability of the emitter to relax from the excited state m into the ground state k and its calculation requires a quantum-mechanical treatment which is tedious for large organic molecules. The influence of the surrounding environment on the emission characteristics comes in via σ_{mk}, the 'density of states' or number of decay channels for the emission process. For a detailed description of the quantum mechanical treatment of excitation and emission of fluorescent dyes, the reader may choose from many standard textbooks such as [Hin85].

A simple geometry where the influence of the density of states on the emission characteristics has been studied extensively in theory and experiment are one or more plane interfaces in front of which the excited dipole is placed. This work is comprehensively treated in a review article by Barnes [Bar98]. A single metal surface [Dre70] provides a good illustration for the influence of the environment on the emission characteristics of an excited chromophore. The surface plasmon resonance provides a significant enhancement of decay channels (density of states) for dye molecules that are in close enough proximity to the interface. This is reflected in a drastically reduced lifetime of the excited state when the emitter is placed within 20 nm of the interface.

6.1.3.2 The modulated interface

The mathematical problem of an emitter situated close to a periodically modulated surface is much more challenging than the case of the plane surface mentioned above. To my knowledge [Bar00], there have been no successful attempts to solve it exactly. Still, there was considerable experimental work in this field. The first proof that the surface plasmon as an intermediate state plays an important role for the coupling of the excitiation energy of a chromophore to light was given in the early 80's by Knoll et al. [Kno81]. The diffraction grating provides coupling between surface plasmons and light and the momentum matching condition (compare chapter 2) appropriately reproduces the observed directions of enhanced emission.

During the last few years additional work was carried out in the field. Studies with fixed emission wavelength and direction were performed by Andrews et al. [And97]. He varied the polar angle and the wavelength of the excitation beam, producing a band gap

structure similar to the ones shown in Fig. 6.2. It was observed that the emission intensity of the dye exhibits the same band gap structure as the reflectivity. Low reflectivity implies effective excitation of the surface plasmon resonance and is reflected in an enhanced emission.

Kitson et al. used monochromatic excitation at fixed angle and extended the observation of surface plasmon enhanced fluorescence decay to the complete half-sphere over the grating [Kit96b]. Especially, experimental geometries where the emission process takes place over coupled resonances were investigated in [Kit95]. There are always emission maxima when there would be reflectivity minima in a reflection experiment performed with the emission wavelength. This includes the formation of a band gap like structure in the emission intensity recorded over the whole half sphere above the grating.

The experiment that will be presented in this chapter is a somewhat natural extension of these investigations: both the excitation and the emission of the dye molecules will involve the surface plasmon resonance as an intermediate step. This will yield new insight that could not be obtained by having surface plasmons involved in only one of these two processes. Especially when we are dealing with coupled surface resonances, the field intensities vary strongly along the interface (See Fig. 6.5). This implies that the excitation probability of a molecule close to the surface depends strongly on its position along the surface of the grating. So, in a simplified view, there are two sets of chromophores: the ones being placed in the field maxima of the LRSP and the other ones placed in the field maxima of the SRSP (see Fig. 6.5). We are able to excite selectively one of the two sets of chromophores by choosing the appropriate excitation angle[9].

If the optimum excitation angle of a certain molecule depends on its position on the grating, it should be expected that the same holds for the angle under which the strongest emission can be observed. Considering a molecule positioned at the intensity maximum of the LRSP, the coupling to this surface resonance will be stronger than to the SRSP. Therefore, it is expected to lose its energy predominantly to the LRSP.

The concept presented above allows selective excitation of a part of the molecules on the interface as well as selective fluorescence read out. Since the two groups of dye molecules are defined as the ones positioned either in the maxima or in the minima of the 2nd harmonic of the grating profile, their lateral distance is very small (less than 200 nm from maximum to minimum excitation in our case.). As a next step, a model will be presented that allows a quantitative modelling of this effect.

[9] It should be mentioned here that the separation between the two sets is not perfect, and the model of two separated populations of chromophores is used here only to illustrate the basic idea. A more realistic description will be given in the theoretical section (6.2).

6.2 Two models for the fluorescence intensity

In this section, a model will be set up to calculate the fluorescence intensity of molecules being randomly distributed over the polymer layer on top of the grating (See Fig. 6.1). The direction of the exciting laser beam and the direction of the emission (specified by the position of the detector) are the free parameters. First, the cross sections of the excitation and emission will be calculated for one single molecule. Then, the expected fluorescence intensity is obtained by an appropriate averaging procedure.

6.2.1 Cross section for the excitation process

In our experiments, a two-step process has to be considered for each molecule. First, the excitation probability for a given molecule at the position **x** with the transition dipole moment for the excitation $\mathbf{r_{ex}}$ must be determined. The exciting light wave is specified by a fixed wavelength λ_{ex}, the direction of incidence, given by the solid angle Ω_{ex} and its polarisation. The absorption process is described as the excitation of an electrical dipole with a fixed oscillation axis by the incident electrical field. The detailed theory of this model can be found in the literature, e.g. [Hin85]. Essentially, the transition probability for the excitation process P_{ex} is calculated by using Fermi's golden rule (Equation (6.3)).

For a fixed direction of the dipole, the transition matrix element is given as

$$V_{mk} = -\mathbf{r}_{ex} \cdot \mathbf{E} \qquad (6.4)$$

Where **E** is the (time independent) electric field. Therefore, the probability for the excitation P_{ex} will have the form

$$P_{ex}\left(\mathbf{x}, \mathbf{r}_{ex}, \Omega_{ex}\right) = Const \cdot \left(\mathbf{E}\left(\mathbf{x}, \Omega_{ex}\right) \cdot \mathbf{r}_{ex}\right) \cdot \left(\mathbf{E}\left(\mathbf{x}, \Omega_{ex}\right) \cdot \mathbf{r}_{ex}\right)^{*} \qquad (6.5)$$

where the asterisk denotes the complex conjugate.

6.2.2 Cross section of the emission process

The second step that must be modelled theoretically is the emission process. A complete treatment of the problem would involve calculating the electric field of the oscillating dipole with the appropriate boundary conditions imposed by the grating. From this, the probability that the light is emitted into a certain solid angle (the detector) could be derived. Additionally, the photonic energy that is lost in the gold could be tracked. But since no mathematical algorithms are known to solve this problem, this exact approach cannot be used.

For this reason, a simpler approach is chosen to calculate the probability of the emitter to radiate its energy into a certain solid angle. It is based on viewing the dye molecule and the detector as two systems that may exchange energy by a photon. The direction of the energy exchange that we are interested in, from the dye molecule to the detector cannot be directly calculated. The reverse direction would be an emitter at the detector

position transferring its energy to the dye molecule at the grating surface. This problem has already been solved in the previous section and is easily adapted by changing the wavelength of the radiation to the emission wavelength of the fluorescent molecule. Because the coupling strength is equal for both directions of the energy transfer, our problem is solved. The following equation gives the relative probability P_{em} for a given emitting dipole to radiate its energy into a certain direction:

$$P_{em}\left(\mathbf{x}, \mathbf{r_{em}}, \Omega_{em}\right) = Const \cdot \left(\mathbf{E}\left(\mathbf{x}, \Omega_{em}\right) \cdot \mathbf{r_{em}}\right) \cdot \left(\mathbf{E}\left(\mathbf{x}, \Omega_{em}\right) \cdot \mathbf{r_{em}}\right)^{*} \qquad (6.6)$$

where the vector $\mathbf{r_{em}}$ denotes the transition dipole moment for the emission process and $\mathbf{\Omega_{em}}$ the solid angle of detection.

One disadvantage of this approach should be mentioned here. All information about decay channels that are not ultimately transferred into plane light waves is lost, therefore we cannot give absolute probabilities that the excitation energy of the dye molecule will be transformed in a photon, travelling in a certain direction. As long as it can be assumed that the density of alternative decay channels is not rapidly varying along the grating surface, this approach is applicable for the calculation of an emission pattern, where only intensities at different emission directions are compared.

6.2.3 The appropriate averaging procedure

The next step consists of averaging over all molecules that are involved. It is assumed that they are randomly distributed within the polymer layer and randomly oriented. The probability that fluorescence light is detected in the emission direction Ω_{em} upon irradiation under the excitation direction Ω_{ex} will be an average over all molecules.

First, the average is taken over the different orientations of the molecules. If the transition dipole moments for excitation and emission are collinear and the molecules do not rotate between absorption and emission, the directional average has to be taken over the combined process as well. In this case, the probability for the combined excitation-emission process, averaged over all possible directions, P_{da} will be given by

$$P_{da}\left(\Omega_{ex}, \Omega_{em}, \mathbf{x}\right) \propto \left\langle P_{ex}\left(\Omega_{ex}, \mathbf{x}, \mathbf{r}\right) \cdot P_{em}\left(\Omega_{em}, \mathbf{x}, \mathbf{r}\right) \right\rangle_{\mathbf{r}} \qquad (6.7)$$

where the brackets denote the averaging and the vector **r** is the (common) direction of the transition dipole moment. Inserting equation (6.5) and (6.6) yields

$$\begin{aligned} P_{da}\left(\Omega_{ex}, \Omega_{em}, \mathbf{x}\right) \propto & \left|E_x^{ex}\right|^2 \cdot \left[\frac{3}{8}\left|E_x^{em}\right|^2 + \frac{1}{8}\left|E_y^{em}\right|^2 + \frac{1}{8}\left|E_z^{em}\right|^2\right] + \\ & \left|E_y^{ex}\right|^2 \cdot \left[\frac{1}{8}\left|E_x^{em}\right|^2 + \frac{3}{8}\left|E_y^{em}\right|^2 + \frac{1}{8}\left|E_z^{em}\right|^2\right] + \\ & \left|E_z^{ex}\right|^2 \cdot \left[\frac{1}{8}\left|E_x^{em}\right|^2 + \frac{1}{8}\left|E_y^{em}\right|^2 + \frac{3}{8}\left|E_z^{em}\right|^2\right] + \\ & \frac{1}{2} \cdot \left[\left|E_x^{ex} \cdot E_y^{ex}\right| \cdot \left|E_x^{em} \cdot E_y^{em}\right| + \left|E_x^{ex} \cdot E_z^{ex}\right| \cdot \left|E_x^{em} \cdot E_z^{em}\right| + \left|E_y^{ex} \cdot E_z^{ex}\right| \cdot \left|E_y^{em} \cdot E_z^{em}\right|\right] \end{aligned} \qquad (6.8)$$

In this equation, the dependence of the electrical field on **x** and Ω_{ex}/Ω_{em} is not explicitly written for readability.

If the transition dipole moment varies for the excitation and the emission process, either on the molecular level or due to rotation of the chromophore, the average over orientations must be taken separately. One simple model may be set up based on the assumption is that there is no correlation between the excitation and emission processes. In this case, the directional averages must be determined independently, therefore the directionally averaged emission probability equals

$$P_{da}\left(\Omega_{ex},\Omega_{em},\mathbf{x}\right) \propto \left\langle P_{ex}\left(\Omega_{ex},\mathbf{x},\mathbf{r_{ex}}\right)\right\rangle_{\mathbf{r_{ex}}} \cdot \left\langle P_{em}\left(\Omega_{em},\mathbf{x},\mathbf{r_{ex}}\right)\right\rangle_{\mathbf{r}_{em}} \qquad (6.9)$$

With equations (6.5) and (6.3), this yields

$$P_{da}\left(\Omega_{ex},\Omega_{em},\mathbf{x}\right) = Const \cdot \frac{1}{4} \cdot \left|\mathbf{E}\left(\Omega_{ex},\mathbf{x}\right)\right|^2 \cdot \left|\mathbf{E}\left(\Omega_{em},\mathbf{x}\right)\right|^2 \qquad (6.10)$$

Finally, these probabilities are spatially averaged over all possible positions of the dye molecule in order to obtain the fluorescence intensity I for a given direction of excitation and emission

$$I\left(\Omega_{ex},\Omega_{em}\right) \propto \frac{\sum_{\mathbf{x}} P_{da}\left(\Omega_{ex},\Omega_{em},\mathbf{x}\right)}{N} \qquad (6.11)$$

where N denotes the number of points where the above equations are evaluated. The electric field distributions that were needed for these calculations were obtained with the numerical modelling program ‘oblique’. For a number of discrete points the electric fields were determined and the expressions (6.8) and (6.10) evaluated for each point before the averaged value was determined. The points were chosen equally spaced on a line reproducing the surface profile right in the middle of the polymer layer (along the dashed line in Fig. 6.1). This turned out to give a good approximation to an average over the entire layer because a vertical displacement of the selected points gives an almost linear variation in the calculated fluorescence intensity, not exceeding 10 % of the absolute value.

6.3 Experimental

6.3.1 Sample preparation

From initial calculations, gratings with a period of ca. 750 nm and an amplitude of 20 - 30 nm of the first harmonic component of the surface profile turned out to be best suited for our investigations. Additionally, a strong blazing of the structure is necessary to get significant coupling to both branches of coupled surface resonances (see chapter 5).

A photoresist grating was prepared as described in chapter 3 with a photoresist thickness of 50 nm. Then, the sample was exposed to a normally incident ion beam for 1 minute

and to a beam incident under an angle of 75° relative to the surface normal for further 9 minutes. By thermal evaporation, the sample was covered with an optically thick (150 nm) gold film. A thin, thermally evaporated chromium film between glass and gold was used for better adhesion between the two materials.

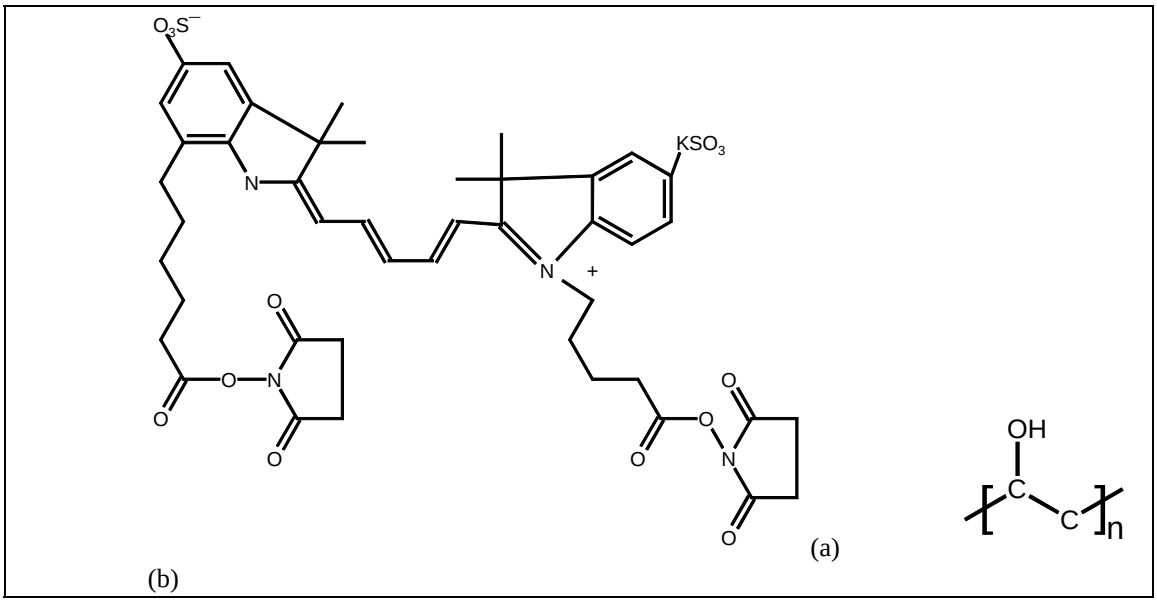

Fig. 6.6: Chemical structure of the chromophore Cy5 (a) and Poly (vinyl alcohol) (b).

A thin film of poly-(vinyl alcohol) with the Chromophore Cy5, bound to streptavidin, as the guest-host system was spin-coated out of aqueous solution (containing 1 weight % polymer) at 4000 RPM. Fig. 6.6 shows the structure of the Cy5-dye and of Poly(vinylalcohol). Streptavidin is a very complex biological molecule, its structure can be found in [Hen89]. For these experiments, it is used as an anchor for the fluorescent dye only, its exact structure is of no importance.

6.3.2 Experimental set-up

The grating was mounted in Ψ_{ex} = 90°-geometry on the set-up that is depicted in Fig. 6.7. The beam of a HeNe Laser (λ = 632.8 nm) is attenuated and fixed to TE-polarisation by two polarisers. Immediately in front of the sample all frequency components but the fundamental are removed from the laser beam with an interference filter (633 ± 3 nm). Pinholes remove stray light from the optical path and a shutter blocks the laser beam when no data is taken in order to minimise photobleaching of the dye molecules. All components are mounted on an optical bench.

The incident beam intersects the axis of a goniometer which is normal to the drawing plane. There, the sample is mounted with the grating grooves lying in the plane of incidence and the goniometer axis lying in the sample surface (Ψ = 90° geometry).

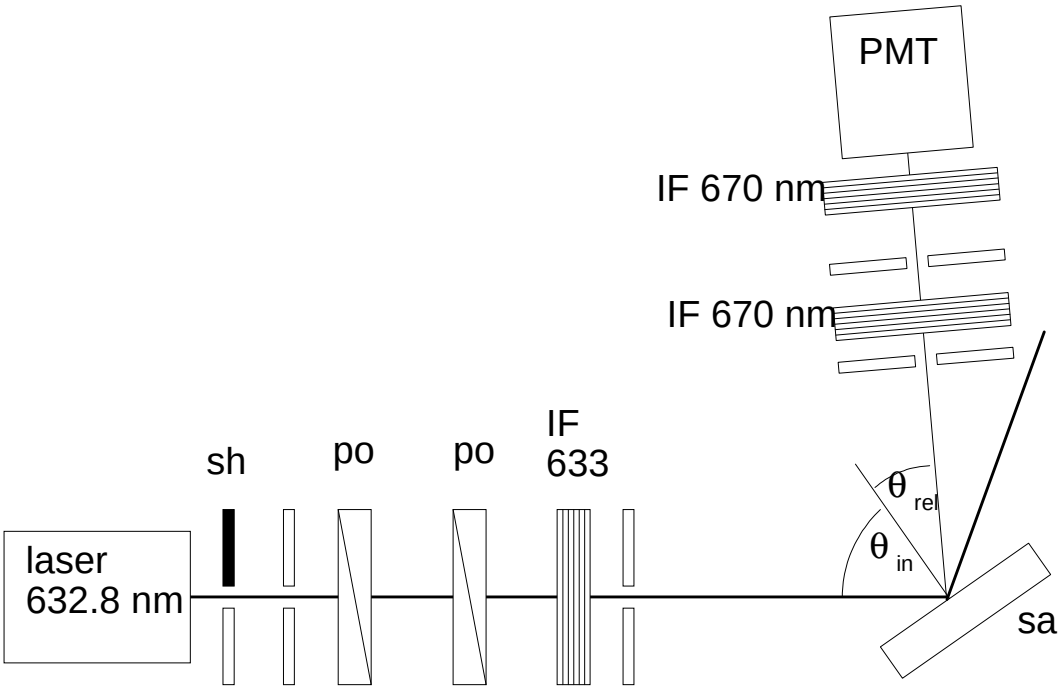

Fig. 6.7: Schematic experimental set-up: The abbreviations stand for Shutter (sh), polarizer (po), interference filter (IF), sample (sa) and photo multiplier tube (PMT)

On the detection axis, the fluorescence intensity generated on the sample surface is measured as a function of its direction: a pinhole (diameter 2 mm) determines the solid angle relative to the sample that is investigated. Its distance to the sample being 150 mm leads to an angular resolution of 0.76°. An interference filter (670 ± 3 nm) removes all frequency components in the light except the one corresponding to the wavelength of the emission maximum of the dye. A pinhole reduces stray light before the light reaches the photomultiplier tube. All these components are mounted together rigidly and the entire detection unit is mounted on a second (detector-) goniometer with an axis that coincides with the one of the sample goniometer. The detection unit can be moved vertically (normally to the plane of the drawing in Fig. 6.7) in order to investigate Ψ_{em} other than 90°. In this case, the optical axis of the detection system still must point towards the sample. The required tilting is established with the aid of a ball joint which links the detection system to an optical bench that is screwed on the detector goniometer. The direction of emission that is investigated in this case is defined by the angle between the axis of the detection system and the plane of incidence, Ψ_{tilt}:

$$\Psi_{tilt} = \arctan\left(\frac{h}{d}\right) \qquad (6.12)$$

with the height h of the first pinhole over the plane of incidence and the distance d which is the projection of the detection axis onto the plane of incidence. As a second degree of freedom, the detector can be moved on a circle around the sample by the detector-goniometer. Its position is determined by the 'relative polar angle' θ_{rel} which is defined as the angle between the surface normal of the sample and the projection of the detection axis onto the plane of incidence. It should be mentioned here that θ_{rel} and Ψ_{tilt}

which can be varied with the experimental set-up are not equal to the polar angle θ_{em} and the azimuthal angle Ψ_{em} which are defined according to the notation for reflection geometry as introduced in chapter 2. The latter ones are the parameters used in the model calculations to describe the solid angle of the outgoing radiation. By basic trigonometry it can be shown that

$$\tan(\theta_{em}) = \frac{\sqrt{\left[\sin(\Psi_{tilt})\right]^2 + \left[\sin(\theta_{rel}) \cdot \cos(\Psi_{tilt})\right]^2}}{\cos(\Psi_{tilt}) \cdot \cos(\theta_{rel})} \qquad (6.13)$$

$$\tan(\Psi_{em} + 90°) = \frac{\sin(\Psi_{tilt})}{\sin(\theta_{rel}) \cdot \cos(\Psi_{tilt})} \qquad (6.14)$$

These relations allow a comparison between model calculation and experiment. Note that for detection in the plane of incidence($\Psi_{tilt} = 0°$), the above expressions reduce to $\Psi_{em} = 90°$, $\theta_{em} = \theta_{rel}$.

6.3.3 Additional data treatment

During the measurement there was significant photobleaching of the dye. For the series of measurements where different tilting angles were investigated, this effect was too large to be neglected. For that reason, the flourescence intensity was measured for a defined geometry before and after adjusting the detection unit to a particular tilting angle. The observed decrease in intensity was of the order of less than 10 %. This bleaching was corrected for in the data assuming a linear bleaching during a single measurement using the following model:

$$I_{corr} = I_{measured} \cdot \frac{I_0}{I_{before} - \left(I_{before} - I_{after}\right) \cdot t/T} \qquad (6.15)$$

where I denotes the fluorescence intensity. The subscripts have the following meanings:

corr: ‘corrected’
0: Intensity measured before the first measurement: all dye molecules are still intact
before: Intensity measured before an individual measurement
after: Intensity measured after an individual measurement
T denotes the total time needed for one measurement and t is the time when the individual point is taken.

It is a problem that this correction routine does not account for the fact that the bleaching rate of the molecules is strongly site-dependent as will be explored in section 6.5. For that reason, care must be taken that the bleaching is not too strong in order to obtain significant data.

6.4 Results

In this section, the sample is optically characterised first with a reflectivity measurement. Next, the measurements of the fluorescence intensity with the detector placed in the plane of incidence are presented. These results are compared to model calculations on the basis of the parameters as obtained from the reflectivity measurement. To obtain a complete picture, the transition from the coupled resonances to the free surface plasmons is investigated by detecting fluorescence light leaving the plane of incidence and comparing these measurements again with theory.

6.4.1 Sample characterisation with reflectivity measurements

The basis of the calculations of the local fields that are experienced by the fluorescence molecules is a set of parameters which describes the optical response of the grating: the shape of the grating, the dielectric constant of the gold, the thickness and the refractive index of the polymer film. Reflectivity measurements are best suited to obtain these parameters as described in detail in chapter 3. For a bare gold surface, a single reflectivity measurement would be sufficient to determine all parameters by a least squares fit. The thickness of the polymer film is an additional parameter that has to be determined by comparing the reflectivity data with and without the film.

The reflectivity of the sample was recorded with a set-up as described in chapter 3 in $\Psi = 90°$ geometry before and after spin-coating the polymer film. By the method of least squares, the grating profile as well as the dielectric constant of the gold was determined from the measurement without polymer film. Then, the thickness of the polymer film was determined by introducing this value as a new free parameter and keeping all other parameters fixed. For an idealised sample, the quality of this fit should be as good as without polymer film. In reality, this is not the case and a tolerance of small changes for all parameters again gives a much better correspondence. There may be several reasons for this inconsistency:

- Only 3 Fourier components of the profile were regarded for the fit.
- No effects of sample roughness were taken into account.
- The gold was described as a perfectly homogenous medium.
- The polymer film was assumed to be a layer of constant thickness following precisely the grating profile, an assumption that cannot be entirely true, taking into account the process of spin coating on a non-planar surface.

By comparison of the parameters obtained from the best fit to the data from the bare gold surface to the ones that were obtained with the film, only slight variations are observed. Because the fluorescence experiments are performed on a sample with polymer film, this set of parameters was chosen for the calculations of fluorescence intensities. Their values are given in the figure caption of Fig. 6.8., where calculated and experimental data are shown.

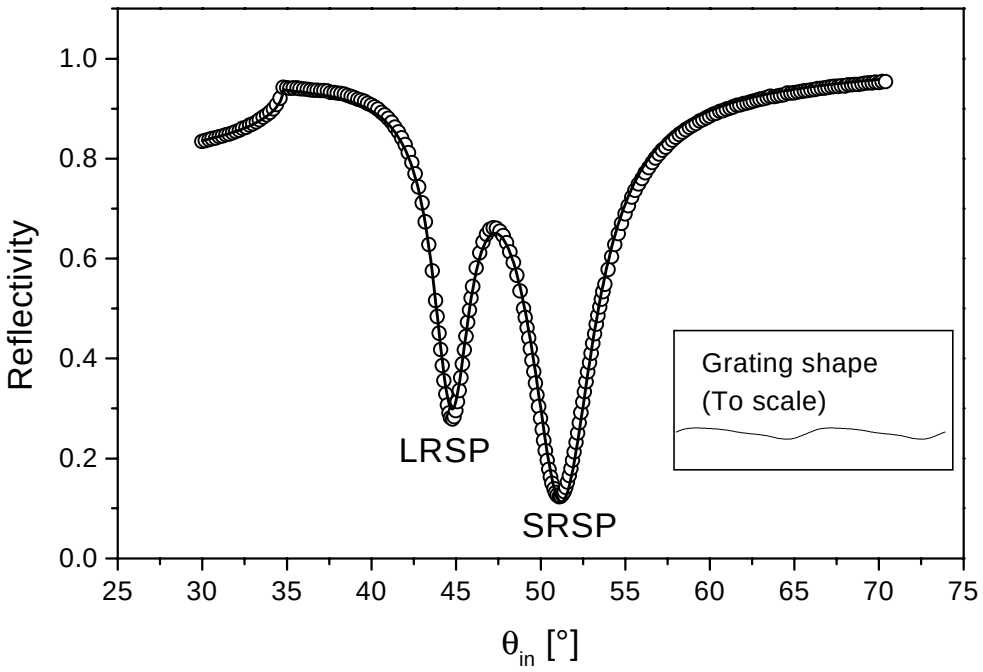

Fig. 6.8: Reflectivity in $\Psi = 90°$ geometry with the incident light (632.8 nm) being TE-polarised. The straight line is a model calculation based on the parameter set: $\Lambda = 770.35$ nm, $A_1 = 25.6$ nm, $A_2 = 7.62$ nm, $\varphi_2 = 25.6°$, $A_3 = 3$ nm, $\varphi_3 = 63°$, $\varepsilon_{Au} = -11.2 + i\,1.17$, Polymer layer with thickness 19.1 nm and dielectric constant $\varepsilon = 2.25$. The grating shape as determined from the fit is shown in the inset.

For the model calculations at a wavelength of $\lambda = 670$ nm, the dielectric constant of the gold was adapted according to the procedure that was already discussed in chapter 4.3.1. An $\varepsilon(\lambda = 670\text{ nm}) = -13.84 + i{\cdot}1.053$ was used for the further analysis.

6.4.2 Fluorescence emission in the plane of incidence

The fluorescence light was measured as a function of θ_{rel} for the angles of incidence $\theta_{ex} = 44.8°$ and $\theta_{ex} = 51°$, with $\Psi_{ex} = 90°$ and $\Psi_{tilt} = 0°$, the data is shown in Fig. 6.9. This is the same excitation geometry as used for the reflectivity scan in Fig. 6.8. From there it can be seen that the two excitation angles θ_{ex} were chosen precisely in the two reflectivity minima, assuring an effective excitation of the two coupled resonances (LRSP, SRSP).

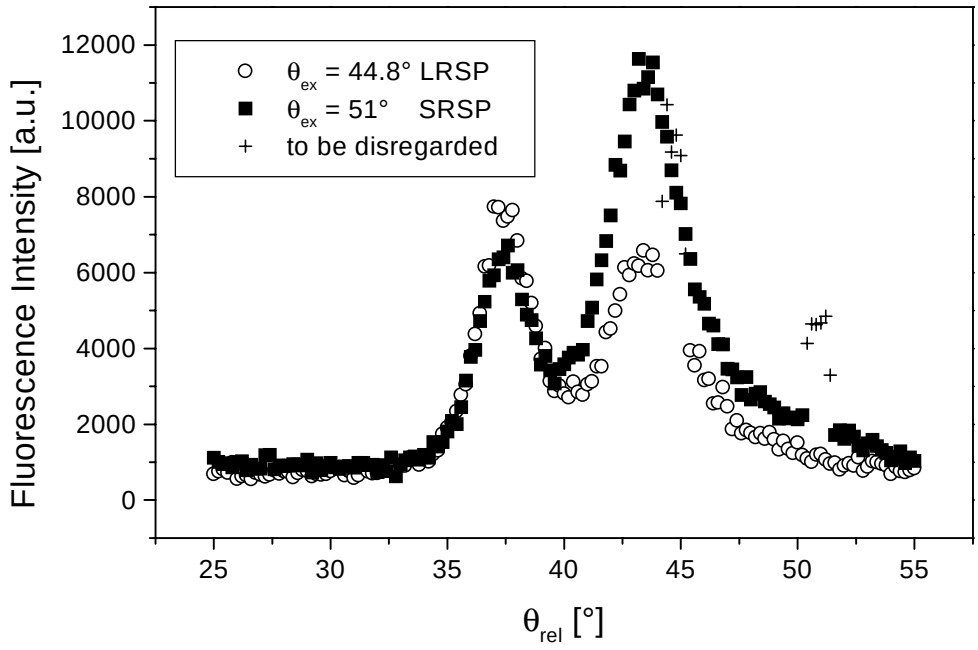

Fig. 6.9: Fluorescence intensity as a function of the emission angle θ_{em} (= θ_{rel}) at Ψ_{em} = 90° for two different excitation angles θ_{ex}. The excitation wavelength equals λ_{ex} = 632.8 nm. When the specular reflection of the incoming beam coincides with the detection axis, there is some undesired stray light reaching the detector. These data points are drawn as crosses and should not be considered for the analysis.

The emitted intensity shows two clear maxima which are attributed to surface resonances corresponding to the emission wavelength of the chomophore (670 nm). They occur at θ_{rel} = 37.5° and θ_{rel} = 43.5°. The positions where mimima are observed in a reflection experiment with the corresponding wavelength λ_{em} = 670 nm (compare the model calculation in Fig. 6.3) coincide well with the positions of these emission peaks. Therefore, they can be attributed to an enhanced emission that is mediated by the two coupled resonances at λ_{em} = 670 nm.

An important observation can be made regarding the relation between the maximum values of the two peaks for the two excitation angles. Excitation of the LRSP (at λ = 632.8 nm) leads to an enhanced fluorescence emission mediated by the LRSP (θ_{rel} = 37.5° at λ = 670 nm). The same holds for the SRSP. The transfer from excitation to fluorescence energy is more effective between coupled resonances of equal type than between different types. This effect can be explained with the concept of the site-dependent variation of the excitation and emission probability as introduced in section 6.1.3.2.

In order to quantify this effect, the ‘Correlation number’ C is defined as

$$C = \frac{I_{LRSP}^{LRSP} \big/ I_{SRSP}^{LRSP}}{I_{LRSP}^{SRSP} \big/ I_{SRSP}^{SRSP}} \qquad (6.16)$$

where I denotes the maximum intensity of the peak as it is read from the plot and the superscript/subscript indicate whether the excitation/emission angle corresponds to the LRSP or SRSP coupled resonance. In the present case (Fig. 6.9) a correlation number of C = 2.12 is found.

Some remarks must be made about the experimental errors.

The final angular resolution of the detector leads to a smearing out both in direction of θ_{rel} (which will broaden the narrower peak at 37°) and in Ψ_{tilt} (which will lead to a generally diminished effect as will be shown in the next section). The finite wavelength resolution of the detector has a similar effect. For these reasons, it can be assumed that the 'real' correlation number is higher than the one that was determined from the experimental data.

Outside the resonance region a significantly higher signal is measured than predicted ba the calculation (compare the following section). This effect may be attributed to scattering effects due to roughness features on the grating surface. This background will again lead to a reduction of the correlation number as found from the measurement. One may eliminate this background by subtracting a constant number from the data, but this doesn't give satisfying results in the region around $\theta_{rel} = 50°$.

It is not meaningful to attempt to quantify all these effects especially the error that is induced by scattering. Therefore, no error is assigned to the measured correlation. It should be kept in mind, though, that it can be assumed that the measured correlation is too low.

6.4.3 Detection in the plane of incidence: model calculations

Calculations based on the two models introduced in section 6.2, 'quickly rotating dipoles' and 'fixed dipoles' were performed. The calculated fluorescence intensities for both models are compared to the measured data in Fig. 6.10. A scaling factor was applied to the calculated data to obtain a better correspondence to the measurement (Note: A scaling factor won't change the correlation as defined in equation (6.16))

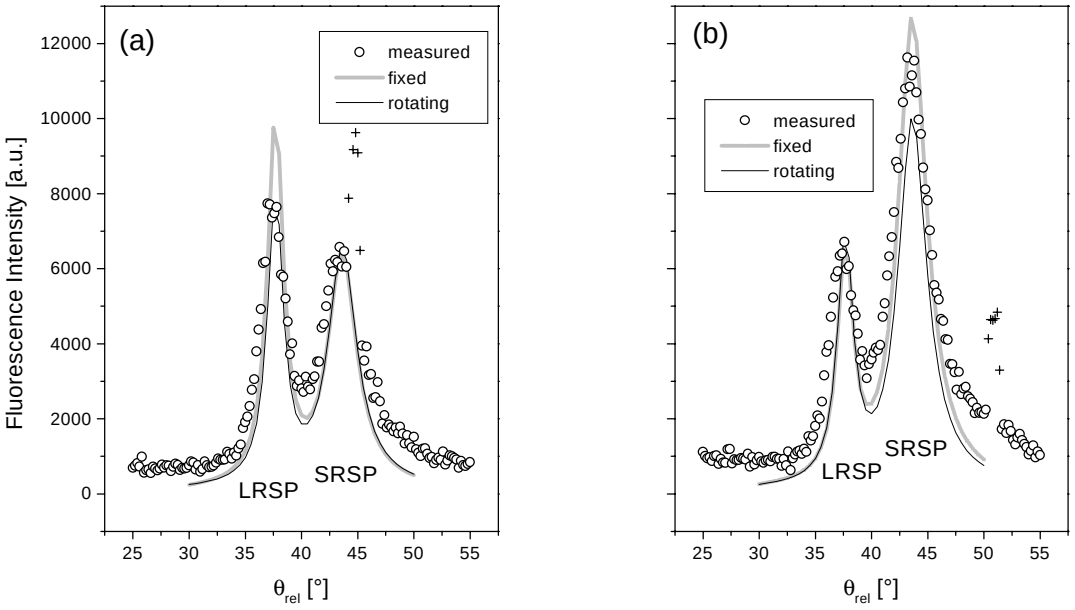

Fig. 6.10: The measured data for (a) $\theta_{ex} = 44.8°$ (excitation with the LRSP) and for (b) $\theta_{ex} = 51°$ (excitation with the SRSP) together with model calculations based on the model of fast rotating dipoles (narrow black line) and fixed dipoles (broad grey line).

Calculations based on both models predict a significant correlation. The correlation number that is found for the rotating dipoles is 1.79, smaller than the one experimentally determined (C = 2.12). The fixed dipoles on the other hand predict a correlation number of 2.93 which is too high. Since the two averaging procedures may be regarded as extreme cases, it is not surprising that neither is able to give a perfect description of the measured data. Furthermore, as was pointed out in chapter 3, the roughness of the sample induces some uncertainties in the grating profile as determined from reflectivity measurements. Therefore, the intensity distributions as determined from the model calculations will have some degree of uncertainty, also.

To conclude, both averaging procedures predict a correlation of the order of magnitude that is observed experimentally. Since all experimental errors lead to a diminished correlation, it can be assumed that the model of quickly rotating dipoles is not applicable for the measurement on this system. Due to the errors in the measurement and in the modelling, a quantitative evaluation is not possible. Still, the approximate agreement between experiment and theory gives good insight into the underlying physics.

6.4.4 Emission outside the plane of incidence

More fluorescence data were recorded with the detector being positioned outside the plane of incidence ($\Psi_{tilt} \neq 0°$, therefore $\Psi_{em} \neq 90°$,). These experiments track the resonance features involved in the outcoupling process in their evolution from coupled resonances (at $\Psi_{tilt} = 0°$) to 'free' surface plasmons for higher Ψ_{tilt}. (compare Fig. 6.3

and Fig. 6.5). It is expected that the correlation number for an outcoupling process which is mediated by free surface plasmons will approach 1 (no correlation) due to the fact that they do not have a field localisation. Fig. 6.11 shows data measured with the detector moved out of the plane of incidence by $\Psi_{tilt} = 1.6°$ and $\Psi_{tilt} = 5.5°$

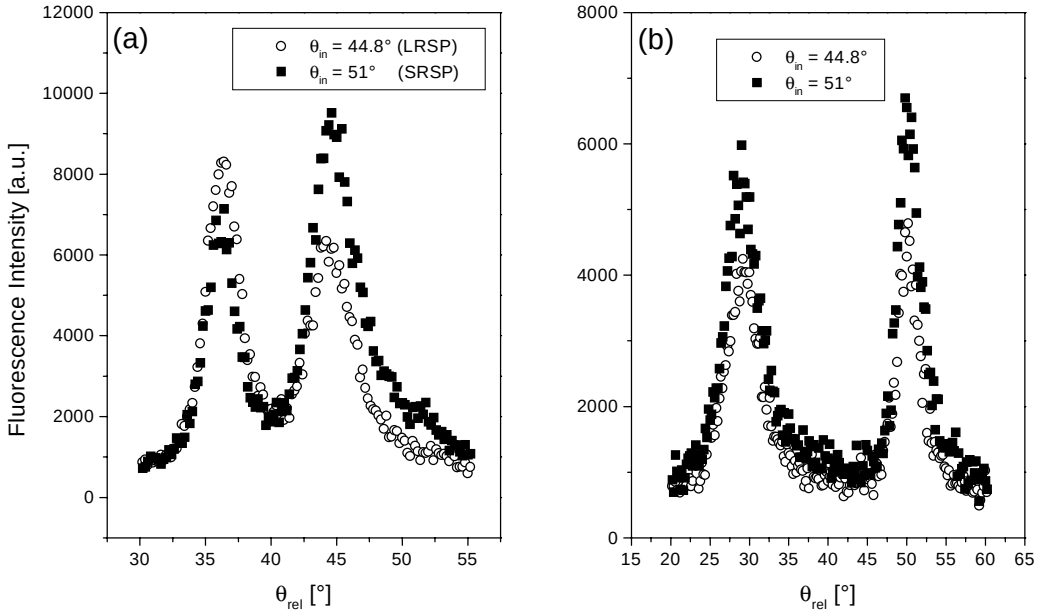

Fig. 6.11: Fluorescence intensity at $\Psi_{tilt} = 1.6°$ (a) and at $\Psi_{tilt} = 5.5°$ (b) for the two different angles of incidence corresponding to the excitation of the LRSP and the SRSP.

The distance between the two peaks increases with increasing Ψ_{tilt} as it is expected from Fig. 6.3, while their mutual coupling weakens. For small tilting angles ($\Psi_{tilt} = 1.6°$) these resonances transition from coupled to free surface plasmons, for $\Psi_{tilt} = 5.5°$, the resonances are some distance from the 'photonic band gap' and can therefore be regarded as free surface plasmons.

It is clearly seen that the difference in shape between the two data sets is still visible for $\Psi_{tilt} = 1.6°$ while at $\Psi_{tilt} = 5.5°$ the two sets of data appear nearly identical up to a constant scaling factor. This is reflected in the correlation number at $\Psi_{em} = 1.6°$ of C = 1.96 which is already diminished from C = 2.12 in the plane of incidence, showing that the field confinement is already diminished. For $\Psi_{em} = 5.5°$ the correlation number is determined as 1.024 which is equal to 1 within the experimental error.

The correlation numbers that were obtained from several out-of-plane measurements, including the two that were just presented are shown in Fig. 6.12. For comparison, correlation numbers that were obtained by model calculations based on the two models are also shown.

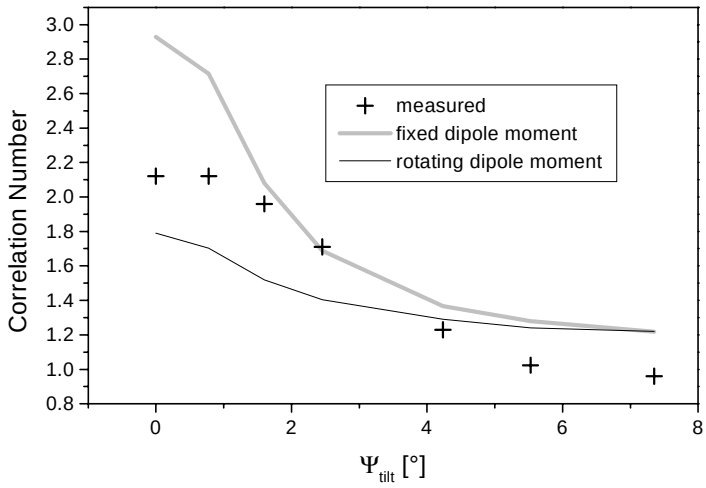

Fig. 6.12: Correlation numbers as a function of the angle relative to the plane of incidence Ψ_{tilt}. Measured data are compared to model calculations.

The measured correlation number shows a maximum when the detector is in the plane of incidence and decreases quickly when the detector is tilted out of the plane of incidence. At $\Psi_{tilt} = 7.35°$ the measured correlation number has reached 1 within the error of the measurement indicating freely propagating surface plasmons.

The model calculations, assuming quickly rotating molecules (thin black line), yield significantly lower values than the ones measured in the plane of incidence, but a measurable correlation for strongly tilted detector axis is predicted which is not found in the measurement.

The modelled correlation number assuming fixed dipole moments (grey line) is tendentiously higher than the measured data. It seems to decay more rapidly in the vicinity of $\Psi_{tilt} = 0$ than in the measurement and there is a finite correlation predicted for $\Psi_{tilt} = 7.35°$ that is not found experimentally.

In conclusion, neither of the averaging procedures is appropriate for a quantitative interpretation of the data. Nevertheless, both describe the reduced correlation upon transition from coupled resonances to freely propagating surface plasmons and predict the range of Ψ_{tilt} where a significant correlation is correctly observed. Although some refinements seem to be necessary, the physical processes underlying the results of the measured fluorescence light which is coupled out with either a coupled resonance or a freely propagating surface plasmon as intermediate step, seem to be well reproduced by the theory.

6.5 Selective bleaching

In the previous section, there was considerable effort put in the elimination of bleaching effects. Nevertheless, the bleaching of chromophores in standing surface plasmon fields

is an interesting phenomenon by itself and will be studied in this section. As an application, a modification of the FRAP (fluorescence recovery after photobleaching) technique [Axe76] will be presented as a possible application and a proof of principle thereof will be given.

6.5.1 Observation of the selective bleaching

The photonic energy that is absorbed by a dye molecule may cause a photochemical reaction which transforms the dye into some non-fluorescent molecule. As a consequence, the fluorescence of a given sample will decrease with time under illumination. Obviously, when the chromophores are exposed to a spatially modulated electrical field pattern as it is generated by coupled surface resonances, the bleaching will mainly occur to the chromophores that are exposed to high field intensities. This will lead to a modulated chromophore density across the grating with the same modulation period as the electrical field, 385 nm in the present case.

The existence of such a modulation can be proved by following the fluorescence intensity as a function of excitation and emission angle with time. Because the bleaching is relatively fast, only the two excitation angles (LRSP: θ_{ex} = 44.8°, SRSP: θ_{ex} = 51°) and two emission angles (LRSP: θ_{em} = 37.5°, SRSP: θ_{em} = 43.5°) are chosen that assure maximum coupling of (incident or emitted) light to the coupled surface resonances. These four intensities are measured while the sample is illuminated under θ_{bleach}. When the θ_{bleach} is chosen to coincide with maximum excitation of the one resonance, the corresponding emission can be measured in situ during the bleaching process. The measurement of the emission excited by the other resonance requires a short interruption of the bleaching process as well as bleaching at a ‘wrong’ excitation angle. Bleaching intervals of 5 minutes were chosen opposed to data acquisition times of 10 seconds per point to minimise the effect of bleaching at a wrong angle. During the time when the goniometer positions were changed, the laser beam was blocked from reaching the sample. Fig. 6.13 shows the four peak intensities for bleaching under θ_{bleach} = 44.8° (excitation of the LRSP) with λ_{ex} = 632.8 nm. It is clearly seen that the decay of $I^{LRSP}{}_{LRSP}$ is the most rapid, followed by $I^{SRSP}{}_{LRSP}$ and $I^{LRSP}{}_{SRSP}$, which are approximately equal. $I^{SRSP}{}_{SRSP}$ exhibits the slowest decay. I denotes the fluorescence intensity, the superscript the excitation and the subscript the emission direction.

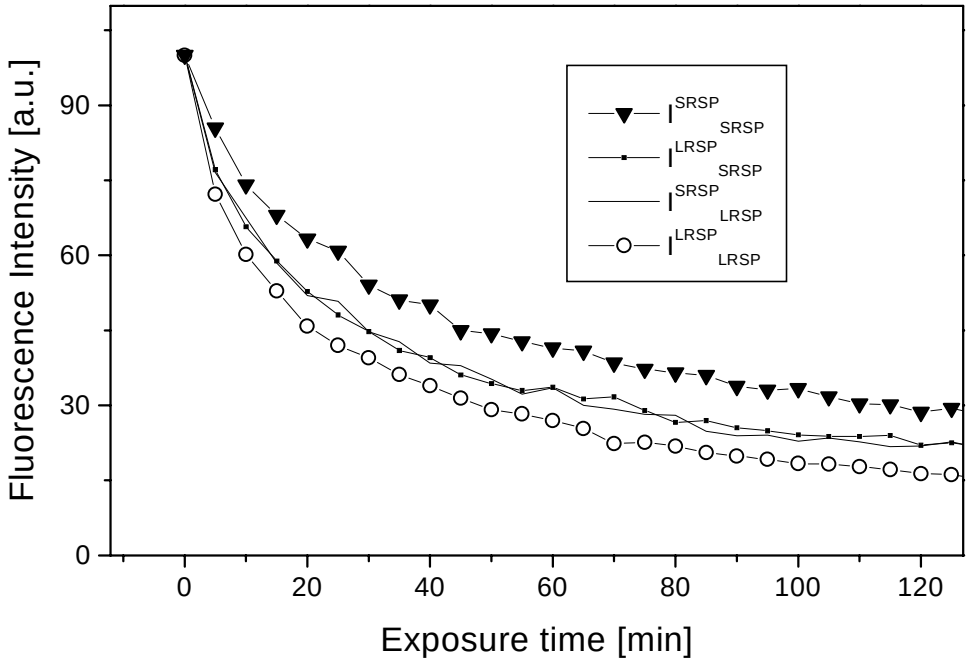

Fig. 6.13: Evolution of the intensities I^{LRSP}_{LRSP}, I^{LRSP}_{SRSP}, I^{SRSP}_{LRSP}, I^{SRSP}_{SRSP}, during illumination in the LRSP. The curves were normalised to a starting value of 100 to allow better comparison.

This behaviour can be explained qualitatively when we consider which molecules are involved in which fluorescence process:

1. I^{LRSP}_{LRSP} mainly involves the molecules in the intensity maxima of the LRSP..

2. I^{SRSP}_{SRSP} mainly involves the molecules in the intensity maxima of the SRSP..

3. I^{LRSP}_{SRSP} and I^{SRSP}_{LRSP} mainly involve the molecules which experience significant field strength of both coupled resonances, this is dirctly in the slopes of the intensity distributions in Fig. 6.5.

Because the bleaching rate is proportional to the local electric field strength, the different bleaching rates that are observed in Fig. 6.13 can be understood with the assumption that the chromophores positioned in the intensity maxima of the LRSP will be most effectively bleached. Indeed, the bleaching beam ‘burns’ a modulation in chromophore density and this effect can be tracked by observation of the fluorescence intensities at the experimental geometries specified above.

6.5.2 A new ‘FRAP’ method

The spatially selective and irreversible bleaching of fluorescing molecules can be used for the study of dynamic processes in thin films. This technique is called ‘Fluorescence Recovery after Photobleaching’ (FRAP) [Axe76]. A high intensity laser is focused on a

surface containing chromophores. Soon, all fluorescing molecules in the focal point are irreversibly bleached. After the bleaching laser is switched off, the fluorescence from this spot is measured as a function of time. Molecules that were outside the spot at the first laser flash are still intact and while they diffuse into the bleached spot, the fluorescence intensity that is detected from there will rise from 0 immediately after the bleaching, ideally back to its original value. The time that is needed for this process depends on the diffusion constant of the chromophores and allows therefore the study of dynamic processes in the film.

Exploiting the effect of selective bleaching that was introduced in the last section, a very similar experiment can be performed. It may offer the possibility to measure systems that are not accessible with conventional FRAP for two reasons:

1. The light cone of a focused laser can be thought of as being composed of plane light waves that form an intensity minimum right at a metal surface due to destructive interference of the incoming and outgoing beams. Manipulation and investigation of fluorescing molecules directly on a metal surface is therefore difficult. In contrast, the coupled resonances on a diffraction grating have their maximum intensity at the surface and are therefore better suited for the investigation of metal-based systems.

2. The average distance x that a molecule diffuses within the time t is given by the diffusion coefficient D [Ger82]:

$$\left\langle x^2 \right\rangle = D \cdot t \qquad (6.17)$$

If small diffusion coefficients are to be measured within reasonable time, the observation of small distances is required. Since the modulation in chromophore density that is produced by coupled modes has a pitch of less that 400 nm, very slow processes can be resolved with this technique.

As a proof of principle, the mobility of Cy5 labelled streptavidin dispersed in a film of Poly(vinylalcohol) is investigated. Fig. 6.14 shows the measured fluorescence intensities $I^{SRSP}{}_{SRSP}$ and $I^{LRSP}{}_{LRSP}$, which exhibit the strongest difference in bleaching rate for a sample that was bleached for 20 minutes at θ_{ex} = 52.6° (SRSP)[10]. As in the previous section, both intensities decrease, this time, $I^{SRSP}{}_{SRSP}$ about twice as fast as $I^{LRSP}{}_{LRSP}$. When the bleaching laser is switched off, only a slow change in intensity is observed which can be attributed to the photobleaching during the measuring process. Then, at t = 55 min, the humidity of the air next to the sample is increased for a few seconds to 100% by placing a sponge with hot water close to the sample.

[10] This measurement was done on a different sample, therefore the angular positions of the excitation / emission maxima are slightly shifted.

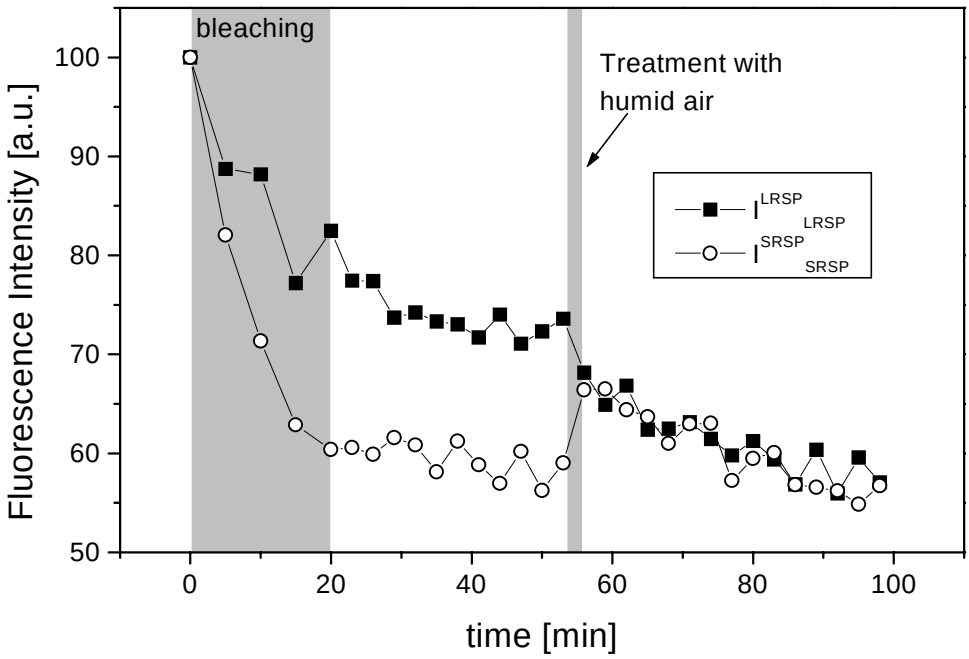

Fig. 6.14: The development of the normalised fluorescence intensity which is due to excitation and emission either mediated by the LRSP (open circles) or the SRSP (full squares). First, the sample was bleached in the SRSP for 20 minutes then, after some time the sample was exposed to humid air for a few seconds.

After this, an increase in $I^{SRSP}{}_{SRSP}$, along with a decrease in $I^{LRSP}{}_{LRSP}$ indicates the redistribution of the dye molecules. Both (normalised) intensities being almost equal at the end shows that the dye molecules are distributed completely random again after the exposure to humidity.

Poly- (vinyl alcohol) is a strongly hydrophilic polymer which takes up water from the surrounding. This swelling causes considerable enhancement of the mobility of the system. This gave the chromophores the mobility to rearrange and form a homogenous distribution again within the polymer layer. By this, it was demonstrated that the redistribution of fluorescent dyes can in principle be tracked by observing the fluorescence intensity which is mediated by coupled resonances in the excitation and the emission processes.

6.6 Conclusion and outlook

It is demonstrated that the localisation of the near field of coupled surface resonances leads to spatially inhomogenous excitation and emission probabilities of fluorescence molecules near the surface. A theoretical model allows a quantitative description of these effects but due to errors both in the model and in the measurement, a quantitative

description is not possible. Outcoupling mediated by free surface plasmons does not show spatial selectivity.

Furthermore, it is shown that the chromophores at the positions of maximum field strength are preferentially bleached. The observation of moisture-induced mobility of chromophores in a thin polymer layer shows that the effect of selective bleaching can be used for the study of diffusion phenomena.

It would be very interesting to do similar measurements with freely rotating chromophores as opposed to fixed ones and check if the theoretically expected reduction of the correlation upon enhanced mobility can be observed. The search for spatial inhomogenities of lifetimes and spectral properties due to coupled surface waves would be another interesting problem.

Some more effort should be made regarding the measurement of diffusion effects. For example, the research on metal based model membranes (compare e. g. [Gyö99]), where either the lipids or proteins could be fluorescence labelled, may benefit from this technique.

7 The polarisation dependence of the coupling to the surface plasmon resonance

7.1 Introduction

The excitation of surface plasmons by light requires the formation of a periodic charge density fluctuation in the metal. As it will be shown in detail later (7.4.1), the electrical field of TE polarised light cannot produce a surface charge on a plane metal surface and on a relief grating in the classical mount. For this reason, coupling to the surface plasmon resonance is only possible with TM polarised light in these geometries. In the general case of grating coupling (conical mount, Ψ arbitrary), it is not straightforward to see which polarisation couples to the surface plasmon resonance. Fig. 7.1 shows the measured reflectivity as a function of the angle of incidence (given by θ and Ψ) for TM and TE polarisation. A definition of the angles that are used here is given in chapter 2. There, the position of the surface plasmon resonance in the θ-Ψ plane was already discussed, this problem is analysed in literature as well [Wat97c]. Here, the focus lies on the polarisation dependence.

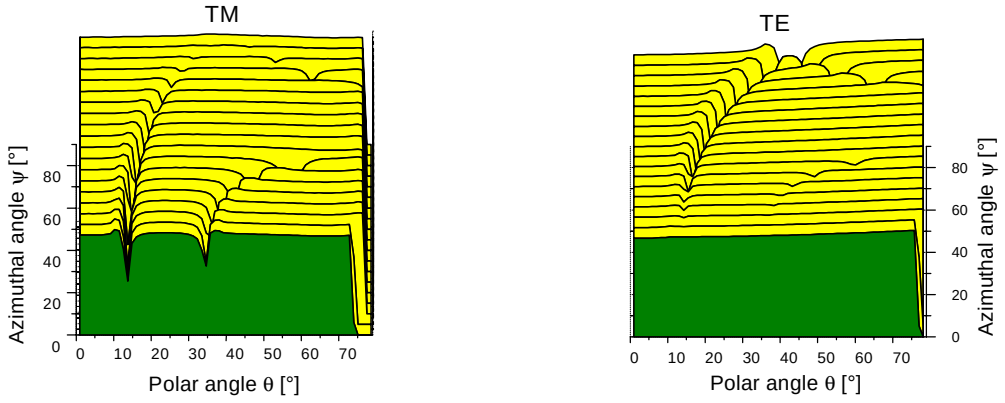

Fig. 7.1: Measured reflectivity of a Λ = 773.6 nm grating for different azimuthal angles. The wavelength of the incident beam was λ = 632.8 nm. The image on the left was recorded with TM polarised light, right with TE polarisation.

While in the classical mount (Ψ = 0°), there are two clear minima visible that are due to coupling to the surface plasmon resonance in +1st and -2nd order for TM polarisation, no minimum is observed for TE as expected. When the azimuthal angle is gradually increased, the coupling strength of TM weakens while coupling becomes possible with TE. At Ψ = 90°, when the plane of incidence is parallel to the grating grooves, from

momentum matching, two resonances are allowed, $+1^{st}$ and -1^{st} order[11]. They are excited by TE-light only. The question that will be treated in more detail in this chapter is: at which polarisation of the incident light do minima appear that are due to coupling to the surface plasmon resonance?

In the next section (7.2), measurements of the surface plasmon resonance for different linear polarisations are presented. These measurements are compared to the corresponding model calculations in section 7.3. Subsequently, some more calculations deal with the case of an almost perfectly conducting metal. As a next step (7.4), the polarisation dependence of surface plasmon coupling is discussed on a geometrical basis. Finally, an analysis of the polarisation of the reflected beam (7.5) stresses the importance of a full analysis of the polarisation state.

7.2 Experimental results

The grating that was investigated with respect to its polarisation dependence was optically characterised. Since exactly this grating served as an example to illustrate the procedure of optical characterisation in chapter 3.3, the results that were obtained there are valid for the following analysis.

As a next step, this grating was investigated with respect to the polarisation-dependence of surface plasmon coupling in the conical mount.

It was already seen in the introduction that in the classical mount, there are no minima in the reflected intensity when the sample is illuminated with TE-polarised light. Similarly, TM-light does not lead to minima in the reflectivity at $\Psi = 90°$. For all other Ψ, both TM and TE do couple to some extent. An arbitrary linear polarisation $\mathbf{p}$ is described as a superposition of a TM and a TE component (Compare Fig 2.4) which have directions that are defined by the unit vectors $\mathbf{p_{TM}}$ and $\mathbf{p_{TE}}$.

$$\mathbf{p} = \cos(\varphi) \cdot \mathbf{p_{TM}} + \sin(\varphi)\mathbf{p_{TE}} \qquad (7.1)$$

with the 'polarisation angle' φ. In Fig. 7.2, the θ-dependent reflectivity is shown for φ varying from 0° to 180° for one example ($\Psi = 79°$) as obtained from a measurement.

[11] To be precise, at $\Psi = 90°$ no free surface plasmons but coupled resonances are observed, but this does not influence the polarisation dependence.

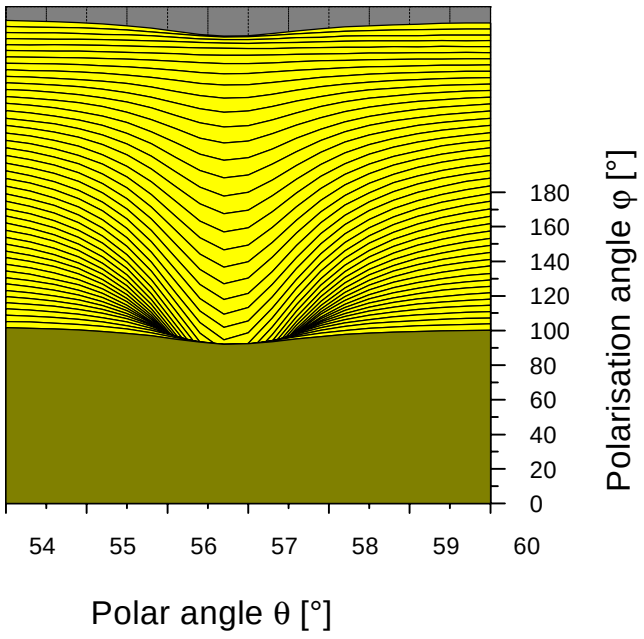

Fig. 7.2: Measured intensity reflected from the grating as a function of φ and θ at Ψ = 79° for light with a wavelength λ = 632.8 nm.

The depth of the minimum strongly depends on the polarisation. For a given φ, the second derivative of the reflectivity with respect to θ in the minimum gives a measure for the coupling strength which is denoted as cs. The second derivative is defined as the expression that is given below in the limit of $\delta \to 0$.

$$cs = \left.\frac{d^2 I}{d^2 \theta}\right|_{\theta=\theta_{\min}} = \lim_{\delta\to 0} \frac{I(\theta_{\min}+\delta) + I(\theta_{\min}-\delta) - 2\cdot I(\theta_{\min})}{\delta^2} \qquad (7.2)$$

For the measured values, cs could only be evaluated approximately at a finite δ which was chosen as 0.3° due to the finite spacing of the measured points and noise in the measurement.

Fig. 7.3 shows the coupling strength as a function of φ together with a least squares fit to a cosine function oscillating between the maximum coupling cs_{max} and the minimum coupling cs_{min} reaching maximum coupling efficiency at some polarisation angle φ_{max}.

$$cs(\varphi) = cs_{\min} + \frac{cs_{\max} - cs_{\min}}{2} + \frac{cs_{\max} - cs_{\min}}{2} \cdot \cos\left(2\cdot(\varphi - \varphi_{\max})\right) \qquad (7.3)$$

As it will be explained in the next section, this functional dependence cs(φ) is expected from theory. Comparison of the fit with the measured data shows a good agreement. In the example given here, a small but finite cs_{min} is found.

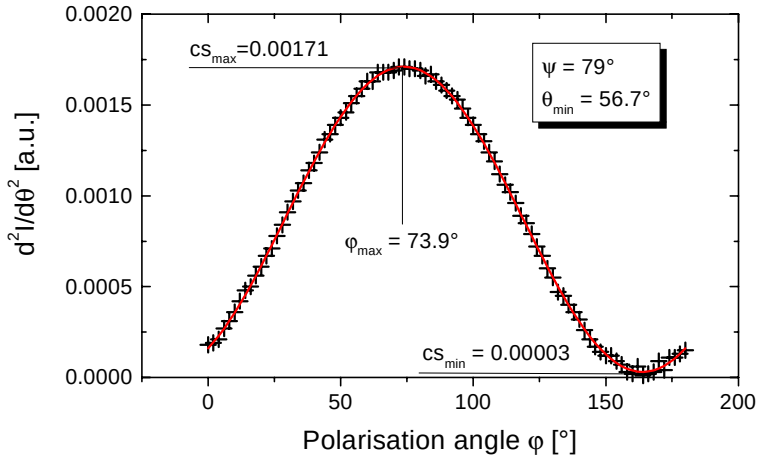

Fig. 7.3: The coupling strength cs is plotted in the minimum of the plasmon resonance (θ = 56.7°) as a function of the polarisation angle φ. The straight line is a fit according to equation (7.3).

7.3 Numerical calculations

7.3.1 Mathematical description of the polarisation

These experimental results are now compared to model calculations. This required the extension of the numerical code (compare chapter 2) to incident light of any polarisation, which means that the incident and outgoing beam are described as a plane wave with the electrical field which is varying in space (**x**) and time t.

$$\mathbf{E}(\mathbf{x},t) = \left(\mathbf{p_{TM}} \cdot E_{TM} + \mathbf{p_{TE}} \cdot E_{TE}\right) \cdot \exp\left(i \cdot \left(\mathbf{k} \cdot \mathbf{x} - \omega \cdot t\right)\right) \qquad (7.4)$$

where **k** is the wavevector. The unit vectors $\mathbf{p_{TM}}$ and $\mathbf{p_{TE}}$ are describing the directions of the fundamental polarisations, the corresponding amplitudes of the electrical field are labelled E_{TM} and E_{TE}. In the most general case of elliptical polarisation, these amplitudes will take complex values, for linear polarisation they can be chosen as real numbers and may be expressed by the polarisation angle φ (compare with equation (7.1)). It is convenient to define a two-dimensional vector $\mathbf{E_0}$ which describes the polarisation state and intensity of the light,

$$\mathbf{E_0} = \begin{pmatrix} E_{TM} \\ E_{TE} \end{pmatrix} = \begin{pmatrix} E_0 \cdot \cos(\varphi) \\ E_0 \cdot \sin(\varphi) \end{pmatrix} \qquad (7.5)$$

where E_0 is the magnitude of the electrical field vector. This representation is used to describe both the incoming and the outgoing beam. Since the response of the optical system under investigation is assumed to be linear, the connection between incoming and outgoing beam is given by a complex 2-dimensional matrix.

$$\mathbf{E}_{\mathbf{0}}^{\mathbf{out}} = \begin{pmatrix} M_{TM}^{TM} & M_{TE}^{TM} \\ M_{TM}^{TE} & M_{TE}^{TE} \end{pmatrix} \cdot \mathbf{E}_{\mathbf{0}}^{\mathbf{in}} \qquad (7.6)$$

At this point it can be shown that the fitting function (7.3) was the appropriate choice. First it is important to note that the dependence of the reflected intensity on the (linear) polarisation angle of the incoming beam will always be sinusoidal in shape because:

$$\begin{aligned} I^{out}(\varphi) = \left|\mathbf{E}_{\mathbf{0}}^{\mathbf{out}}(\varphi)\right|^2 &= E_0 \cdot \left|\left(M_{TM}^{TM} \cdot \cos(\varphi)\right) + \left(M_{TE}^{TM} \cdot \sin(\varphi)\right)\right|^2 + \\ &\quad E_0 \cdot \left|\left(M_{TM}^{TM} \cdot \cos(\varphi)\right) + \left(M_{TE}^{TM} \cdot \sin(\varphi)\right)\right|^2 \qquad (7.7) \\ &= A \cdot \cos(\varphi)^2 + B \cdot \sin(\varphi)^2 + C \cdot \sin(\varphi) \cdot \cos(\varphi) \end{aligned}$$

with some coefficients A, B, C. Obviously, this expression is a harmonic oscillation with twice the period of φ with some offset and some phase shift. The coupling strength cs as defined in (7.2) is a linear combination of intensities and has therefore the same sinusoidal form. As a consequence, φ_{max}, cs_{min} and cs_{max} are sufficient to describe the polarisation dependence.

Some care must be taken with the appropriate chirality of the co-ordinate systems that are defined by the polarisation vectors and the propagation direction of the beam. Here, ($\mathbf{p_{TM}}$, $\mathbf{p_{TE}}$, $\mathbf{k}$) are chosen as right handed (compare with Fig. 2.4)[12]

Upon reflection on plane interfaces, by definition, the projection of the electrical field vector on the reflecting plane for TM-light has a phase jump of 180° while there is no phase jump for TE-light (compare e. g. [Jac83]). This convention preserves the chirality of the light beam upon reflection.

With the modelling program ‘oblique’, the matrix elements as defined in equation (7.6) were determined for the appropriate angles of incidence (θ, Ψ). This allowed to determine the polarisation dependent coupling strength cs(φ) according to equation (7.2) from model calculations.

7.3.2 Comparison between theory and experiment

The experimental procedure that was described in section 7.2 was repeated for several azimuthal angles and a fitting as described above allowed the experimental determination of φ_{max}, cs_{min} and cs_{max}. The corresponding numerical calculations for the grating under investigation were also performed.

The values of φ_{max} as determined from experiment are compared to the modelled results in Fig. 7.4.

[12] For the modelling, it was important to transform the vectors because in the original code ‘oblique’ the chirality is just inversed.

For $\Psi > 70°$, excitation of surface plasmons is possible in two different diffracted orders, $+1^{st}$ and -1^{st} (compare Fig. 7.1), but at different polar angles which is not visible in this plot because the implicit θ-dependence cannot be plotted in 2 dimensions. The polarisation dependent coupling to the surface plasmon resonance in -2^{nd} order is not shown. It can be seen in the plot that the model calculations are well suited to describe the measurement.

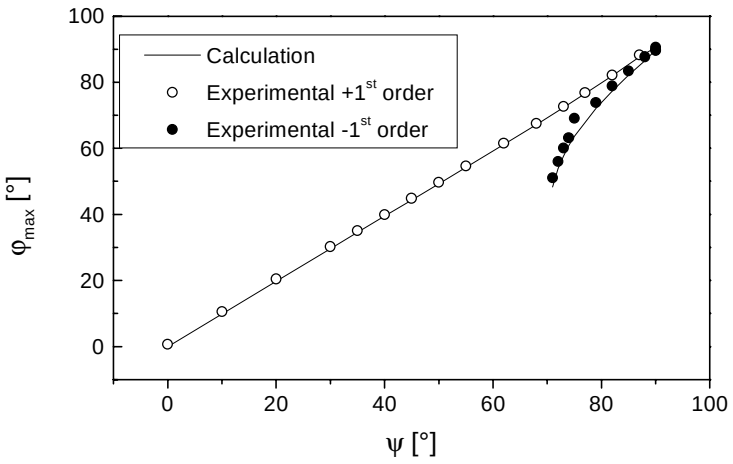

Fig. 7.4: The polarisation angle of maximum coupling φ_{max} for the resonances that are found in the reflectivity of light with $\lambda = 632.8$ nm on the grating under investigation.

The next parameter of interest is the strength of the polarisation dependence, which is reflected in the ratio c_{min}/c_{max}. This number will approach zero if there is a (linear) polarisation where no surface plasmon coupling occurs and approaches 1 if there is no polarisation dependence of the coupling strength. This number was determined from model calculations and from the experiment. The results are compared in Fig. 7.5. For all possible coupling geometries where the $+1^{st}$ diffracted order is responsible for the coupling to the surface plasmon, c_{min}/c_{max} is very small in the numerical modelling and the variations in the measured values are due to experimental errors. For coupling in -1^{st} order, c_{min}/c_{max} increases significantly when θ approaches 90° ($\Psi \rightarrow 70°$).

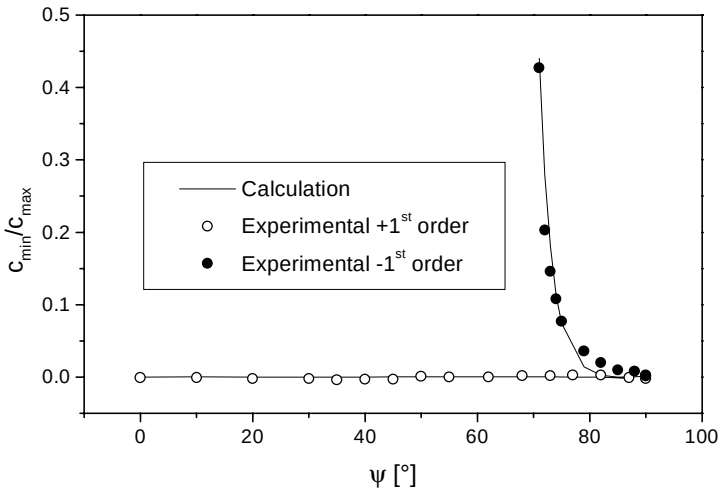

Fig. 7.5: The value of c_{min}/c_{max} in calculation and experiment. The open circles correspond to coupling in $+1^{st}$ order, the full circles to -1^{st} order. The wavelength of the incident light is $\lambda = 632.8$ nm.

These results show conclusively that the modelling routine is capable to describe the polarisation dependence of surface plasmon excitation in good agreement with nature.

7.3.3 Asymptotic behaviour

In order to find out if there is some general principle underlying the polarisation dependence, more model calculations were performed assuming a very shallow grating ($A_1 = 1$ nm) with different pitch Λ on an almost ideal metal ($\varepsilon = -100 + i\ 0.1$). The following observations were made in the model calculations:

1. For an ideal metal, c_{min}/c_{max} approaches 0. That implies that in this case there is a linear polarisation state that doesn't show a surface plasmon minimum in its reflectivity.

2. The polarisation angle of optimum coupling φ_{max} depends only on the reflection geometry (θ, Ψ) and it is completely independent from the coupling order[13].

This is surprising at first sight for the following reason: Surface plasmons that are coupled in different order are described by different in-plane wavevectors or 'propagation directions'. These different wavevectors will lead to different electromagnetic field distributions as it can be concluded from equation (2.5). Nevertheless, maximum coupling to plasmons in all orders occurs with the same field distribution expressed by the same linear polarisation of the incident beam

3. There is an analytical equation that describes $\varphi_{max}(\theta, \psi)$ which has been found by analysing the model calculations:

[13] For any combination of θ, Ψ coupling in any order can be achieved by choosing the appropriate grating pitch.

$$\tan(\varphi_{max}) = \tan(\Psi) \cdot \cos(\theta) \qquad (7.8)$$

In Fig. 7.6, $\varphi_{max}(\theta, \Psi)$ is plotted as obtained from numerical calculations together with the result that is obtained analytically. The small deviations of the real metal grating from the ideal case are due to the fact that gold is not a perfectly conducting metal (finite ε) and that the grating under investigation has a finite amplitude.

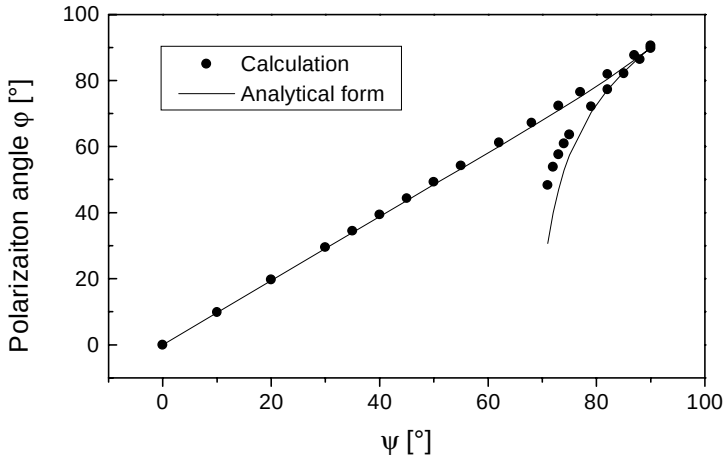

Fig. 7.6: Ψ-dependent φ_{max} as obtained with the analytical form (7.8) in comparison to the results of the numerical calculation (λ = 632.8 nm).

7.4 Geometrical discussion

In this section, an attempt is made to develop a geometrical explanation for the results that were found in the previous subsection, especially equation (7.8). First, an explanation for the polarisation dependence in prism coupling and in grating coupling in the classical mount is given. Then, the geometrical interpretations that are found in literature [Vei95], [Fer93], [Kit96b] are critically reviewed on the basis of a vectorial representation of the experimental geometry that is defined first.

7.4.1 Easy geometries

Excitation of the surface plasmon resonance requires the formation of a modulation in charge density. When a plane electromagnetic wave falls on a grating in the classical mount, the electrical field is parallel to the grating grooves for TE polarisation as shown in Fig. 7.7. No charge density oscillation may be formed due to this field because the charges are moved along lines formed of equivalent points of the grating surface which are exposed to the same time-dependent electrical field. Therefore, for any volume element, the number of electrons leaving the volume equals the number of entering electrons.

On a plane metal surface, the same argument can be applied. In agreement with the well established experimental findings (Kretschmann- and Otto-configuration, compare chapter 2.4), surface plasmon excitation on a planar multilayered system is only possible with TM polarised light.

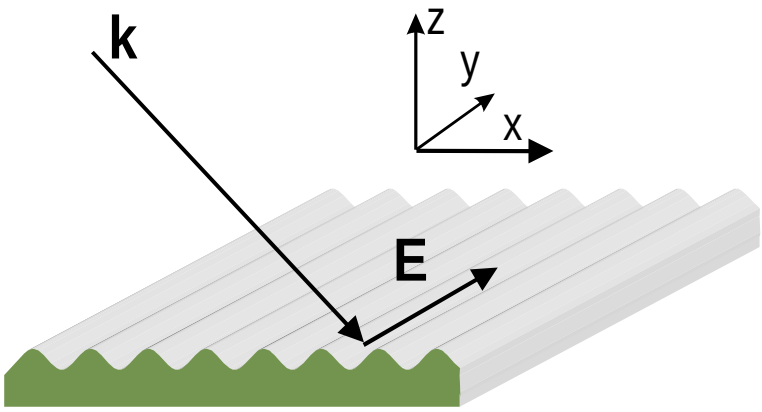

Fig. 7.7: The electrical field of a TE-polarised light beam in the classical mount.

7.4.2 Definition of the geometry

The definitions that were presented graphically in Fig. 2.4 are now described in a vectorial representation. The Cartesian co-ordinate system that is chosen as a basis for the description of the problem is right handed and has its x-axis parallel to the reciprocal grating vector and its y-axis parallel to the grating grooves. The z-axis is normal to the sample surface and is pointing into the dielectric. So, the reciprocal grating vector $\mathbf{k_g}$ equals:

$$\mathbf{k_g} = \frac{2 \cdot \pi}{\Lambda} \cdot \begin{pmatrix} 1 \\ 0 \\ 0 \end{pmatrix} \qquad (7.9)$$

The azimuthal angle Ψ is defined as the counterclockwise rotation of the projection of the plane of incidence onto the sample surface[14], starting with 0 when the reciprocal grating vector lies in the plane of incidence. The wavevector of the incoming beam, $\mathbf{k_i}$, expressed in terms of angles equals therefore

$$\mathbf{k_i} = k_0 \cdot \begin{pmatrix} \sin(\theta) \cdot \cos(\psi) \\ \sin(\theta) \cdot \sin(\psi) \\ -\cos(\theta) \end{pmatrix} \qquad (7.10)$$

where k_0 is the modulus which is fixed by the dispersion relation of light in the dielectric. The linear polarisation of the incoming beam is expressed as the superposition of TM and TE polarisation, where the polarisation vector $\mathbf{p_{TE}}$ must be

[14] In the experiment, this is realised by a clockwise rotation of the grating around its normal.

orthogonal to the plane of incidence which is spanned by $\mathbf{k_i}$ and the surface normal and can therefore be calculated as a vector product

$$\mathbf{p_{TE}} \propto \mathbf{k_i} \times \begin{pmatrix} 0 \\ 0 \\ 1 \end{pmatrix} \propto \begin{pmatrix} \sin(\psi) \\ -\cos(\psi) \\ 0 \end{pmatrix} \qquad (7.11)$$

Normalisation constants are omitted because they are of no significance for the further analysis. The direction of the electrical field for TM polarisation must be orthogonal to the incident beam and the polarisation vector $\mathbf{p_{TE}}$.

$$\mathbf{p_{TM}} \propto \mathbf{p_{TE}} \times \mathbf{k_i} \propto \begin{pmatrix} \cos(\psi)\cdot\cos(\theta) \\ \sin(\psi)\cdot\cos(\theta) \\ \sin(\theta) \end{pmatrix} \qquad (7.12)$$

7.4.3 Geometrical interpretation

Some investigations of the polarisation (φ-) dependence of the coupling to the surface plasmon resonance in the conical mount are found in literature. They are neither consistent with each other nor do they satisfactorily describe the experimental findings that were presented in the previous chapter.

Fernandez-Horn [Fer93] and Veith [Vei95] claim that maximum coupling requires Ψ = φ. This interpretation is clearly wrong as it can be easily verified from equation (7.8) as well as in Fig. 7.4.

Kitson et al. [Kit96b] state that ‘At a general value of Φ (which is the azimuthal angle, Ψ in the notation that is used here) it is only the component of the photon E-field that is in the plane defined by the substrate normal and the grating vector that may couple resonantly to the SPPs (surface plasmon polaritons)’.

One may assume that all components of the electrical field in this plane couple equally well. In this case, the prerequisite for maximum coupling would be

$$\mathbf{p}\cdot\begin{pmatrix} 0 \\ 1 \\ 0 \end{pmatrix} = 0 \qquad (7.13)$$

which yields when (7.9), (7.10) and (7.11) are plugged in

$$\tan(\varphi_{max}) = \tan(\Psi)\cdot\cos(\theta) \qquad (7.14)$$

which is in agreement with the result that was obtained by measurement and numerical modelling.

But there are two major drawbacks of this model. Firstly, there is in general for any φ, a not-vanishing component of the electrical field in this plane because the plane of

possible polarisations and the plane spanned by the reciprocal grating vector and the surface normal are in general not orthogonal. Nevertheless there is a polarisation that does not show a surface plasmon related minimum for an ideal metal (c_{min}/c_{max} does vanish completely).

The second problem concerns the assumption that the electrical field couples with equal strength no matter how it is oriented in the plane spanned by the reciprocal grating vector and the surface normal.

In this plane, either fields parallel to the reciprocal grating vector (x-axis) or parallel to the surface normal (z-axis) may exist. It is not clear why these two components should have the same power to excite charge density oscillations.

Kitson et al. [Kit96b] assume that '[...] such an E-field has a component normal to the local surface allowing it to couple to the surface charge oscillation that constitutes an SPP'. This point of view does not yield an equally effective excitation of a charge density oscillation for all orientations of the E-field inside the plane spanned by the x- and z-axis as it is shown now. A charge ρ that is proportional to the normal component of the incident electrical field can be calculated for a relief grating which is described as a function z(x) by expressing the local normal vector of the surface in terms of the function which is describing the surface.

$$\rho(x) \propto \mathbf{n} \cdot \mathbf{E} = \frac{1}{\sqrt{\left[z'(x)\right]^2 + 1}} \begin{pmatrix} -z'(x) \\ 0 \\ 1 \end{pmatrix} \cdot \mathbf{E} \qquad (7.15)$$

For a very weakly corrugated grating, this function can be expanded in a Taylor series with respect to z'(x):

$$\rho \propto \begin{pmatrix} -z'(x) + O\left(\left[z'(x)\right]^2\right) \\ 0 \\ 1 - \frac{1}{2} \cdot \left[z'(x)\right]^2 + O\left(\left[z'(x)\right]^3\right) \end{pmatrix} \cdot \mathbf{E} \qquad (7.16)$$

If a very shallow sinusoidal grating is considered, only the x-component of the electrical field possesses a not-vanishing linear term and does therefore lead to a significant charge density oscillation that has the appropriate spatial frequency to excite a surface plasmon. So, this model is not able to explain an equally good coupling for electrical fields in x- and z-direction. Instead, there would be a polarisation that does not couple at all to the surface plasmon resonance, the one that is orthogonal to $\mathbf{k_g}$ (x-axis). With the aid of equations (7.4), (7.11) and (7.12) the corresponding polarisation of minimum coupling can be calculated.

$$\vec{E} \cdot \begin{pmatrix} 1 \\ 0 \\ 0 \end{pmatrix} = 0 \quad \Rightarrow \quad E_0 \cdot \left(-\cos(\psi) \cdot \cos(\theta) \cdot \cos(\varphi_{\min}) - \sin(\varphi_{\min}) \cdot \sin(\psi)\right) = 0 \qquad (7.17)$$

From this, with the prerequisite that the φ-dependence is sinusoidal ($\varphi_{min} = \varphi_{max} + 90$), the polarisation of maximum coupling is obtained,

$$\tan(\varphi_{max}) = \frac{\tan(\Psi)}{\cos(\theta)} \qquad (7.18)$$

which is not in agreement with equation (7.8).

It must be concluded that the initial assumption that only a local normal component of the electrical field may produce a charge density oscillation is wrong. Instead, a locally varying tangential component which is parallel to the reciprocal grating vector $\mathbf{k_g}$ may produce a surface charge as well. For a satisfying physical interpretation of the polarisation dependence of surface plasmon coupling, the coherent superposition of both of these mechanisms must be taken into account which makes the problem inaccessible to an easy intuitive interpretation.

So, finally only a heuristic geometrical interpretation is given that describes the experimental findings but is not based on accurate physical arguments:

'Whenever the projection of the electrical field vector onto the grating grooves (y-axis) reaches a maximum, no surface plasmon related minimum is observed on an ideal metal.'

It should be noted that the polarisation that does couple best coincides with the $E_\perp$ polarisation which was introduced in a theoretical paper by Li [Li94].

7.5 Elliptical polarisation

It is well known that the full information about a monochromatic plane light wave includes its polarisation state. A detailed description of the mathematical and experimental treatment of elliptically polarised light is found in many textbooks, [e.g. Col93].

In the previous sections, only linearly polarised light was considered as excitation and it was always the full intensity of the reflected beam that was detected. Here, as a remark, the effect of a detection that is polarisation selective is investigated. In Fig. 7.8, it is demonstrated that a missing minimum in the total intensity of the reflected beam does not necessarily imply that there is no interaction between the incident beam and the surface plasmon resonance. When the TM and the TE-polarised component of the reflected beam are measured separately, resonances are observed in the two individual intensities which are just mutually inverse so that they cancel each other when the sum of the two orthogonal components (full intensity) is measured.

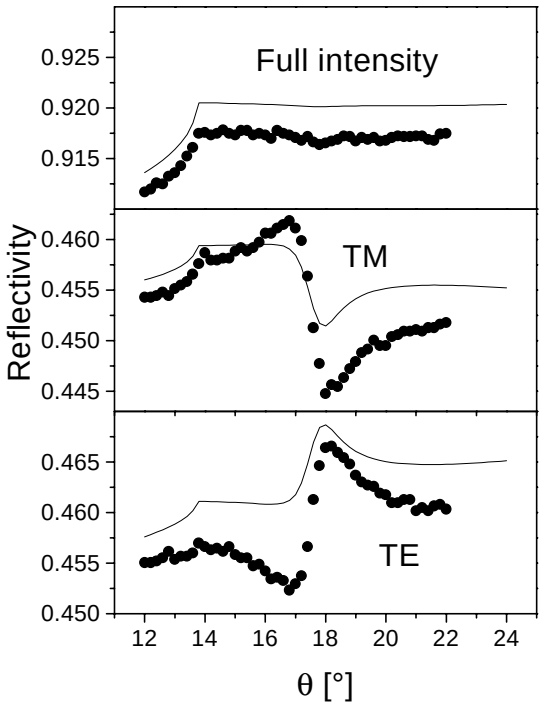

Fig. 7.8: Normalised intensity for $\psi = 45°$, $\varphi = -45°$. The first graph shows the full reflected intensity while the other two were recorded with a polariser in the reflected beam with the orientation as indicated in the graph. The line shows the corresponding model calculation ($\lambda = 632.8$ nm)

It is observed that although the excitation of the surface plasmon resonance has no effect on the total reflected intensity, care must be taken with the statement that there is 'no coupling to the surface plasmon resonance'. When the polarisation state of the outgoing beam is investigated, it is seen that there is still some interaction of the incident light with the surface plasmon. The missing plasmon-related minimum must be regarded as an interference effect and cannot be simply explained by regarding the ability of the incident beam to produce a surface charge.

By some more model calculations, the limit of a perfect metal was investigated again. It turns out that in this limit the resonances in the individual polarisations will vanish.

7.6 Conclusion

In this chapter, the influence of the linear polarisation of the incident beam on the ability to excite the surface plasmon resonance on a metal grating was investigated. The depth of the minimum in the total intensity of the reflected beam was taken as a measure of the coupling strength. Good agreement was found between experiment and numerical modelling with respect to the polarisation where the resonance minimum is deepest and to the finite 'minimum coupling' c_{min}/c_{max}. For an ideal metal with a very shallow modulation, it was found in a set of model calculations that there is a linear polarisation which does not show any reflectivity minimum due to coupling to the surface plasmon

and an analytical equation for this polarisation was found which is only dependent on the polar angle θ and the azimuthal angle Ψ. Approaches to the problem that are found in literature do not give an appropriate description of the experimental findings. Instead, an alternative heuristic interpretation is proposed. An analysis of the two orthogonal polarisations of the light reflected from a real metal grating shows that there may be some interaction with the surface plasmon resonance even if no minimum in the total reflected light intensity is visible.

8 About thin film sensing

8.1 Introduction

The wavevector of the surface plasmon resonance is altered by a thin dielectric film on the metal surface. This effect has been applied to the investigation of thin films by Gordon et al. [Gor77] for the first time. With this ‘surface plasmon spectroscopy’, the detection and investigation of dielectric films in the Angstrom level on metal surfaces is easily possible. Today, this technique has become a standard method in biochemistry. Commercial surface plasmon spectrometers are available from several different companies (Pharmacia, BioTul and others). Mostly, prism coupling is used for sensing due to several reasons:

- The optical response of a flat multilayer system can easily be calculated with the transfer matrix method (compare chapter 2).
- In in-situ investigations of chemical reactions on the metal surface, usually some solution will be present on top of the metal. By prism coupling in Kretschmann-configuration (compare chapter 2), the light beam that excites the surface plasmon does not propagate through this solution and is therefore insensitive to perturbations that may be introduced by stirring or by the addition of light-absorbing species. The only interaction of the light with the solution on top of the surface that is to be probed is via the evanescent field of the surface plasmon.
- A flat gold surface is a well defined environment for the chemical reactions that are to be investigated.

Nevertheless there are certain cases where the excitation of the surface plasmon with an optical grating is favourable. When the appropriate pitch of the grating is chosen, the surface plasmon resonance is observed only a few degrees off from normal incidence. This was used by Kleideiter [Kle99, Kle00] to investigate thin films under high hydrostatic pressure through a very small and thick window as it is necessary for the stability of the set-up. Other examples where prism coupling is impossible and therefore grating coupling is the only solution to obtain informations about dielectric films on the metal surface are investigations on liquids with a high refractive index or measurements where a substrate material must be used that does not have the required optical properties for prism coupling (like simultaneous investigation of optical and rheological properties of a thin film on a quartz microbalance).

In this chapter, it is demonstrated that grating coupling can be used to investigate reactions on metal surfaces. First (8.2), an example for a measurement on a gold grating is given which proofs the applicability of gratings for sensor purposes. The main focus of this chapter lies on section 8.3 where the evaluation of the measured data is

described. First, an evaluation procedure which is based on the precise mathematical treatment of the corrugated metal surface is presented. Then, a much simpler evaluation is proposed as an alternative and its applicability is demonstrated.

8.2 Experimental

8.2.1 Experimental set-up

In practice, one is usually interested in dielectric films on metal surfaces that are exposed to a solvent environment containing molecules that build or modify the film. Examples are self assembled monolayers of thiol compounds [Woh99] and the fusion of lipid vesicles on pre-treated gold surfaces [Sch98]. In Fig. 8.1, a cuvette which can be used for such experiments with a diffraction grating is shown. A laser beam passes through a glass slide and the solution under investigation. It is reflected on the grating, passes through the solution and the glass again and finally reaches a detector. The cuvette, being mounted on an optical set-up as described in chapter 3, allows for the variation of the polar angle of incidence and the measurement of the reflected intensity in a θ / 2θ geometry (tracking of the reflected beam with the detector).

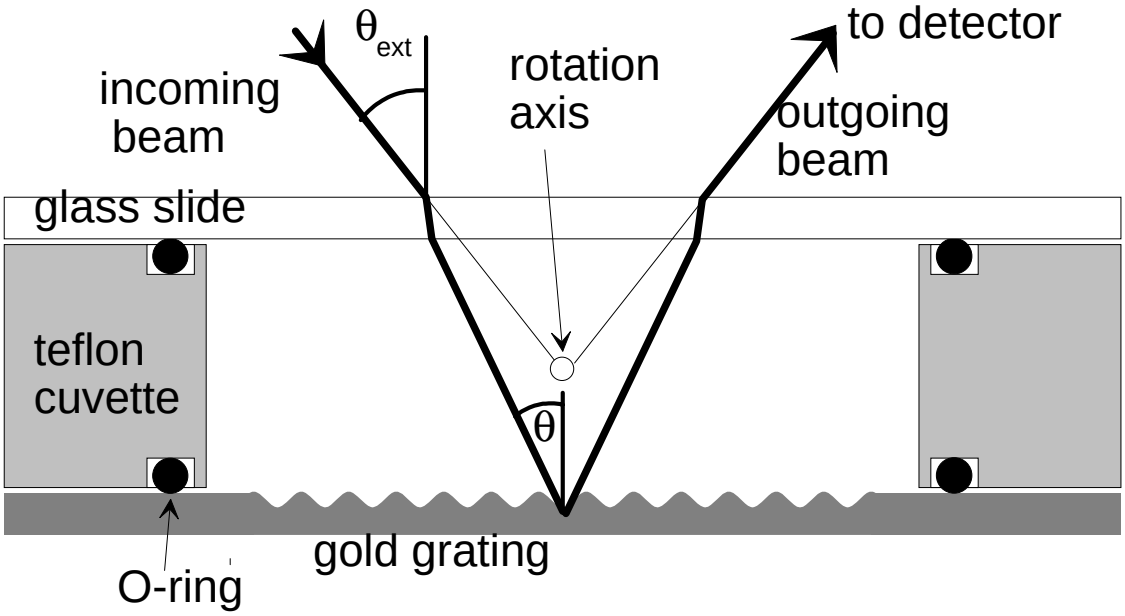

Fig. 8.1: Sketch of a cuvette for surface plasmon spectroscopy with an optical grating.

Due to the different refractive indices of air and the liquid in the cuvette, the polar angle of the reflection on the gold-liquid interface θ is not equal to the one in air, θ_{ext} which is fixed externally with the goniometer. Snellius' law yields in this case

$$\sin(\theta_{ext}) = n_s \cdot \sin(\theta) \qquad (8.1)$$

with the refractive index of the solvent, n_s. It is favourable to use a glass slide as cover that has a refractive index which is as close as possible to n_s in order to avoid

interference problems. Cuvette designs that are quite different from the one presented in Fig. 8.1 are in use for special purposes. A feature which is common to all the designs is that the light has to pass through the cover glass and the solvent before and after reflection on the metal.

8.2.2 Investigation of a thin film

The reliability of a surface plasmon spectrometer which uses an optical grating to couple the incident light to the surface plasmon resonance is demonstrated in this and the following sections. The well studied[15] reaction of octadecanethiol ($SH\text{-}(CH_2)_{17}\text{-}CH_3$) with a gold surface serves as an example. This compound forms a monolayer which is bound covalently to the surface. Fig. 8.2 shows the reflected intensity from a gold grating before and after the formation of a thiol-monolayer. This process was tracked by recording the intensity of the reflected beam at a fixed polar angle ($\theta = 7.5°$). Since this is in the almost linear slope of the resonance, it allows for the on-line observation of a shift of the resonance curve (kinetic mode). Fig. 8.3 shows the reaction kinetics while the following experimental procedure was used to form a monolayer of the thiol compound.

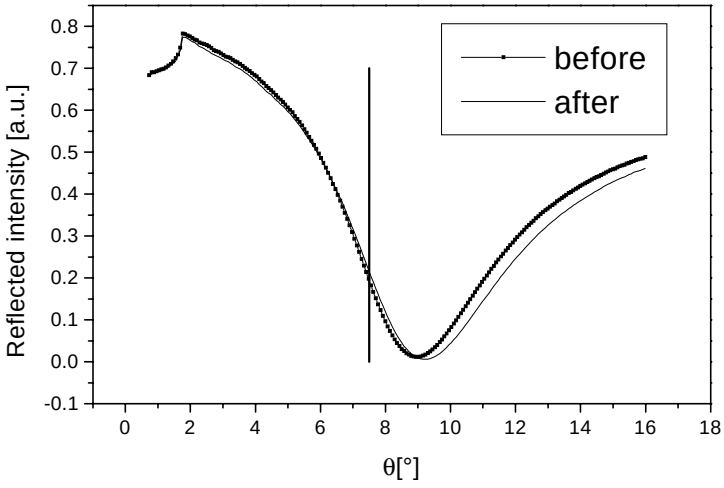

Fig. 8.2: θ-dependent reflectivity of a gold grating before and after the self-assembly of octadecanethiol which was dissolved in ethanol. The angle where the intensity was recorded during the self-assembly ($\theta = 7.5°$) is indicated with a straight line.

The cuvette volume was filled with pure ethanol, subsequently it was rinsed twice with pure ethanol to check the stability of the system. In the kinetic curve, some perturbation due to the liquid exchange are visible but the system recovers within a few seconds. It can be concluded that no artefacts are introduced by the rinsing procedure.

[15] An overview over this topic can be found for example in the book of Ulman [Ulm91].

Then, the cuvette was filled with a solution of the thiol in ethanol (5×10^{-4} mol/l). A steep rise in intensity shows the formation of a dielectric film in the self-assembly process.

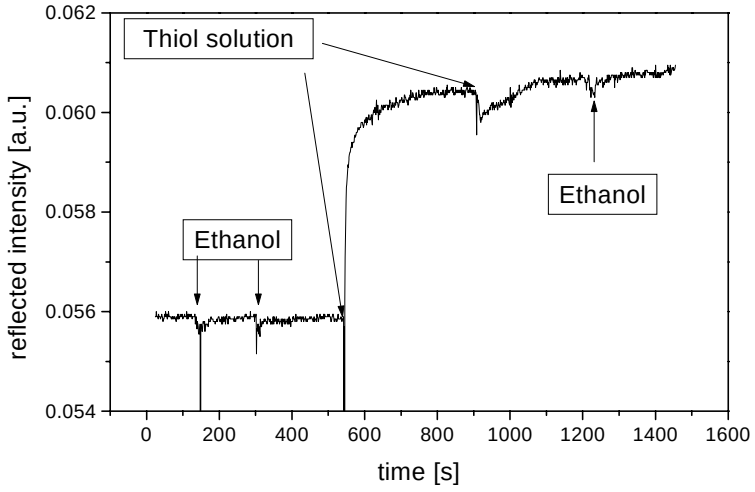

Fig. 8.3: Reflected intensity at θ = 7.5° during the formation of a monolayer of octadecanethiol.

After the intensity had reached a plateau indicating the end of the adsorption process, the sample was rinsed again, once with thiol solution and once with ethanol, before the second reflectivity scan as function of θ was recorded. In this second scan, as expected, a significant shift of the surface plasmon resonance to higher θ is observed (compare Fig. 8.2).

8.3 Evaluation procedures

In this subsection, two evaluation routines are presented that can be used to extract information about the adsorbed film from reflectivity measurements with the aid of the example that was introduced above. The optical model system that is used for the description of the measurement is drawn schematically in Fig. 8.4.

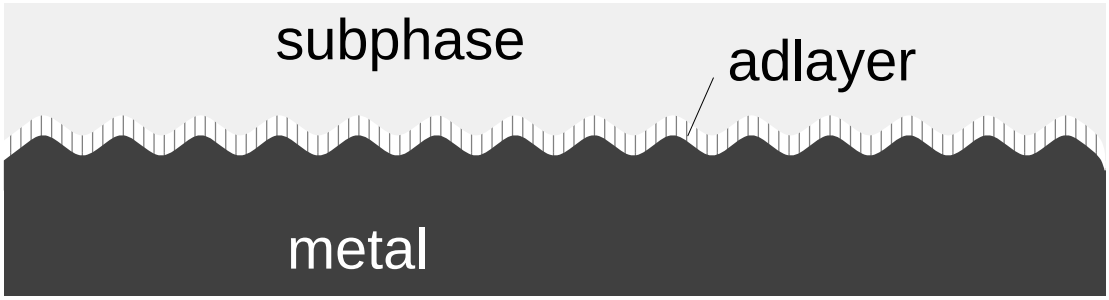

Fig. 8.4: The multilayer system under investigation.

On top of an infinitely thick corrugated metal surface, there is a thin and homogenous film, the adlayer, followed by another infinitely thick medium, the subphase. It is the aim of surface plasmon spectroscopy, to determine the thickness of the adlayer from the comparison between the reflectivity curves before and after the self assembly.

There is one major difficulty with the determination of the thickness of dielectric films with surface plasmon spectroscopy. Completely identical resonance curves may be obtained by a whole set of thickness' and refractive indices. A thin film with high refractive index cannot be distinguished from a thick film with low refractive index, therefore only one of these two parameters can be measured, the other one must be determined otherwise. Usually, the refractive index of the material under investigation is assumed as a constant. Its value may be derived from bulk measurements for materials where this is possible. In the case that is treated here, there is no bulk analogue to the thiol monolayer, therefore the same choice is made as in [Fla98], n = 1.5, in order to allow a comparison to the results that were obtained there. For the following, it must be kept in mind that the thickness that is derived from the measurements depends on the choice for the refractive index.

It should be noted further that the assumption of one homogenous layer which is characterised by one dielectric constant is not necessarily a good description of reality. For example dielectric films with holes which are smaller than the wavelength of light will mimic a homogenous dielectric film with a reduced thickness.

8.3.1 Rigorous modelling of the grating

The straightforward method to obtain the thickness of the adsorbed layer from an experiment like the one that was presented above consists in the determination of all parameters that describe the optical response of the bare grating. The refractive index of the subphase is easily determined from the position of the pseudocritical edge. With the routine that is described in chapter 3, the dielectric constant of the gold as well as the grating profile can be determined from a least squares fit. Fig. 8.5 shows the measured data and the fit. Some discrepancy is visible for very small θ which is due to light that is reflected from the cover glass and reaches the detector close to normal incidence only. In order to determine the thickness of the thiol layer, a second fit is performed to the reflectivity that was recorded after addition of the thiol where the only free parameter is the thickness of the thiol layer with an assumed refractive index of n = 1.5.

Changing this parameter shifts the minimum position of the modelled surface plasmon resonance. The changes in the form of the reflectivity curve as observed in Fig. 8.2 (mainly deepening and broadening of the resonance) cannot be explained with this model as it can be concluded from the difference between the data and the fit in Fig. 8.5 (b). This indicates that reality is different from the idealised picture (Fig. 8.4) which was the basis for this evaluation routine. Random roughness of the grating surface or inhomogenity of the adlayer may be responsible for this discrepancy.

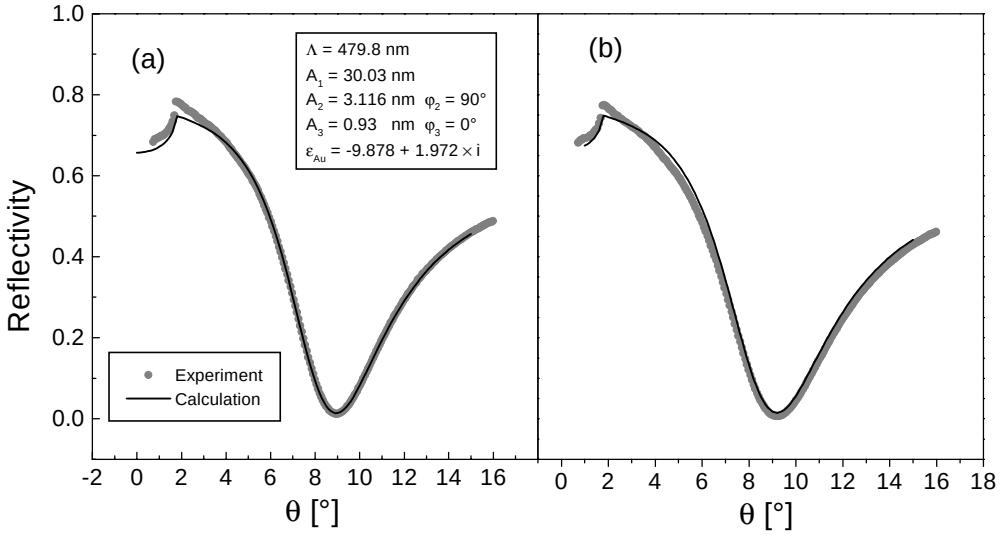

Fig. 8.5: (a) Measured reflectivity (circles) of the bare gold grating with a fit (straight line) based on the parameters that are shown in the inset.
(b) Measured reflectivity with an additional thiol monolayer (circles) with a model calculation including a dielectric adlayer with a thickness of 2.4 nm and a refractive index of n = 1.5. A better comparison of the two measured data sets is possible in Fig. 8.2

From this fit, the thickness of the dielectric layer was determined as 2.4 ± 0.1 nm, which is in agreement with literature. The apparent higher thickness of the layer that is reported by Ulman [Ulm91] is due to the lower refractive index (1.45 instead of 1.5) that is used there. When the same refractive index is used, consistent values are obtained [Fla98].

It can be concluded that although the changes in the form of the curve cannot be described by the addition of a single homogenous dielectric layer, the shift of the position of the surface plasmon minimum yields a film thickness that is consistent with other measurements. It is cumbersome to use this evaluation technique that is based on the complete characterisation of the grating. This procedure requires much time and computer power to perform the initial fit which, at the end, is not able to reproduce the measured reflectivity perfectly but is only used as a mean to determine the shift of a resonance curve. The following section introduces an easier routine to calculate the thickness of an adsorbed layer from the change of the minimum position.

8.3.2 Evaluation by transformation

In grating coupling experiments, the excitation of a surface plasmon resonance is accomplished by matching its momentum with a higher diffracted order of the incident light beam. In prism coupling, a plane light wave in a high index medium has the required momentum. These two alternatives are schematically depicted in Fig. 8.6.

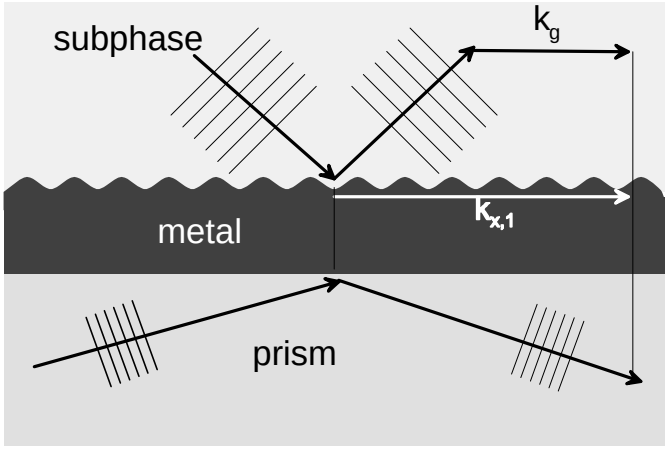

Fig. 8.6: Sketch of two processes to excite a surface plasmon on an subphase-metal interface: grating coupling and prism coupling.

While the determination of the thickness of a thin adlayer from a grating-coupling experiment is difficult, the evaluation of a prism-coupling experiment is easily done with the transfer matrix algorithm (compare chapter 2 or [Kar91]). If it can be assumed that the introduction of a coupling of the surface plasmon to light does not change its momentum, the momentum change due to a dielectric adlayer Δk will be the same for both experiments. This was assumed by Knoll et al. [Kno81] who evaluated data that were obtained by grating coupling calculating an equivalent prism coupling geometry.

In reality, the effect of the additional loss channels that are introduced by the finite thickness of the gold layer in prism coupling or by the grating topology in grating coupling are not negligible. It is the aim of this section to show that the evaluation of a grating coupling experiment as flat multilayer system yields the right thicknesses in spite of this fact.

As a first step, a transformation is made from the polar angle θ_{grat} of the grating coupling experiment to an angle θ_{pris} that would yield the same in-plane wavevector k_x in a prism coupling experiment as it is obtained in reality in the first diffracted order.

$$k_g + n_s \cdot k_0 \cdot \sin\left(\theta_{grat}\right) = k_x = n_p \cdot k_0 \cdot \sin\left(\theta_{pris}\right) \qquad (8.2)$$

Here k_g is the reciprocal grating vector, n_s and n_p the refractive index of the subphase and the prism, respectively, and k_0 the wavevector of the light in vacuo. In Fig. 8.7 the same data set as in Fig. 8.5 is shown where θ_{pris} is calculated for a hypothetical prism-coupling measurement. The model calculation of the bare gold grating is based on the model of a planar 3-layer system (prism/gold/subphase) with the parameters as shown in the graph.

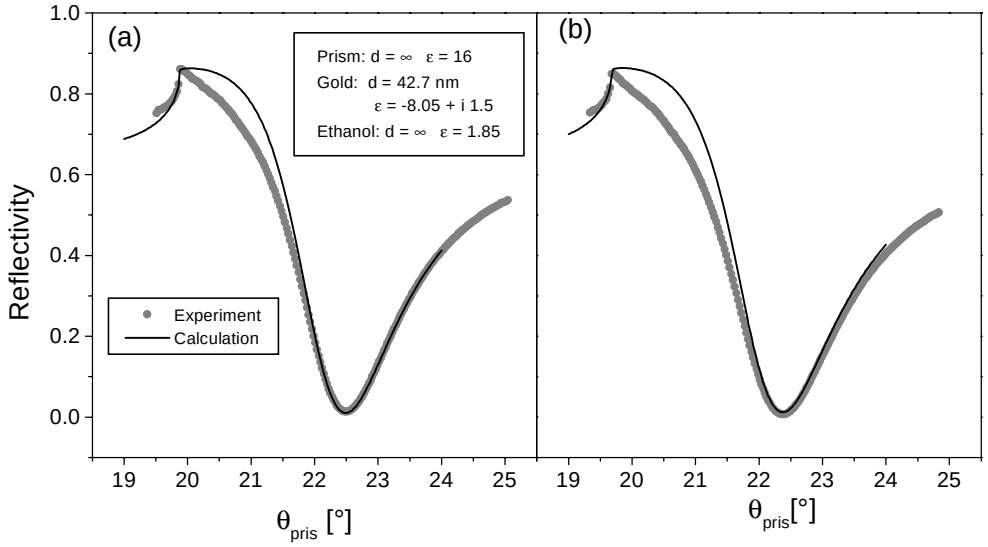

Fig. 8.7: The same set of data as in Fig. 8.5, transformed to a 'hypothetical prism scan' with a prism of refractive index $n_p = 4$.
(a) Experimental data from the pure gold surface. The straight line is a model calculation of a multilayer system as specified in the inset.
(b) Experimental data after the self-assembly. The modelling assumes an additional dielectric layer with a thickness of 2.3 nm and a refractive index of 1.5.

It is clear that the fit is pretty poor compared to the results that were obtained by rigorous modelling, especially close to the pseudocritical edge. Nevertheless, it is possible to reproduce the position and shape of the minimum rather well. In the model calculation on the right, the additional thiol layer was modelled with an assumed n = 1.5. The thickness was varied to give an optimum fit to the data. Within the error the same thickness is found with this technique as with the rigorous approach, d = 2.3 ± 0.1 nm.

It can be concluded that when the complex wavevector of the surface plasmon (position and halfwidth) is reproduced in the 'hypothetical prism' evaluation, the thickness of a thin dielectric film that is obtained with this technique is consistent with the result that was obtained by rigorous grating theory. It should be noted that the dielectric constant of the gold for this fit is ε = -8.05 + i 1.5 which is far from the value that is obtained in real prism-coupling experiments which is around ε = -12.5 + i 1.2. It seems that the influence of the corrugation on the surface plasmon can be described to some extent by introducing an unphysical dielectric constant.

It was checked if this evaluation can be generally applied by modelling the response of a grating coupler with and without an additional dielectric layer by rigorous grating theory and 'evaluating' the reflectivity with the 'evaluation by transformation technique' that has just been described. Thickness' below 100 nm were reproduced with an error of less than 1 % even when high amplitude gratings were modelled where the surface plasmon

resonance is strongly overcoupled. For thicker films, the quality of this evaluation method decreases.

Beyond a certain thickness, a dielectric film will support optical waveguide modes ([See e. g. [Kar91]). For a planar system, the wavevectors of these modes can be deduced from the transfer matrix formalism. It has been shown by comparing rigorous analysis of the electromagnetic response of the grating to planar multilayer calculations that there is only a negligible effect on the wavevector of these modes as long as the coupling grating does not significantly exceed the modulation depth as it is common for surface plasmon spectroscopy. As a consequence, for the determination of the optical constants of a given multilayer system with the aid of optical waveguide modes, the approximation as a plane multilayer system with an infinitely thick metal layer is justified.

8.4 Conclusion

It has been demonstrated that surface plasmon spectroscopy with an optical grating is well suited for the investigation of thin dielectric films. The simplified evaluation method, involving transformation to an equivalent prism-coupling experiment is applicable for thin dielectric films. For the analysis of the wavevector of optical waveguide modes in thick films, the corrugation can be neglected.

Summary

The influence of the surface plasmon resonance on the optics of surface relief gold gratings was investigated experimentally. The corresponding theoretical calculations were done with a numerical modelling routine.

In the thermally stimulated emission of light from a gold grating at 700°C, an enhanced emission was found under well-defined directions when a fixed wavelength was selected. The analysis of the emission direction and the polarisation led to the interpretation that an important channel for the conversion of thermal energy to light on a metallic grating involves the surface plasmon resonance as an intermediate step.

Model calculations of the reflectivity of deep metal gratings of different degrees of asymmetry allowed the investigation of higher order resonances that are attributed to self-coupled surface plasmons and may exist for depth-to-pitch ratios exceeding unity. It was shown that these resonances can be classified into two families that are characterised either by an even or an odd symmetry of the magnetic field. In this framework, effects that were found in model calculations for the first time in this work (coupling of coupled resonances) could be combined with effects known from literature to a consistent picture. A process for the fabrication of highly modulated gratings of different degrees of asymmetry was developed. Three coupled resonances could be observed experimentally on these gratings, and their dispersion and strength as a function of frequency and grating amplitude showed a reasonable agreement with model calculations. Some additional measurements were performed to highlight the particularities of the experimental geometry in the interaction of light with the coupled resonances. The very weak change in resonance wavelength for varying angle of incidence of such a resonance was shown. Further experiments stressed the importance of the symmetry of both the grating structure and the reflection geometry: On a grating with symmetric grating profile, coupling to a resonance with odd symmetry was not possible in a reflection geometry with even symmetry. When the symmetry of the reflection geometry was broken, or the symmetry of the incident magnetic field was changed from even to odd, coupling became possible. The observation of a kink in the wavelength-dependent reflectivity, which could not be reproduced in the model calculations, was assigned to scattering on imperfections of the grating into the additional decay channels offered by coupled surface resonances.

Coupled resonances and free surface plasmons play an important role as an intermediate step in the excitation and emission of fluorescent dyes. Fluorophores were used as a probe to map the localised optical near field of coupled surface resonances. It could be proved that according to the strong localisation of the electrical field, a site-dependent coupling strength to the coupled resonances was observed, whereas the coupling to free surface plasmons was not site-selective. A theoretical model was developed which was

capable of describing the experimental findings to some extent. In addition it was shown that the photobleaching in the field of coupled resonances is site-selective and can be tracked by an optical experiment. An application for the investigation of the diffusion in thin films on metal surfaces was proposed.

The polarisation dependence of the coupling of the incident light to the surface plasmon resonance was investigated in conical reflection geometry. A good agreement between measurement and modelling was found. In the limit of a perfectly conducting grating with vanishing amplitude, there is an analytical equation which describes the polarisation dependence of the depth of the plasmon-related minimum. No intuitive explanations for this behaviour could be found. Attempts to describe the polarisation dependence found in the literature turned out to disagree with the experimental data and the model calculations. An analysis of the polarisation of the reflected light showed that interaction with the surface plasmon may take place without being detected in the total reflected intensity. This finding may be helpful for a better understanding of these effects that will hopefully be developed in the future.

The applicability of diffraction gratings for the investigation of ultra-thin dielectric films on metal surfaces (surface plasmon spectroscopy) was demonstrated experimentally. A simple evaluation routine was developed, which avoids the complicated mathematical treatment of a grating by transformation of the problem to an almost equivalent planar multilayer system.

As a final remark, it can be stated that the strong impact of the geometry of the metal-dielectric interface on the surface plasmon resonance leads to many interesting effects in the optics of metal gratings. In this work, a better understanding of some of these effects has been obtained by using a modern modelling algorithm for the interpretation of experimental results. Nevertheless, more research is needed to answer some questions that were raised here, and there is no doubt that many puzzling phenomena in the optics of metal gratings are to be discovered in the future.

Literature

[And97] Andrew, P., S. C. Kitson and W. L. Barnes (1997). "Surface-plasmon energy gaps and photoabsorption." Journal of Modern Optics **44**(2): 395-406.

[Ash76] Ashcroft, N. W. and N. D. Mermin. **Solid state physics**, Saunders College (1976).

[Ast00] Astilean, S., P. Lalanne and M. Palmaru (2000). "Light transmission through metallic channels much smaller than the wavelength." to appear in Optics Communications

[Aus94] Aust, E. F., S. Ito, M. Sawodny and W. Knoll (1994). "Investigation of polymer thin films using surface plasmon modes and optical waveguide modes." Trends in polymer science **2**(9): 313-323.

[Axe76] Axelrod, D., D. E. Koppel, J. Schlessinger, E. Elson and W. Webb (1976). "Mobility measurements by analysis of fluorescence photobleaching recovery kinetics." Biophysics Journal **16**: 1055-1069.

[Bar98] Barnes, W. L. (1998). "Fluorescence near interfaces: the role of photonic mode density." Journal of Modern Optics **45**(4): 661-99.

[Bar00] Barnes, W. L. (2000) Personal communication

[Bar97b] Barnes, W. L., S. C. Kitson, T. W. Preist and J. R. Sambles (1997). "Photonic surfaces for surface-plasmon polaritons." Journal of the Optical Society of America A **14**(7): 1654-61.

[Bar96] Barnes, W. L., T. W. Preist, S. C. Kitson and J. R. Sambles (1996). "Physical origin of photonic energy gaps in the propagation of surface plasmons on gratings." Physical Review B **54**(9): 6227-6244.

[Bar95] Barnes, W. L., T. W. Preist, S. C. Kitson, J. R. Sambles, N. P. K. Cotter and D. J. Nash (1995). "Photonic gaps in the dispersion of surface plasmons on gratings." Physical Review B **51**(6): 11164-11167.

[Bar85] Barnes, W. L. and J. R. Sambles (1985). "Re-radiation of surface -plasmon - polaritons by surface roughness." Solid State Communications **55**(11): 921-923.

[Boe99] Boerner, V., A. Gombert, A. Heinzel and M. Ternant (1999). "Spectrally selective microstructured metal surfaces." Proceedings of the EOS Topical meeting on diffractive optics: 290.

[Bry91] Bryan-Brown, G. P., S. J. Elston and J. R. Sambles (1991). “Comparison of metal parameters obtained from prism and grating coupling to surface plasmon polaritons.” Journal of Modern Optics **38**(6): 1181-1187.

[Bur74] Burstein, E., W. P. Chen, Y. J. Chen and A. Hartstein (1974). “Surface polaritons - propagating electromagnetic modes at interfaces.” Journal of Vacuum Science and Technology **11**(6): 1004-1019.

[Bus00] Busse, S., Thesis: "Untersuchung molekularer Erkennungsreaktionen mit einem integriert-optischen Mach-Zehnder Interferometer", Johannes Gutenberg-Universität, Mainz (2000)

[Cha82] Chandezon, J., M. T. Dupuis, G. Cornet and D. Maystre (1982). “Multicoated gratings: A differential formalism applicable in the entire optical region.” Journal of the Optical Society of America **72**(7): 839-846.

[Col93] Collett, E. **Polarized light**, Marcel Dekker(1993).

[Cot95] Cotter, N. P. K., T. W. Preist and J. R. Sambles (1995). “Scattering-matrix approach to multilayer diffraction.” Journal of the Optical Society of America A **12**(5): 1097-1103.

[Dre70] Drexhage, K. H. (1970). “Monomolecular layers and light.” Scientific American **222**(3): 108-119.

[Ebb98] Ebbesen, T. W., H. J. Lezec, H. F. Ghaemi, T. Thio and W. P. A. (1998). “Extraordinary transmission through sub-wavelength hole arrays.” Nature **391**(12): 667-669.

[Els91] Elston, S. J., G. P. Bryan-Brown and J. R. Sambles (1991). “Polarisation conversion from diffraction gratings.” Journal of the Optical Society of America A **13**(4): 803-810.

[Fan41] Fano, U. (1941). “The theory of anomalous diffraction gratings and of quasi-stationary waves on metallic surfaces (Sommerfeld’s waves)” Journal of the Optical Society of America **31**: 213.

[Fer93] Fernandez, U., T. Fischer and W. Knoll (1993). “Surface-plasmon microscopy with grating couplers.” Optics Communications **102**: 49-52.

[Fis95] Fischer, B., T. M. Fischer and W. Knoll (1995). “Unusual splitting behaviour of the dispersion of surface polaritons in gratings of different symmetry, amplitude and profile.” Applied Optics **34**(25): 5773-5779.

[Fla98] Flath, J., Thesis: "Metall-Sulfide an funktionalisierten Grenzflächen: Nukleation, Wachstum und Charakterisierung", Johannes Gutenberg-Universität, Mainz (1998)

[Gar97] Garcia-Vidal, F. J. and J. B. Pendry (1997). “Collective theory for surface enhanced Raman scattering.” Physical Review Letters **77**(6): 1163-1166.

[Ger82] Gerthsen, K., H. O. Kneser, H. Vogel. **Physik**, Springer Verlag, (1982).

[Gor77] Gordon, J. G. and J. D. Swalen (1977). “The effect of thin organic films on the surface plasma resonance on gold.” Optics Communications **22**(3): 374-376.

[Gyö99] Györvary, E., B. Wetzer, U. B. Sleytr, A. Sinner, A. Offenhäusser and W. Knoll (1999). “Lateral Diffusion of Lipids in Silane-, Dextran-, and S-Layer-Supported Mono- and Bilayers.” Langmuir **15**: 1337-1347.

[Har96b] Harris, J. B., T. W. Preist, J. R. Sambles, R. N. Thorpe and R. A. Watts (1996). “Optical response of bigratings.” Journal of the Optical Society of America A **13**(10): 2041-2049.

[Har96] Harris, J. B., T. W. Preist, E. L. Wood and J. R. Sambles (1996). “Conical diffraction gratings containing uniaxial materials.” Journal of the Optical Society of America A **13**(4): 803-810.

[Hen89] Hendrickson, W. A., A. Pähler, J. L. Smith, Y. Satow and E. A. Merritt (1989). “Crystal structure of core strepavidin determined from multiwavelength anomalous diffraction of synchrotron radiation.” Proceedings of the National Academy of Sciences in the USA, **86**: 2190.

[Her94] Herminghaus, S., M. Klopfleisch and H. J. Schmidt (1994). “Attenuated total reflectance as a quantum interference phenomenon.” Optics Letters **19**(4): 293-295.

[Hin94] Hinchcliffe, A., Munn, R. W. (1985), **Molecular electromagnetism,** John Wiley & Sons, New York

[Jac83] Jackson, J. D. **Klassische Elektrodynamik**, Walter de Gruyter (1983).

[Kar91] Karthe, W. and R. Müller. **Integrierte Optik**, Akademische Verlagsgesellschaft Geest & Portig, (1991).

[Kan96] Kazandjian, L. (1996). “Rayleigh methods applied to electromagnetic scattering from gratings in general homogenous media“ Physical Review E **54**(6): 6902-6815.

[Kit95b] Kitson, S. C., W. L. Barnes, G. W. Bradberry and J. R. Sambles (1995). “Surface profile dependence of surface plasmon band gaps on metallic gratings.” Journal of Applied Physics **79**(9): 7383-7385.

[Kit96c] Kitson, S. C., W. L. Barnes and J. R. Sambles (1996). “Full photonic band gap for surface modes in the visible.” Physical Review Letters **77**(13): 2670-3.

[Kit96b] Kitson, S. C., W. L. Barnes and J. R. Sambles (1996). “Photoluminescence from dye molecules on silver gratings.” Optics Communications **122**: 4-6.

[Kit95] Kitson, S. C., W. L. Barnes and J. R. Sambles (1995). “Surface-plasmon energy gaps and photoluminescence.” Physical Review B **52**(15): 11441-5.

[Kit96] Kitson, S. C., W. L. Barnes, J. R. Sambles and N. P. K. Cotter (1996). “Excitation of molecular fluorescence via surface plasmon polaritons.” Journal of Modern Optics **43**(3): 573-82.

[Kle99] Kleideiter, G., Z. Sekkat, M. Kreiter, M. D. Lechner, W. Knoll (2000) „Photoisomerization of disperse red one in films of poly(methyl-methacrylate) at high pressure“ Journal of Molecular Structure **521**: 167-178

[Kle00] Kleideiter, G., Thesis: "Oberflächenplasmonen- und Wellenleitermoden-Spektroskopie unter hohen hydrostatischen Drücken", Universität Osnabrück (1999)

[Kno91] Knoll, W. (1991). “Polymer thin films and interfaces characterized with evanescent light.” Makromolecular Chemistry **192**(12): 2827-2856.

[Kno97] Knoll, W. (1997). Guided wave optics for the characterisation of polymeric thin films and interfaces. **Handbook of optical properties 2.** R. E. Hummel and P. Wießmann. Boca Raton, CRC Press**:** 373-400.

[Kno98] Knoll, W. (1998). “interfaces and thin films as seen by bound electromagnetic waves.” Annual Review on Physical Chemistry **49**: 569-638.

[Kno81] Knoll, W., M. R. Philpott, J. D. Swalen and A. Girlando (1981). “Emission of light from Ag metal gratings coated with dye monolayer assemblies.” Journal of Chemical Physics **75**(10): 4795-4799.

[Kol82] Kolb, D. M. (1982). The study of solid-liquid interfaces by surface plasmon polariton excitation, **Surface Polaritons**, V. M. Agranovich and D. L. Mills. (ed.) Amsterdam, Paris, Oxford, North Holland publishing company**:** 299-329.

[Kre71] Kretschmann, E. (1971). “Die Bestimmung optischer Konstanten von Metallen durch Anregung von Oberflächenplasmaschwingungen.” Zeitschrift für Physik **241**: 313-324.

[Lak81] Laks, B., D. L. Mills and A. A. Maradudin (1981). “Surface polaritons on large-amplitude gratings.” Physical Review B **23**(10): 4965-4976.

[Li94b] Li, L. (1994). “Bremmer series, R-Matrix propagation algorithm and numerical modelling of diffraction gratings.” Journal of the Optical Society of America A **11**(11): 2829-2836.

[Li94] Li, L. (1994). “Multilayer-coated diffraction gratings: differential method of Chandezon et al. revisited.” Journal of the Optical Society of America A **11**(11): 2816-2828.

[Lieb99] Liebermann, T., Thesis: "Oberflächenplasmonen Fluoreszenz-spektroskopie zur Detektion molekularer Erkennungsreaktionen", Johannes Gutenberg-Universität, Mainz (1999)

[Lop98] Lopez- Rios, T., D. Mendoza, F. J. Garcia-Vidal, J. Sanchez-Dehesa and B. Pannetier (1998). “Surface shape resonances in lamellar metallic gratings.” Physical Review Letters **81**(3): 665-668.

[Lyn85] Lynch, D. W. and W. R. Hunter. **Comments on the optical constants of metals and an introduction to the data for several materials**, Academic Press Boston (1985).

[Mai85] Mai, X., R. Moshrefzadeh, U. J. Gibson, G. I. Stegeman and C. T. Seaton (1985). “Simple versatile method for fabricating guided-wave gratings.” Applied Optics **24**(19): 3155-3161.

[Mar97] Maradudin, A. A., A. V. Shchegrov and T. A. Leskova (1997). “Resonant scattering of electromagnetic waves from a rectangular groove on perfectly conducting surface.” Optics Communications **135**: 352-360.

[May82] Maystre, D. (1982). General study of grating anomalies from electromagnetic surface modes, **Electromagnetic surface modes**. A. D. Boardman (ed.), John Wiley & Sons**,** 661-724.

[Ott68] Otto, A. (1968). “Excitation of nonradiative surface plasma waves in silver by the method of frustrated total reflection.” Zeitschrift für Physik **216**: 398-410.

[Pet80] Petit, R. **Electromagnetic theory of gratings**, Springer Verlag (1980).

[Pla99] Plamenevskii, B. A., V. E. Grikurov, P. Neittaanmäki and M. A. Lyalinov (1990). “On surface waves in diffraction gratings.” Reports on the department of mathematical information technology series b scientific computing (Preprint) **13**: 1-20.

[Plo96] Plowman, T. E., W. M. Reichert , C. R. Peters, H. K. Wang, D. A. Christensen and J. N. Herron (1996). “Femtomolar sensitivity using a channel-etched thin film waveguide fluoroimmunosensor.” Biosensors and Bioelectronics **11**(1): 149-160.

[Poc78] Pockrand, I. (1978). “surface plasma oscillations at silver surfaces with thin transparent and absorbing coatings.” Surface Science **72**: 577-588.

[Por99] Porto, J. A., F. J. Garcia-Vidal and J. B. Pendry (1999). “Transmission resonances on metallic gratings with very narrow slits.” Physical Review Letters **83**(14): 2845-2848.

[Pre95] Preist, T. W., N. P. K. Cotter and J. R. Sambles (1995). “Periodic multilayer gratings of arbitrary shape.” Journal of the Optical Society of America A **12**(8): 1740-1748.

[Pre97] Preist, T. W., J. B. Harris, N. P. Wanstall and J. R. Sambles (1997). “Optical response of blazed and overhanging gratings using oblique Chandezon transformations.” Journal of Modern Optics **44**(6): 1073-1080.

[Rae88] Raether, H. **Surface plasmons**, Springer Verlag (1988).

[Kri90] S. Krishnan , G. P. H., R.H. Hauge and J.L. Margrave (1990). “Spectral emissivities and optical properties of electromagnetically levitated liquid metals as functions of temperature and wavelength.” High Temperature Science **29**: 17-52.

[Sam91] Sambles, J. R., G. W. Bradberry and F. Yang (1991). “Optical excitation of surface plasmons: an introduction.” Contemporary physics **32**(3): 173-183.

[Sar81] Sarid, D. (1981). “Long range surface plasma waves on very thin metal films.” Physical Review Letters **47**: 1927-1930.

[Sch98] Schmidt, E. K., T. Liebermann, M. Kreiter, A. Jonczyk, R. Naumann, A. Offenhäusser, E. Neumann, et al. (1998). “Incorporation of the acetylcholine receptor dimer from torpedo californica in a peptide supported lipid membrane investigated by surface plasmon and flourescence spetroscopy.” Biosensors & Bioelectronics **13**: 585-591.

[Sch99] Schröter, U. and D. Heitmann (1999). “Grating couplers for surface plasmons excited in thin metal films in the Kreschmann-Raether configuration.” Physical Review B **60**(7): 4992-4999.

[Sob98] Sobnack, M. B., W. C. Tan, N. P. Wanstall, T. W. Preist and J. R. Sambles (1998). “Stationary Surface Plasmons on a Zero-Order Metal Grating.” Physical Review Letters **80**(25): 5667-5670.

[Tam77] Tamir, T. and S. T. Peng (1977). “Analysis and design of grating couplers.” Applied Physics **14**: 235-254.

[Tan98] Tan, W. C., T. W. Preist, J. R. Sambles, M. B. Sobnack and N. P. Wanstall (1998). “Calculation of photonic band structures of periodic multilayer grating systems by use of a curvilinear coordinate transformation.” Journal of the Optical Society of America A **15**(9): 2365-2372.

[Ulm91] Ulman, A. An introduction to ultrathin organic films: From Langmiur Blodgett to Self-Assembly, Academic press Boston (1991).

[Vei95] Veith, M., Thesis: "Wechselwirkung von Oberflächepolaritonen mit periodisch modulierten Grenzflächen", Johannes Gutenberg-Universität Mainz (1995)

[Wan99] Wanstall, N. P., Thesis: "Modelling the electromagnetic response of deep, blazed and overhanging gratings", University of Exeter (1999)

[Wan98] Wanstall, N. P., T. W. Preist, W. C. Tan, M. B. Sobnack and J. R. Sambles (1998). “Standing-wave surface-plasmon resonances with overhanging zero-order metal gratings.” Journal of the Optical Society of America A **15**(11): 2869-2876.

[Wat97b] Watts, R. A. (1997). “Polarisation conversion from blazed diffraction gratings.” Journal of Modern Optics **44**(6): 1231-1241.

[Wat97a] Watts, R. A., T. W. Preist and J. R. Sambles (1997). “Sharp surface plasmon resonances on deep diffraction gratings.” Physical Review Letters **79**(20): 3978-3981.

[Wat97c] Watts, R. A., J. R. Sambles and J. B. Harris (1997). “An experimental test of conical diffraction theory.” Optics Communications **135**: 189 -192.

[Wat97] Watts, R. A., J. R. Sambles, M. C. Hutley, T. W. Preist and C. R. Lawrence (1997). “A new optical technique for characterizing reference artefacts for surface profilometry.” Nanotechnology **8**: 35-39.

[Win76] Winsemius, P., v. K. F. F., L. H. P. and v. W. C. G. (1976). “Temperature dependence of the optical properties of Au, Ag and Cu.” Journal of Physics F **6**(8): 1583-1606.

[Woh99] Wohlfart, P., J. Weiß, J. Käshammer, M. Kreiter, C. Winter, R. Fischer and S. Mittler-Neher (1999). “MOCVD of aluminum oxide/hydroxide onto organic self-assembled monolayers.” Advanced Materials **5**(4): 165-170.

[Woo95] Wood, E. L., J. R. Sambles, N. P. Cotter and S. C. Kitson (1995). “Diffraction grating characterisation using multiple-wavelength excitation of surface plasmon polaritons.” Journal of modern Optics **42**(6): 1343-1349.

[Woo02] Wood, R. W. (1902). “On a remarkable case of uneven distribution of light in a diffraction grating spectrum.” Philosophical Magazine **4**: 396-402.

[Yea96] Yeatman, E. M. (1996). “Resolution and sensitivity in surface plasmon microscopy and sensing.” Biosensors & Bioelectronics **11**(6/7): 635-649.

[Yeh98] Yeh, P. **Optical waves in layered media,** John Wiley and Sons (1998).

Abbreviations

A_i	amplitude in the Fourier representation of the grating profile
D	dielectric displacement
D	diffusion constant
e	charge of an electron
E	electrical field strength
FRAP	fluorescence recovery after photobleaching
H	magnetic field
h	Planck's constant
I	intensity
k	wavevector
LRSP	long range surface plasmon
m	diffracted order
m_e	mass of an electron
ME_i	resonance with a magnetic field with even symmetry
MO_i	resonance with a magnetic field with odd symmetry
n	normal vector
n	refractive index
n_e	electron density
P	probability
$\mathbf{p_{TE}}$	unit vector for TE polarisation
$\mathbf{p_{TM}}$	unit vector for TM polarisation
r	transition dipole moment
sc	scaling factor
SEM	scanning electron microscope
SRSP	short range surface plasmon
t	time
TE	transverse electric polarisation
TM	transverse magnetic polarisation
V	transition matrix element
x	Cartesian co-ordinate
x	vector in space
y	Cartesian co-ordinate
z	Cartesian co-ordinate
ε	dielectric constant
ε_0	permettivity of vacuum
φ	polarisation angle
φ_i	phase in the Fourier representation of the grating profile
Λ	grating period
λ	wavelength of light
μ	magnetic permeability
μ_0	permeability of free space
θ	polar angle
θ_{etch}	etching angle
θ_{ob}	obliquity angle
θ_{rel}	relative polar angle
θ_{lit}	polar angle in the Littrow mount
ρ	charge density
σ	density of states
τ	collision time
ω	angular frequency
Ω	solid angle
ω_p	plasma frequency
Ψ	azimuthal angle
Ψ_{tilt}	tilt angle